

**DEVELOPING A SYNERGY BETWEEN SPACE-BASED INFRARED SOUNDERS AND
THE GROUND-BASED ATMOSPHERIC EMITTED RADIANCE INTERFEROMETER
(AERI) TO IMPROVE THERMODYNAMIC PROFILING OF THE PLANETARY
BOUNDARY LAYER**

by

David M. Loveless

A dissertation submitted in partial fulfillment of

the requirements for the degree of

Doctor of Philosophy

(Atmospheric & Oceanic Sciences)

at the

UNIVERSITY OF WISCONSIN-MADISON

2021

Date of final oral examination: Wednesday 11 August 2021

The dissertation is approved by the following members of the Final Oral Committee:

Steven A. Ackerman, Professor, Atmospheric and Oceanic Sciences, UW-Madison

Timothy J. Wagner, Scientist, Space Science and Engineering Center, UW-Madison

Ankur Desai, Professor, Atmospheric and Oceanic Sciences, UW-Madison

Michael C. Morgan, Professor, Atmospheric and Oceanic Sciences, UW-Madison

Tristan S. L'Ecuyer, Professor, Atmospheric and Oceanic Sciences, UW-Madison

© Copyright by David M. Loveless 2021
All Rights Reserved

Acknowledgements

I have been blessed to have met some amazing people since coming to Madison in the fall of 2014. First, to Alex Goldstein, Kate Sauter, Keiko Yamamoto, Kai-Wei Chang, and Luke Gloege, thank you so much for your friendship. Our collaborative homework and study sessions through the first year of classes made that first year so much more enjoyable than it otherwise would have been. My participation on the Plains Elevated Convection At Night (PECAN) field campaign during the summer of 2015 is an experience that will stay with me forever. Beyond the joys of being on a field campaign designed to make observations in environments supportive of nocturnal convection, I particularly enjoyed spending time with Coda Phillips, Skylar Williams, and Andrew Wagner. To Coda, Skylar, Keiko, and Charles White you guys were amazing officemates and made coming to work every day so much fun. Coda, I am so thankful for all of your coding support as well, I am going to be seeking you out next time I get a new computer and all of my code breaks because of the computer transfer. Outside of the department, I am particularly thankful for the friendship of Daniel Fung and Zach Williams. Thank you for being people I can lean on in difficult times. To Curtis Walker, thank you for being a great friend from Oneonta and through our continually evolving career positions. To Leslie Harten, thank you for being a friend and a mentor from a far, even though we only see each other once a year (and that was before COVID). I cherish your friendship and mentorship.

I have to thank my undergraduate advisor at SUNY Oneonta, Todd Ellis, for cultivating my interest in thermodynamics and remote sensing and for being a continually encouraging voice. I am especially thankful to both Steve Ackerman and Wayne Feltz for taking a chance on me in the first place in offering me a research assistantship position and for ensuring that I always had

funding to continue on this journey. To my committee members: Ankur Desai, Michael Morgan, and Tristan L'Ecuyer, thank you for your guidance and mentorship.

I would not have made it this far without my advisor Tim Wagner. Thank you for your patience, encouragement, and advice every week (sometimes more than that). Thank you for providing comments on far too many paper drafts, conference abstracts, poster presentations, power point slides, everything. Thank you for advocating for me to continue my career at SSEC and looking forward to our new projects together. I am also grateful for the mentorship provided to me by Bob Knuteson at SSEC and Dave Turner at NOAA. Thank you for teaching me so much and asking difficult questions while remaining encouraging as well.

To my family, thank you so much for being encouraging and supportive as my interest in weather has turned into far more years of schooling than I think any of us could have imagined. I am thankful that you have allowed me to pursue this dream of getting a PhD, despite having no idea what graduate school really entailed at the start of this whole thing.

Lastly, to my wife Michelle. We became friends, got married, and now have had kids in these last several years and I am so glad that we get to do life together. I am certain that having a spouse finishing a PhD would be stressful in its own right, let alone doing it while recovering from pregnancy and having two newborns at home, all in the middle of a pandemic that restricted how much we could see family and support people. This is as much your accomplishment as it is mine.

This project is possible due to the support from NASA prime award number NNX15AQ03A “Educational Opportunities in NASA STEM (EONS)”.

Abstract

Profiles, or soundings, of atmospheric temperature and water vapor from remotely sensed platforms provide critical observations within the temporal and spatial gaps of the radiosonde network. The 2017 National Academies of Science Decadal Survey highlighted that observations of the planetary boundary layer (PBL) from the current space-based observing system are not of the necessary accuracy or resolution for monitoring and predicting high impact weather phenomena. The National Research Council (NRC, 2009) suggested the development of a network of ground-based profilers to supplement the existing space-based observing system in order to improve observations of the PBL. One instrument that fits the requirements outlined by the NRC (2009) for the ground-based network for profilers is the Atmospheric Emitted Radiance Interferometer (AERI).

This dissertation advances the understanding of the benefits of a synergy between the ground-based AERI and space-based hyperspectral infrared (IR) sounders as a method for improving thermodynamic sounding using three studies: 1) A synthetic information content analysis in clear sky conditions to quantify improvements offered by the synergy of profilers in terms of degrees of freedom, vertical resolution, and uncertainties. 2) A synthetic information content study in three cloudy sky scenes to assess the potential of the ground-based and space-based synergy as a possible solution to IR sounding in cloudy environments. 3) Develop an optimal estimation retrieval that combines AERI with the space-based Cross-track Infrared Sounder (CrIS) on S-NPP and NOAA-20 to assess the performance of the synergy in practice, outside of synthetic studies.

The clear sky information content study shows that a combination of AERI with any of the three polar-orbiting IR sounders: The Atmospheric Infrared Sounder (AIRS), the Cross-track

Infrared Sounder (CrIS), or the Infrared Atmospheric Sounding Interferometer (IASI), results in a 30-40% increase in degrees of freedom (DOF) in the surface to 700 hPa layer compared to the space-based instrument alone. Introducing AERI measurements to the observing system also results in significant improvements to vertical resolution and uncertainties in the bottom 1000 m of the atmosphere compared to CrIS measurements alone.

The cloudy sky information content analysis show that the synergy of CrIS+AERI has greater temperature information in cloudy sky conditions than in clear sky because the cloud provides an opaque layer that sharpens the Jacobians enabling a temperature retrieval at that layer. AERI and CrIS both lose water vapor information as the cloud becomes optically thick, though a synergy of CrIS+AERI would minimize those losses. In partly cloudy scenes, the information content of the synergy is most sensitive to cloud cover at greater than 50% aerial cloud fraction.

The combined CrIS+AERI retrieval is assessed for a single case study. CrIS+AERI did not produce the best comparison to the radiosonde profile when compared to the individual instrument retrievals and was found to have greater uncertainty as well. It is shown that this is likely due to the small uncertainties used for each instrument. The synergy of CrIS+AERI was found to replicate the improvements in vertical resolution identified in the information content analysis. The vertical resolution of the combined retrieval in this case study is found to exceed the 1 km resolution goal stated by the 2017 Decadal Survey.

Table of Contents

ACKNOWLEDGEMENTS	I
ABSTRACT.....	III
TABLE OF CONTENTS	V
LIST OF FIGURES	VII
LIST OF TABLES	X
CHAPTER 1: INTRODUCTION.....	1
1.1 HISTORY OF INFRARED SOUNDING.....	2
1.2 MOTIVATION.....	6
1.3 BACKGROUND ON INSTRUMENT SYNERGY STUDIES.....	9
CHAPTER 2: RETRIEVING THERMODYNAMIC INFORMATION FROM RADIANCE MEASUREMENTS.....	13
2.1 GAUSS-NEWTON ESTIMATION	14
2.2 INFORMATION CONTENT	20
CHAPTER 3: INSTRUMENTATION	23
CHAPTER 4: RADIOSONDE DATA	27
CHAPTER 5: CLEAR SKY INFORMATION CONTENT ANALYSIS.....	30
5.1 INTRODUCTION.....	30
5.2 RADIATIVE TRANSFER MODELLING	31
5.3 CONSTRUCTING THE A PRIORI COVARIANCE MATRIX:	33
5.4 RESULTS	34
5.4.1 Degrees of Freedom.....	34
5.4.2 Variations in Information with Precipitable Water Vapor.....	38
5.4.3 Vertical Resolution	47
5.4.4 Uncertainties	52
5.5 SUMMARY AND CONCLUSIONS.....	57
CHAPTER 6: CLOUDY SKY INFORMATION CONTENT ANALYSIS	60
6.1 INTRODUCTION.....	60
6.2 EXPERIMENTAL DESIGN	61
6.2.1 Constructing the A Priori Covariance Matrix	62
6.2.2 Radiative Transfer Modelling	63
6.2.3 Computing Jacobians in Partly Cloudy Scenes	64
6.3 RESULTS	69
6.3.1 Information Content with Varying Cloud Optical Depth	69
6.3.2 A Comment on Unexpected Results	82
6.3.3 Information Content with Varying Cloud Fraction	83
6.5 SUMMARY AND CONCLUSIONS.....	87

CHAPTER 7: DEVELOPING A SYNERGISTIC RETRIEVAL.....	90
7.1 INTRODUCTION.....	90
7.2 ALGORITHM DETAILS.....	91
7.3 RESULTS	93
7.4 SUMMARY AND FUTURE WORK	99
CHAPTER 8: CONCLUSIONS AND FUTURE WORK	102
8.1 SUMMARY OF RESULTS	102
8.2 BROADER IMPACTS	104
8.2.1 Sounding from Geostationary Orbit.....	104
8.2.2 Applications to System Process Studies	106
8.3 FUTURE WORK.....	107
REFERENCES.....	111

List of Figures

Figure 1.1: Comparison of AERIOe (AERI-derived, red), NUCAPS (CrIS-derived, blue), and radiosonde (black) profiles of temperature (left) and water vapor mixing ratio (right) on 20 June 2015.

Figure 2.1: Radiances for the upward looking AERI (red) and downward looking CrIS (blue).

Figure 2.2: Temperature Jacobians for AERI (a) and CrIS (b).

Figure 5.1: A priori covariance matrix used in this analysis. Bottom-left is temperature covaried against itself. Top-right is water vapor varied against itself. Top-left and bottom-right are temperature and water vapor covaried against each other.

Figure 5.2: DOF for temperature (a-c) and water vapor (d-f) for the full troposphere (surface to 200 hPa). DOF for the individual sensors is displayed in black. DOF for the synergy of the AERI with each respective space-based sensor is displayed in red.

Figure 5.3: Same as in Figure 5.2 but for the surface to 700 hPa layer.

Figure 5.4: AERI DOF for temperature (a) and water vapor (c) binned for every 1 cm of PWV. Number of profiles in each PWV bin is displayed as the gray bars, DOF for the full troposphere (surface to 200 hPa) is displayed in black, and the DOF for the surface to 700 hPa is displayed in red. The diagonal of high (4+ cm, green), medium (2-3 cm, orange), and low (less than 1 cm, purple) PWV composite mean averaging kernels for AERI for temperature and water vapor are shown in b and d respectively.

Figure 5.5: Composite temperature (a – c) and water vapor (d – f) Jacobians for AERI in the high (4+ cm, a and d), medium (2 – 3 cm, b and e), and low (less than 1 cm, c and f) PWV composites.

Figure 5.6: Same as in Figure 5.4 but for CrIS.

Figure 5.7: Same as in Figure 5.5 but for CrIS.

Figure 5.8: Same as in Figure 5.4 but for CrIS+AERI.

Figure 5.9: Vertical resolution for AERI (red), CrIS (blue), and the synergy of CrIS+AERI (gray) for temperature (a) and water vapor (b). Shading is between the 25th and 75th percentiles for all 4,720 profiles in the analysis.

Figure 5.10: Vertical resolution for temperature (a-c) and water vapor (d-f) for AERI (a and d), CrIS (b and e), and CrIS+AERI (c and f) in high (4+ cm, green), medium (2-3 cm, orange), and low (less than 1 cm, purple) PWV composites.

Figure 5.11: 1σ uncertainties for AERI (red), CrIS (blue), and CrIS+AERI (gray) for temperature (a), water vapor mixing ratio (b), and relative humidity (c). Shading is between the 25th and 75th percentiles for all 4,720 profiles in the analysis. For reference, the 1σ uncertainties of the a priori are about 14 K and 4 g kg⁻¹ at the surface.

Figure 5.12: Posterior correlation matrix for temperature (a-c) and water vapor (d-f) for AERI (a and d), CrIS (b and e), and the synergy of CrIS+AERI (c and f).

Figure 5.13: 1σ uncertainties for temperature (a-c) and water vapor (d-f) for AERI (a and d), CrIS (b and e), and CrIS+AERI (c and f) in high (4+ cm, green), medium (2-3 cm, orange), and low (less than 1 cm, purple) PWV composites.

Figure 6.1: Temperature (red) and dew point temperature (blue) profiles used for each cloudy sky case, interpolated to the 500 m grid used for radiative transfer calculations. The black lines indicate the location of the cloud layer in the simulations.

Figure 6.2: A priori covariance matrix used in this analysis. Bottom-left is temperature covaried against itself. Top-right is water vapor varied against itself. Top-left and bottom-right are temperature and water vapor covaried against each other.

Figure 6.3: Approximate sensitivity of the CrIS FOV. Dots represent the 375 m grid of the resolution of the Visible Infrared Imaging Radiometer Suite (VIIRS).

Figure 6.4: a-c display the histograms of the fraction of the total CrIS FOV sensitivity that is cloudy, given random placements of the clear and cloudy pixels, for 25% (a), 50% (b), and 75% (c) areal cloud fraction. d-f display the pattern of clear and cloudy pixels when simulating a cloud mass approaching from the south with 25% (d), 50% (e), and 75% (f) areal cloud fractions.

Figure 6.5: DOF for AERI (purple), CrIS (orange), and CrIS+AERI (green) for the full troposphere (a and d), above-cloud (b and e), and below-cloud (c and f). DOF for temperature is shown in the left column (a-c) and water vapor in the right column (d-f).

Figure 6.6: Diagonal of the averaging kernel for AERI (a and c) and CrIS (b and d) at select cloud optical depths. Diagonal of the averaging kernels for temperature are shown in a and b, and water vapor is displayed in c and d. Absorption only refers to the LBLDIS calculation that only considers the absorption of the cloud layer and not the contributions from scattering.

Figure 6.7: AERI water vapor Jacobians for clear sky (a), a cloud optical depth of 1 (b), and cloud optical depth of 40 (c).

Figure 6.8: CrIS temperature (a) and water vapor (b) Jacobians for a cloud optical depth of 40.

Figure 6.9: Same as in Figure 6.5 but for a cloud base of 2000 m AGL.

Figure 6.10: Same as in Figure 6.6 but for a cloud base of 2000 m AGL.

Figure 6.11: Same as in Figure 6.5 but for a cloud base of 500 m AGL.

Figure 6.12: Same as in Figure 6.6 but for a cloud base of 500 m AGL.

Figure 6.13: CrIS DOF for temperature (a) and water vapor (b). Above-cloud DOF is represented in black, below-cloud DOF represented in red. For reference, the DOF at the mathematical maximum and minimum sensitivity possible for the given areal cloud fraction are represented with an x. Teal and blue dots represent DOF in cloudy scenario 2 for above-cloud and below-cloud respectively.

Figure 6.14: CrIS+AERI DOF for temperature (a and b) and water vapor (c and d). Above-cloud DOF is presented in a) and c) and below-cloud DOF presented in b) and d). The simulations for AERI in clear sky are presented in black, and AERI in cloudy sky presented in red. For reference, the DOF at the mathematical maximum and minimum sensitivity possible for the given areal cloud fraction are represented with an x. Teal and blue dots represent DOF in cloudy scenario 2 when AERI is in clear sky and when AERI is in cloudy sky respectively.

Figure 7.1: Location of AERI (black square) within the S-NPP CrIS granule for the overpass at approximately 830 UTC on 20 June 2015.

Figure 7.2: A priori covariance matrix used in this analysis. Bottom-left is temperature covaried against itself. Top-right is water vapor varied against itself. Top-left and bottom-right are temperature and water vapor covaried against each other.

Figure 7.3: Temperature (a) and water vapor (b) comparisons of the AERI (purple), CrIS (orange), and CrIS+AERI (green) retrievals to radiosonde observation (black dotted).

Figure 7.4: Differences in temperature (a) and water vapor (b) between the AERI (purple), CrIS (orange), and CrIS+AERI (green) retrievals to the radiosonde observation. Differences are calculated such that a positive difference indicates the retrieval has greater temperature or water vapor than the radiosonde.

Figure 7.5: Vertical resolution of the temperature (a) and water vapor (b) retrievals. AERI is shown in purple, CrIS in orange, and CrIS+AERI in green.

Figure 7.6: 1σ uncertainties of the temperature (a) and water vapor (b) retrievals. AERI is shown in purple, CrIS in orange, and CrIS+AERI in green.

Figure 7.7: As in Figure 7.3 except the retrievals are run with five times greater noise.

Figure 7.8: As in Figure 7.6 except the retrievals are run with five times greater noise.

List of Tables

Table 3.1: Summary of instrumentation considered in this study.

Table 4.1: Overview of radiosonde data considered for this study. Total radiosondes are the number of radiosondes in the ARM archive from 1 October 2013 to 30 September 2019.

Chapter 1: Introduction

Vertical profiles, also referred to as soundings, of atmospheric temperature and water vapor, are critical for atmospheric diagnostics and the accuracy of numerical weather prediction (NWP) (eg: Langland and Baker 2004, LaRoche 2010). Soundings enable the diagnosis of atmospheric stability, total precipitable water vapor, freezing levels, and precipitation type among other applications. Radiosondes are considered the gold standard for atmospheric sounding. However, radiosonde observations are generally taken every 12 hours at locations 100s to 1000s of km apart. The large time and spatial gaps in observations cause the radiosonde network to be unable to identify features in the mesoscale with horizontal length scales around 10 to 100s of km and time scales of a few hours. Of primary concern for this work, the radiosonde network in North America is unable to observe transitions in the planetary boundary layer (PBL) under daytime heating, which is crucial for monitoring changes in atmospheric stability to identify the location and timing of severe convection.

Remotely sensed observations from satellite-based infrared (IR) and microwave sounders and Global Positioning System (GPS) radio occultation, in addition to in situ observations from commercial aircraft, are necessary for filling in the temporal and spatial gaps in radiosonde observations. The current observing system makes use of IR sounders on polar-orbiting satellites. In addition, the Feng-Yun 4 satellite, centered over western Asia, has demonstrated the utility of hyperspectral infrared soundings from geostationary orbit. However, both the National Research Council (2009) and 2017 NASA Decadal Survey (National Academies of Sciences, Engineering, and Medicine, 2018; hereafter referred to as the Decadal Survey) have noted that thermodynamic soundings from the current space-based observing system lack the accuracy and resolution within the PBL that is necessary to improve predictions of high impact weather phenomenon. The

Decadal Survey designated improving observations of the PBL as a priority for the next decade. Previously, the NRC (2009) proposed the development of a nationwide network of ground-based thermodynamic profilers to supplement the space-based sounders in order to improve observations of the PBL. This dissertation will focus on supplementing space-based IR sounders with a ground-based IR sensor in order to improve atmospheric sounding.

1.1 History of Infrared Sounding

Kaplan (1959) is largely credited with developing the initial concept on how to infer atmospheric temperature profiles using IR radiance measurements. Kaplan (1959) used simple radiative transfer simulations to show that radiances measured by a space-based instrument at the 15 μm CO_2 absorption band would originate from approximately 100 hPa. Each channel at an incrementally shorter wavelength would detect radiation originating from a lower level in the atmosphere, until reaching the surface at the 13 μm atmospheric window channel. In 1969, the first two atmospheric sounding instruments were launched into orbit on the Nimbus-3 satellite. One of those instruments, the Satellite Infrared Spectrometer (SIRS) had eight total channels with 5 cm^{-1} resolution spanning between the CO_2 absorption band at 15 μm to the atmospheric window at 11 μm . Wark and Hilleary (1969) applied the theory of Kaplan (1959) to retrieve an estimated temperature profile using a set of eight equations that are solved simultaneously. While the comparison of their retrieval to radiosondes was considered a success at the time, they identified large errors near strong vertical temperature gradient, such as the top of the PBL and the tropopause. Conrath et al. (1970) made a temperature retrieval derived from measurements made by the second instrument on Nimbus-3, the Infrared Interferometer (IRIS), with similar results to Wark and Hilleary (1969). In contrast to SIRS, IRIS provided measurements from 5 μm to 25 μm ,

allowing for the retrieval of total column water vapor and other trace gases in addition to temperature.

Ohring (1979) provided a review of various impact studies that assessed the value that satellite-based sounding data had in numerical weather prediction. In general, satellite-based soundings proved to be useful to improving forecast accuracy in the data-sparse Southern Hemisphere (eg: Kelly et al. 1978) but impacts in the Northern Hemisphere were much smaller. Ohring (1979) also documented mixed reactions to this new satellite-based sounding data: both the South African Weather Bureau and the French Meteorological Service believed that satellite sounding data was considerable and impactful, while the German Meteorological Service would not even assimilate the sounding data because they felt the old system with eight weather ships in the Atlantic Ocean provided more valuable information.

Chahine (1974) and Kaplan et al. (1977) identified that the 4.3 μm CO_2 and N_2O absorption bands may be used to retrieve temperature in the lower troposphere, in addition to the 15 μm region utilized in SIRS. In 1979 the TIROS-N Operational Vertical Sounder (TOVS, Smith et al. 1979) was launched. TOVS was a combination of IR and microwave sounding instruments, of which the High-resolution Infrared Radiation Sounder (HIRS) was the IR component. HIRS had 20 channels, extending those in the 15 μm region that SIRS had, to include channels in the water vapor continuum and the near-IR around those CO_2 and N_2O absorption bands, as was suggested by the findings of Chahine (1974) and Kaplan et al. (1977). In addition to the polar-orbiting HIRS instrument, the Visible and Infrared Spin Scan Radiometer (VISSR) Atmospheric Sounder (VAS, Smith et al. 1981) was put in geostationary orbit on GOES-4 in 1980. The VAS had 12 channels ranging from 4 μm to 15 μm and its geostationary orbit allowed for the detection of temporal changes in thermodynamic profiles at a given location (Smith et al. 1985). Given its geostationary

orbit, VAS also enabled the calculation of upper tropospheric wind vectors, which improved tropical cyclone forecasts (Velden et al. 1984). TOVS remained the polar-orbiting sounder for the United States from 1979 until the launch of the Atmospheric Infrared Sounder (AIRS) in 2002.

Phillips et al. (1979) found that the soundings from TOVS were improved compared to the original SIRS instrument, but still had large errors near strong vertical temperature gradients (as originally found with SIRS by Wark and Hilleary 1969). Smith (1991) showed how the poor vertical resolution of the TOVS retrievals resulted in errors as large as 10 K near the tropopause where the temperature changed rapidly with height. The VAS, using the same channels as the TOVS, also had limited impacts because of the poor vertical resolution. Smith (1991) documented how NWP skill stagnated during the 1980s, coincident in time with the stagnation in sounder technology and suggested that improved sounding would lead to more accurate NWP.

While it took two decades for a new instrument to be put into orbit, scientific achievements during the 1980s and 1990s cultivated the successes that would come in the 2000s. Notably, advances in engineering enabled the development of hyperspectral interferometers and grating spectrometers. While the early SIRS and IRIS instruments had spectral resolution of 5 cm^{-1} , and the HIRS instrument had 10 cm^{-1} resolution, newer instruments, such as the aircraft-based High spectral resolution Infrared Sounder (HIS) were able to achieve spectral resolution of 1 cm^{-1} or better. Hyperspectral resolution is necessary to differentiate between the transparent and opaque regions of individual absorption bands, crucial for high vertical resolution sounding. The hyperspectral resolution sharpens the weighting functions for each channel – that is sensitive to a thinner layer of the atmosphere (Kaplan et al. 1977, Smith 1991). Smith (1991) presented experimental data from the HIS when flown on an aircraft, with the sensor looking downward. In

this setting, HIS was capable of doubling the vertical resolution of the TOVS and reducing errors in the temperature retrievals by up to 50% compared to TOVS.

The launch of AIRS in 2002 (still operational in 2021) marked the beginning of the current era for IR sounding. AIRS is a grating spectrometer with more than 2000 channels and a spectral resolution ranging from 0.55 cm^{-1} , in the longwave part of the spectrum to 2.0 cm^{-1} in the shortwave. This was a significant upgrade from the 15 cm^{-1} spectral resolution of the HIRS instrument. Early validation efforts by Chahine et al. (2006) found that AIRS retrievals achieved root mean square errors (RMSE) of about 1.5 K or less throughout the troposphere. For comparison, the RMSE values for TOVS presented by Smith (1991) were 2.5 K to 3 K and greater throughout the profile. An IR sounder capable of significantly more accurate retrievals addressed the primary areas of focus for the IR sounding community that Smith (1991) had highlighted a decade earlier.

Today, AIRS along with the Infrared Atmospheric Sounding Interferometer (IASI), first launched by EUMETSAT in 2006, and the Cross-track Infrared Sounder (CrIS), first launched by the United States National Aeronautics and Space Administration (NASA) and National Oceanic and Atmospheric Administration (NOAA) in 2011, provide IR soundings from polar-orbit. Until recently, hyperspectral sounders have been restricted to polar-orbit. In 2016, the Chinese Meteorological Agency (CMA) launched the Geostationary Interferometric Infrared Sounder (GIIRS), to be the first hyperspectral sounder in geostationary orbit. EUMETSAT currently plans to put the Infrared Sounder (IRS) in geostationary orbit by 2023 as part of the Meteosat Third Generation (MTG) deployment while NOAA's GEO-XO program intends to put an IR sounder in geostationary orbit around 2038. The reader is directed to Menzel et al. (2018) for an additional perspective on the history and development of IR sounding instruments.

While modern day NWP assimilates radiances from IR sounders instead of retrievals, Smith et al. (2021) demonstrates that there is much more information available in these IR sounders than is currently being used in data assimilation techniques. However, thermodynamic retrievals from IR sounders are used for nowcasting and have the potential to provide important information on the pre-convective state of the atmosphere (Iturbide-Sanchez et al. 2018, Esmaili et al. 2020). That potential has yet to be realized though, as extensive validations of the NOAA Unique Combined Atmospheric Processing System (NUCAPS, Gambacorta 2013) by Sun et al. (2017) and Nalli et al. (2018) reveal large errors up to 3 K near the surface. Gartzke et al. (2017) and Bloch et al. (2019) have shown that calculations of Convective Available Potential Energy (CAPE) from AIRS retrievals have no correlation to CAPE calculations from radiosondes, largely driven by the near surface errors in the retrievals. Despite the many technological and scientific advances in the IR sounding field over the last 50+ years, thermodynamic sounding of the PBL from space remains challenging, just as Wark and Hilleary (1969) had found in the first known sounding efforts. These errors significantly limit the use of IR soundings in modern day weather forecasting and analysis.

1.2 Motivation

Figure 1.1 shows an example of a CrIS-derived retrieval from NUCAPS (Gambacorta 2013) compared to a collocated radiosonde. The NUCAPS minus radiosonde difference is less than 1.5 K above 700 hPa, and less than 2.0 g kg⁻¹ above 800 hPa. From the surface to 800 hPa, however, differences are much greater, 2 – 3 K and 4 – 5 g kg⁻¹ in this example. In particular, the errors below 800 hPa cause the NUCAPS retrieval to completely miss the existence of the

nocturnal inversion centered at 875 hPa. These retrieval errors in the PBL significantly reduce the utility of these soundings in operational weather forecasting.

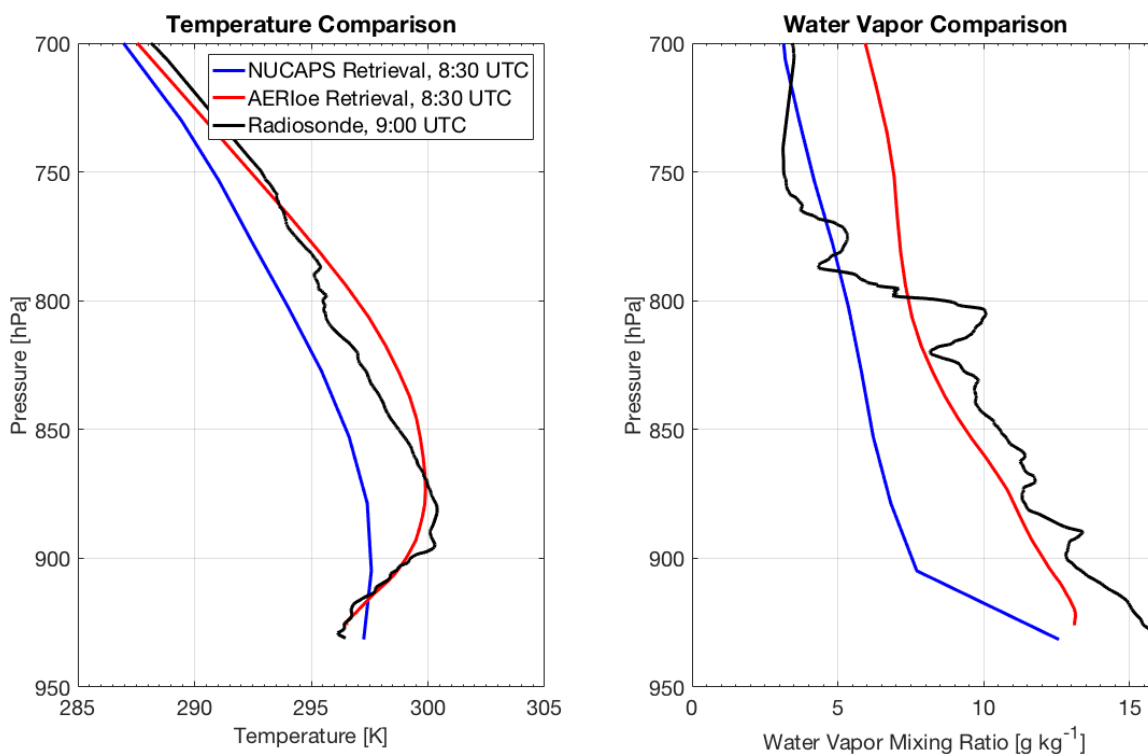


Figure 1.1: Comparison of AERIOe (AERI-derived, red), NUCAPS (CrIS-derived, blue), and radiosonde (black) profiles of temperature (left) and water vapor mixing ratio (right) on 20 June 2015.

Given these weaknesses of the space-based observing system at sounding the PBL, the Decadal Survey made it a priority to improve observations of the PBL. The NRC (2009) proposed the development of a nationwide network of ground-based thermodynamic profilers to supplement the space-based sounders and improve observations of the PBL. The Atmospheric Emitted Radiance Interferometer (AERI, Knuteson et al. 2004a,b) is one of the instruments that would fit the criteria outlined by the NRC (2009) for the hypothetical network of ground-based profilers (Hoff and Hardesty, 2012). AERI is a Michelson interferometer that measures downwelling atmospheric emitted radiances between 520 and 3000 cm^{-1} (19.2 to $3.3\text{ }\mu\text{m}$) and has been demonstrated to achieve an absolute radiometric accuracy of better than 1% of the ambient

radiance (Knuteson et al. 2004a,b). AERI has been widely used in PBL studies including monitoring convective indices (Feltz et al. 2003, Wagner et al. 2008) and gravity waves in the PBL (Tanamachi et al. 2008, Loveless et al. 2019). AERI has been deployed around the world as part of the ARM Program (Mlawer and Turner 2016) and has provided observations critical for improving and validating radiative transfer modelling (Mlawer et al. 2016). Figure 1.1 also displays the AERIOe (Turner and Löhnert 2014, Turner and Blumberg 2019) retrieval for the same time and location as the radiosonde/NUCAPS matchup. While NUCAPS had its greatest differences near the surface, the AERIOe retrieval has a difference of less than 1 K up to 850 hPa, and less than 2 g kg⁻¹ up to 800 hPa. This is in line with the larger validation performed in Turner and Löhnert (2014).

Conceptually, the benefits of a combination of a space-based sounder with a ground-based profiler are intuitive. Satellite-based sounders have low information content near the surface but greater sensitivity in the middle and upper-troposphere (eg: Ebell et al. 2013, Smith and Barnett 2020). Meanwhile, ground-based sounding instruments such as AERI or a microwave radiometer are almost exclusively sensitive to the lowest 4 km of the troposphere (eg: Löhnert et al. 2009, Turner and Löhnert 2014, Blumberg et al. 2015). The optimal combination of an upward-pointing sensor and a downward-pointing satellite-based sensor would permit each system's strengths to be represented in the final retrieved profile.

Given the well-established retrieval methods for using IR or microwave radiance measurements to produce estimated profiles of thermodynamic variables, one potential method to combine the two sets of measurements would be an *a posteriori* combination of the single-instrument retrievals based on the uncertainties of each individual system. Aires et al. (2012) tested this theory for a combination of space-based IR and microwave sounders, comparing a synergy

(both instruments in the same retrieval) to a combination of the individual retrievals, using the retrieval with the lesser uncertainty at a given height. They found that the synergy displays greater improvements than a combination of single-instrument retrievals. This is because the combined retrieval allows the shared information content of the two sets of measurements to interact within the retrieval process and improve the accuracy of the retrieval. Ebell et al. (2013) showed that information content for a ground-based microwave radiometer plus the space-based Infrared Atmospheric Sounding Interferometer (IASI) would be nearly double that of a ground-based microwave radiometer alone. This provides the basis for the underlying hypothesis for this dissertation: *by adding ground-based sensors to the satellite observing system, thermodynamic soundings of the PBL will be greatly improved and will approach the desired accuracy and resolution outlined by the 2017 Decadal Survey.*

1.3 Background on Instrument Synergy Studies

Instrument synergies have become common practice in situations where multiple instruments are making simultaneous observations of the same environment (such as collocated instruments at research facilities or on the same satellite platform). Löhnert et al. (2009) demonstrated a synergy between the ground-based AERI and a ground-based microwave radiometer finding that the microwave radiometer provides additional information to the AERI in high moisture environments, when the IR signal from the AERI is attenuated. Turner and Blumberg (2019) experimented with the synergy between a water vapor Differential Absorption Lidar (DIAL) and AERI. Despite the DIAL only offering information on water vapor, combining AERI with the DIAL actually improves both the temperature and water vapor retrieval compared to AERI alone. In space, IR and microwave sounders have been flown together on the same

satellite since the launch of TOVS in 1979. The current NUCAPS retrieval utilizes a retrieval from a microwave sounder as a first guess for the IR retrieval in clear sky conditions. In cloudy sky conditions, NUCAPS will supplement the IR retrieval (which can retrieve above the cloud layer) with the microwave retrieval below the cloud layer.

Despite the wide-spread use of instrument synergies from the same research facility or satellite platform, limited research has been done combining space-based and ground-based sensors together. Both Gartzke et al (2017) and Bloch et al. (2019) showed that calculations of Convective Available Potential Energy (CAPE) from space-based retrievals had poor correlations with CAPE calculated from radiosondes. By replacing the estimate of temperature and water vapor at the surface from the retrieval with a surface observation, the correlation with radiosonde calculations was drastically improved.

The aforementioned study by Ebell et al. (2013) compared information content for space-based IASI with a ground-based microwave radiometer. They found that the combination of IASI with the ground-based microwave radiometer nearly doubled the total information content of both temperature and water vapor compared to the ground-based microwave radiometer alone. Specifically, the combination with IASI resulted in small increases in information content near the surface, even though the ground-based microwave radiometer was found to have significantly greater information in that layer than IASI. The synergy also resulted in significant reductions in uncertainties: in particular a 20% reduction in near-surface uncertainties for absolute humidity. Overall, their results proved that the synergy of space-based and ground-based instruments had greater information content and smaller uncertainties than either instrument individually: the same result that Aires et al. (2012) found for a synergy of two space-based sensors.

Ho et al. (2002) developed a synergistic retrieval between the downward-looking, aircraft-mounted Scanning High-resolution Interferometer Sounder (S-HIS) with the ground-based AERI. Compared to radiosonde measurements, the combined AERI+S-HIS retrieval displayed a decrease of 1.5 K in root mean square error (RMSE) in the near surface layer versus the S-HIS alone. Near-surface water vapor mixing ratio retrievals improved from RMSE of about 2.5 g kg⁻¹ to about 1.5 g kg⁻¹ for the combined retrieval.

Toporov and Löhnert (2020) utilized a synthetic retrieval (based on reanalysis data) combining simulated measurements for IRS (EUMETSAT's future geostationary IR sounder) with those of a ground-based microwave radiometer. Similar to the findings of Gartzke et al. (2017) and Bloch et al. (2019), they found that CAPE calculated from IRS had only had a correlation of 0.68 to the true CAPE. The ground-based microwave radiometer alone had a correlation of 0.77. However, when combined in a synergistic retrieval, the two sensors had a correlation of 0.84 to the true CAPE in clear sky conditions. They also demonstrated that the combination of the two sensors performed well at identifying temporal changes in CAPE, while the IRS alone struggled to identify periods of very high CAPE.

The results of Ebell et al. (2013) and Toporov and Löhnert (2020) suggest that a synergy of space-based sounders with ground-based sensors will significantly improve remotely sensed soundings of the atmosphere. However, Ebell et al. (2013) used a small sample size of only 100 profiles. Toporov and Löhnert (2020) had a larger sample size, but only documented the improvements in retrievals based on the accuracy of convective indices derived from those retrievals. Both of these studies focused on assessing the ground-and-space-based synergy within atmospheric conditions found in western Europe. This dissertation has three goals that will expand

upon the work presented by Ebell et al. (2013) and Toporov and Löhnert (2020) in order to further quantify the benefits of a synergy of ground-based and space-based sensors:

1) Expand upon the clear sky analysis of Ebell et al. (2013) to consider conditions from multiple climate regimes and document improvements in vertical resolution with the ground-and-space-based synergy.

2) Assess information content of the ground-and-space-based synergy in cloudy sky environments using three case studies with varying cloud heights

3) Create a ground-and-space-based synergistic retrieval in order to demonstrate that the improvements suggested by the information content studies may appear in practice.

Chapter 2: Retrieving Thermodynamic Information from Radiance Measurements

Hyperspectral sounders make radiance measurements of upwelling (from aircraft or space-based platforms) or downwelling (from ground-based platforms) atmospheric emitted radiation at spectral resolutions around 1 cm^{-1} or better. By utilizing prior estimates of the atmosphere (referred to as an a priori), the emission from trace gases such as water vapor, CO_2 , and O_3 , at particular frequencies enable the retrieval of thermodynamic information from these radiance measurements. An example of IR radiance measurements from the ground-based AERI and the space-based CrIS are shown in Figure 2.1. One thing to note about Figure 2.1 is how the observed spectra from the two instruments are largely mirrors of each other. For example, consider the CO_2 absorption band near 700 cm^{-1} . In this region, AERI's radiance is greater than CrIS's due to the strong opacity of the atmosphere in this spectral region: the AERI observations are sensitive to the warm near-surface air immediately adjacent to the sensor while the CrIS observations can only observe the cold upper troposphere and stratosphere as the atmosphere is completely opaque below those levels. The opposite pattern is observed in the relatively transparent window channels between 800 cm^{-1} and 1000 cm^{-1} , where CrIS is most sensitive to the warm surface and AERI has little sensitivity to any part of the atmosphere in this region. Clearly, by combining upward-pointing and downward-pointing views of the atmosphere from these two instruments, a more complete view of the atmosphere emerges than what is possible from a single instrument. The retrieval process originally outlined by Kaplan (1959) assigned the brightness temperature of a single channel as the temperature at a given level. However, that process has many flaws and limited applications as the radiances at each spectral channel are frequently highly correlated with each

other and are sensitive to many layers of the atmosphere, not just a single layer. Because of this, the retrieval process is non-linear and has an infinite number of potential solutions that exist for a given set of radiance measurements. As a result, iterative numerical methods that utilize prior estimates of the atmosphere are required to retrieve thermodynamic information from radiance measurements.

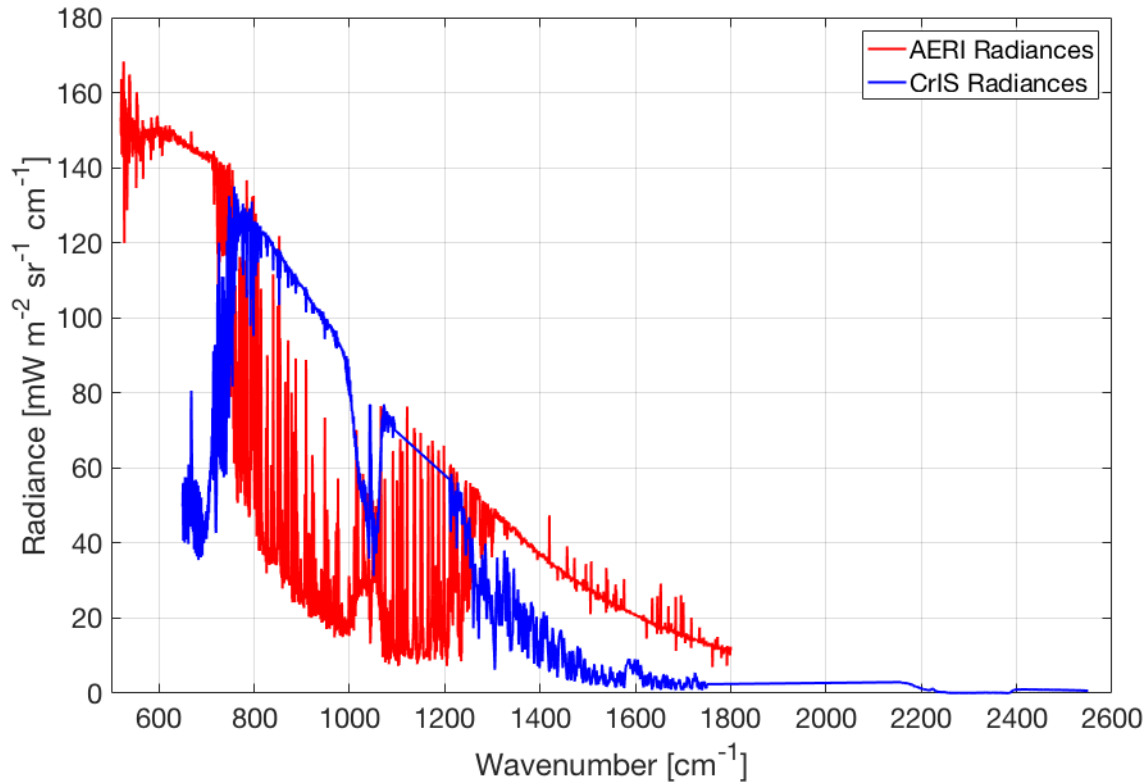


Figure 2.1: Radiances for the upward looking AERI (red) and downward looking CrIS (blue).

2.1 Gauss-Newton Estimation

Turner and Löhnert (2014) describe a Gauss-Newton optimal estimation retrieval using AERI, and a similar approach will be made here in order to demonstrate the synergy of the ground-based AERI with space-based IR sounders. A simplified derivation of the Gauss-Newton method described in Rodgers (2000) is presented here, along with the modifications to the method suggested by Turner and Löhnert (2014). In order to relate the measurement vector y to the

atmospheric state vector x , a forward model F is needed to physically relate the two. In this case, y is an m -dimensional vector of radiance observations while x is an n -dimensional vector that contains the temperature and moisture profiles. In essence, our goal is to take our observations of y and return the most likely values of x that are physically capable of producing y . We can describe this system in the following manner:

$$y = F(x) + \varepsilon \quad (2.1)$$

where ε is the error vector, encompassing both instrument noise and errors of the forward model. Linearizing this system about a reference state x_0 will yield:

$$y = F(x_0) + \left. \frac{\partial F(x)}{\partial x} \right|_{x=x_0} (x - x_0) + \varepsilon \quad (2.2)$$

where the Jacobian matrix, commonly referred to as the weighting function matrix, \mathbf{K} can be defined as the partial derivative of each element of the forward model with respect to each element of the state vector x :

$$\mathbf{K}_{j,k} = \frac{\partial F_j(x)}{\partial x_k} \quad (2.3)$$

where j is an index of the measurement y and k is an index of the state vector x . \mathbf{K} is a m by n matrix where m is the number of measurements and n is the number of elements in the state vector x . \mathbf{K} describes the sensitivity of each element of the measurement vector y to each element of the state vector x . Substituting \mathbf{K} into equation 2.2 and rearranging some terms:

$$y - F(x_0) = \mathbf{K}(x - x_0) + \varepsilon. \quad (2.4)$$

For IR sounders making thermodynamic retrievals, the number of measurements m is typically greater than the number of elements in the state vector x , which would technically make this problem over-determined if the measurements were independent from one another. For example, AERI has 2655 channels and we can consider AERIOe (Turner and Löhnert 2014) which will retrieve temperature and water vapor at 55 different levels in the atmosphere, resulting in a state

vector with 110 elements. However, the measurements are not independent of one another, but rather highly correlated. This can be seen in Figures 2.2a and 2.2b which displays the temperature Jacobians for AERI and CrIS respectively. The Jacobians show how each measurement is sensitive to many layers instead of just one. Because the measurements are correlated with one another, there is actually far less information than the number of measurements. As will be shown later, these measurements result in about 5 independent pieces of information about temperature from the surface to 200 hPa. Comparatively, there are approximately 40 levels in the grid used for these calculations, so 40 elements in the state vector. Thus, this retrieval process is actually ill-posed or under-determined because there is less information than the number of variables we are seeking to retrieve. This results in a problem where an infinite number of solutions for x may be physically possible given measurement y and therefore requires a prior estimate of the atmosphere in order to overcome that lack of information compared to number of variables being retrieved.

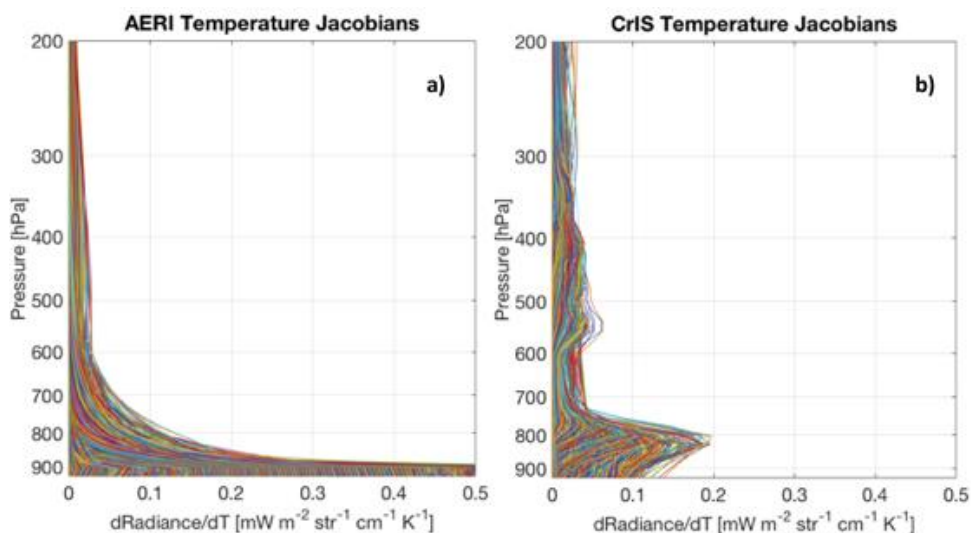


Figure 2.2: Temperature Jacobians for AERI (a) and CrIS (b).

Because there are an infinite number of solutions, the retrieval process is inherently a conditional probability problem: given some measurement y what is the most likely solution for the state vector x ? We can consider Bayes' Theorem for conditional probability:

$$P(x|y) = \frac{P(y|x)P(x)}{P(y)} \quad (2.5)$$

which describes the probability of the state vector being x given some measurement y . $P(x)$ is the prior probability distribution function (*pdf*) of the state vector. This is what is known about x before a measurement is made (e.g.: a climatology). $P(y)$ is the prior of the measurement before the measurement is made. $P(y|x)$ is the probability of measurement y given some state vector x . If we assume that the errors of our linearized system (described in equation 2.4) are Gaussian in distribution, then we can describe $P(y|x)$ as:

$$-2 \ln P(y|x) = (y - \mathbf{K}x)^T \mathbf{S}_\varepsilon^{-1} (y - \mathbf{K}x) + c_1 \quad (2.6)$$

where \mathbf{S}_ε is the error covariance matrix. We can also describe $P(x)$ as:

$$-2 \ln P(x) = (x - x_a)^T \mathbf{S}_a^{-1} (x - x_a) + c_2 \quad (2.7)$$

where x_a is the a priori and \mathbf{S}_a is the a priori covariance matrix. \mathbf{S}_a is calculated as:

$$\mathbf{S}_a^{j,k} = \text{CORR}(x_j, x_k) \sigma_{xj} \sigma_{xk}. \quad (2.8)$$

where σ_{xj} and σ_{xk} are the standard deviation of the atmospheric state (temperature or water vapor mixing ratio) at height levels j and k respectively, and $\text{CORR}(x_j, x_k)$ is the correlation between the atmospheric state at height levels j and k . The constants c_1 and c_2 in equations 2.6 and 2.7 are both independent of x and are important for normalizing these *pdfs*. If we substitute equations 2.6 and 2.7 into Bayes' Theorem in equation 2.5 we can determine the *pdf* for what we are interested in, which is the conditional probability of a state vector x given some measurement y , $P(x|y)$:

$$-2 \ln P(x|y) = [y - F(x)]^T \mathbf{S}_\varepsilon^{-1} [y - F(x)] + [x - x_a]^T \mathbf{S}_a^{-1} [x - x_a] + c_3 \quad (2.9)$$

Since we are looking for the most likely solution, we maximize the probability by taking the derivative of equation 2.9 and setting it equal to zero:

$$\nabla_x [-2 \ln P(x|y)] = -[\nabla_x F(x)]^T \mathbf{S}_\varepsilon^{-1} [y - F(x)] + \mathbf{S}_a^{-1} [x - x_a] = 0 \quad (2.10)$$

We can substitute $\mathbf{K}(x) = \nabla_x F(x)$:

$$-[\widehat{\mathbf{K}}(\hat{x})]^T \mathbf{S}_\varepsilon^{-1}[y - F(\hat{x})] + \mathbf{S}_a^{-1}[\hat{x} - x_a] = 0 \quad (2.11)$$

where $\hat{\cdot}$ indicates an estimated variable. In particular, \hat{x} represents the most likely state vector given measurement y . While we can solve for \hat{x} in equation 2.11, the non-linearity of the system requires an iterative method to minimize the difference between the measurement y and the modeled measurement given our estimated state \hat{x} . We consider Newton's method for a general vector equation $\mathbf{g}(x) = 0$:

$$x_{i+1} = x_i - [\nabla_x \mathbf{g}(x_i)]^{-1} \mathbf{g}(x_i). \quad (2.12)$$

where i is the iteration number. Substituting the left-hand side of equation 2.11 for $\mathbf{g}(x)$:

$$\nabla_x \mathbf{g}(x) = \mathbf{S}_a^{-1} + \mathbf{K}^T \mathbf{S}_\varepsilon^{-1} \mathbf{K} - [\nabla_x \mathbf{K}^T] \mathbf{S}_\varepsilon^{-1} [y - F(x)] \quad (2.13)$$

Note that the $\nabla_x \mathbf{K}$ term is a second derivative of the forward model (recall the definition of \mathbf{K} in equation 2.3). For cases that are not too non-linear, this term is small and can be ignored. We can substitute equations 2.11 and 2.13 into equation 2.12 and find the Gauss-Newton Method:

$$x_{i+1} = x_i + (\mathbf{S}_a^{-1} + \mathbf{K}_i^T \mathbf{S}_\varepsilon^{-1} \mathbf{K}_i)^{-1} [\mathbf{K}_i^T \mathbf{S}_\varepsilon^{-1} (y - F(x_i)) - \mathbf{S}_a^{-1} (x_i - x_a)]. \quad (2.14)$$

This equation provides x at the next iteration $i+1$ based on x at the current iteration i . This method will move incrementally toward the final solution for x (which is the most likely solution given measurements y). Because \mathbf{K} is a function of the state vector x , it should be re-evaluated at each iteration such that \mathbf{K}_i is the Jacobian evaluated at x_i . Masiello et al. (2012) and Turner and Löhnert (2014) utilize a γ factor to weight the prior information relative to the observations. This factor is used to change the weight of the prior information compared to the observation. This acts to stabilize the retrieval, as γ is initially large and is decreased in value with each iteration (e.g.: 1000, 300, 100, 30, 10, 3, 1, 1...), slowly allowing more information from the observation to be used in each successive iteration until $\gamma = 1$. We will also consider the departure of our final solution x_{i+1}

from the a priori x_a instead of x_i and rearrange some terms to provide us the final equation for our Gauss-Newton optimal estimation method:

$$x_{i+1} = x_a + (\gamma \mathbf{S}_a^{-1} + \mathbf{K}_i^T \mathbf{S}_\varepsilon^{-1} \mathbf{K}_i)^{-1} \mathbf{K}_i^T \mathbf{S}_\varepsilon^{-1} [(y - F(x_i)) - \mathbf{K}_i(x_i - x_a)]. \quad (2.15)$$

Following Turner and Löhnert (2014), the retrieval is deemed to converge when:

$$(x_{i+1} - x_i)^T \mathbf{S}^{*-1} (x_{i+1} - x_i) \ll N. \quad (2.16)$$

where N is the number of variables in the state vector and \mathbf{S}^* is the posterior error covariance matrix. Physically speaking, the retrieval is deemed to have converged when the change in x from one iteration to the next is smaller than the uncertainties of the retrieval. Note that the posterior error covariance matrix is typically referred to as \mathbf{S} , however in order to avoid confusion with the traditional Rodgers (2000) formulation of \mathbf{S} which will be used in the next section discussing information content, we will refer to the error covariance matrix for the modified Gauss-Newton method as \mathbf{S}^* :

$$\mathbf{S}^* = (\gamma \mathbf{S}_a^{-1} + \mathbf{K}_i^T \mathbf{S}_\varepsilon^{-1} \mathbf{K}_i)^{-1} (\gamma^2 \mathbf{S}_a^{-1} + \mathbf{K}_i^T \mathbf{S}_\varepsilon^{-1} \mathbf{K}_i) (\gamma \mathbf{S}_a^{-1} + \mathbf{K}_i^T \mathbf{S}_\varepsilon^{-1} \mathbf{K}_i)^{-1}. \quad (2.17)$$

When $\gamma = 1$, \mathbf{S}^* will collapse to equal the traditional version of \mathbf{S} presented by Rodgers (2000).

A radiosonde climatology will be used for the first guess x_a and a priori covariance matrix \mathbf{S}_a . Since model errors are difficult to quantify, the noise characteristics for each instrument, to be described in Table 3.1, will be used for \mathbf{S}_ε . This will result in an underestimation of the uncertainties of the retrieval. Smith et al. (2021) suggests performing a dry temperature retrieval on bands not sensitive to water vapor, and then performing the water vapor retrieval with the knowledge of the temperature profile. However, this method would omit temperature information contained in the water vapor channels. We choose to follow the decisions of Ebell et al. (2013) and Turner and Löhnert (2021) and calculate the averaging kernel \mathbf{A} for both temperature and

water vapor simultaneously. Chapter 6 will demonstrate the optimal estimation retrieval for a synergy of the ground-based AERI and space-based CrIS.

2.2 Information Content

Instrument studies will often quantify the information content that an instrument can provide to a retrieval. Information content is a convenient measure to compare instruments without the computational complexities of an iterative retrieval. For example, the Jacobian matrix only needs to be computed once when calculating information content but multiple times in the retrieval method. Chapters 4 and 5 will assess information content of the ground-and-space-based synergy in clear sky and cloudy sky environments, respectively. There are several methods that may be used to compute information content of an instrument (such as change in entropy or Shannon information content) but in this study we will compute degrees of freedom (DOF) because it is calculated using variables that are already needed for the optimal estimation retrieval. Following Rodgers (2000), we know the Bayesian solution for the retrieved state in a linear system is:

$$\hat{x} = x_a + (\mathbf{K}^T \mathbf{S}_\varepsilon^{-1} \mathbf{K} + \mathbf{S}_a^{-1})^{-1} \mathbf{K}^T \mathbf{S}_\varepsilon^{-1} (y - \mathbf{K}x_a). \quad (2.18)$$

We can see that the retrieved solution \hat{x} is a function of the prior knowledge of the state (x_a) and the change to that prior expected value as contributed by the measurement. The second term on the right-hand side of equation 2.18 is commonly called the gain matrix \mathbf{G} :

$$\mathbf{G} = (\mathbf{K}^T \mathbf{S}_\varepsilon^{-1} \mathbf{K} + \mathbf{S}_a^{-1})^{-1} \mathbf{K}^T \mathbf{S}_\varepsilon^{-1} \quad (2.19)$$

The gain matrix \mathbf{G} is composed of the posterior error covariance matrix \mathbf{S} , which is spread across the instrument space by the Jacobian \mathbf{K} and the instrument noise \mathbf{S}_ε :

$$\mathbf{S} = (\mathbf{K}^T \mathbf{S}_\varepsilon^{-1} \mathbf{K} + \mathbf{S}_a^{-1})^{-1}. \quad (2.20)$$

The diagonal elements of the posterior error covariance matrix \mathbf{S} provide the expected uncertainties of the retrieved state vector x . The posterior uncertainties are a function of the instrument noise (spread across the state space by \mathbf{K}) and the uncertainties of the a priori. This may also be calculated for an iterative retrieval by evaluating \mathbf{K} at state vector x_i (referred to as \mathbf{K}_i in the previous section). This leads us to the averaging kernel \mathbf{A} which may be calculated as:

$$\mathbf{A} = \mathbf{G}\mathbf{K} = \mathbf{S}(\mathbf{K}^T\mathbf{S}_\varepsilon^{-1}\mathbf{K}). \quad (2.21)$$

The averaging kernel \mathbf{A} describes the subspace of the state in which the retrieval must lie and thus, contains descriptions of the information content in a retrieval. In essence, \mathbf{A} is the contribution of the measurement (\mathbf{G}) spread out over the state space based on the sensitivity of the measurement to changes in the state, which is the Jacobian \mathbf{K} .

From the averaging kernel \mathbf{A} , two variables can be computed that we will center our information content analyses on. First, the DOF is calculated as the trace (or the sum of the diagonal elements) of \mathbf{A} :

$$\text{DOF} = \text{Trace}(\mathbf{A}) \quad (2.22)$$

Given the relation to the gain matrix \mathbf{G} , DOF quantifies the additional information contributed to the retrieval due to a signal from the instrument beyond what is already known from the prior. This allows us to compare differences in information provided by different instruments and different instrument synergies, as has been previously shown in Ebell et al. (2013) as well.

Second, the averaging kernel \mathbf{A} may also be used to derive the vertical resolution. Physically speaking, the vertical resolution describes the depth of the atmospheric layer contributing to the measured signal that is being used to estimate the atmospheric state at a given level. Following Hewison (2007) the vertical resolution may be approximated by scaling the

inverse of the diagonal elements of \mathbf{A} (note: the same elements that get summed to calculate DOF) by the vertical spacing of the grid:

$$\mathbf{Vres}_j = \frac{z_{(j-1)} - z_{(j+1)}}{A_{j,j}} \quad (2.23)$$

where z is the height. Note that the vertical resolution cannot exceed the resolution of the grid used for radiative transfer calculations. The instrument noise described in Table 3.1 in the next chapter will be used for the error covariance matrix \mathbf{S}_ε . This will result in an over-estimation of information content and vertical resolution, and underestimate the uncertainties described by the posterior error covariance matrix \mathbf{S} since additional sources of error (such as errors in the forward model) are unaccounted for.

Chapter 3: Instrumentation

This dissertation utilizes IR instruments to study a synergy of ground-based and space-sensors for thermodynamic sounding. While microwave sensors have the advantage of non-precipitating clouds being largely transparent at the frequencies used for microwave sounding, this dissertation focuses on the IR because of both the greater vertical resolution and smaller footprints (allowing for a better match up with the point observations of a ground-based sensor) offered by IR sounders compared to microwave sounders. Table 3.1 is a summary of the instrumentation considered in this study, which includes five different space-based IR instruments along with the ground-based AERI. We include three polar-orbiting space-based hyperspectral IR sounders: The Atmospheric Infrared Sounder (AIRS) on the Aqua spacecraft, the Cross-track Infrared Sounder (CrIS) flown on Suomi NPP and NOAA-20, and the Infrared Atmospheric Sounding Interferometer (IASI) onboard MetOp A, B, and C. With the potential for hyperspectral IR sounding from geostationary orbit becoming a key component of the future observing suite, we include the proposed Geosynchronous Imaging Fourier Transform Spectrometer (GIFTS, described in Elwell et al. 2006) to explore the benefits of soundings from geostationary orbit when combined with improved by ground-based systems. Lastly, we utilize the 12 IR channels on the Advanced Baseline Imager (ABI) as the only current instrument in geostationary orbit over North America offering measurements that could be used for sounding information to provide a baseline for comparison. The noise characteristics for each instrument described in Table 3.1 will make up the error covariance matrix \mathbf{S}_ε used in both the optimal estimation retrieval (equation 2.15) and in the calculation of the averaging kernel (equation 2.21).

Instrument	Platform	Orbit-type	Spectral Range	Range of Instrument Noise ($\text{mW m}^{-2} \text{sr}^{-1} \text{cm}^{-1}$)	Noise Reference
<i>ABI</i>	GOES-16, GOES-17	Geostationary	3.90, 6.19, 6.93, 7.34, 8.44, 9.61, 10.33, 11.21, 12.29, 13.28 μm	0.0038 to 0.52	Schmidt et al. 2017
<i>AERI</i>	Multiple locations	Ground-based	520 - 1800 cm^{-1}	0.01 to 1.8	Löhnert et al. 2009
<i>AIRS</i>	Aqua	Polar	649 - 2665 cm^{-1}	0.0015 to 0.79	Pagano et al. 2014
<i>CrIS</i>	S-NPP, NOAA-20	Polar	650 - 1095 cm^{-1} , 1210 - 1750 cm^{-1} , 2155 - 2550 cm^{-1}	0.1, 0.04, 0.005	Zavyalov et al. 2013
<i>GIIRS/GIFS</i>	Feng-Yun 4 /Proposed	Geostationary	700 - 1130 cm^{-1} , 1650 - 2250 cm^{-1}	GIFTS noise: 0.4, 0.06	Elwell et al. 2006
<i>IASI</i>	MetOp-A, B, C	Polar	645 - 2760 cm^{-1}	0.005 to 0.45	Hilton et al. 2012

Table 3.1: Summary of instrumentation considered in this study.

AIRS (launched in 2002 on the Aqua satellite) and CrIS (launched in 2011 on Suomi-NPP and in 2017 on NOAA-20) are part of the A-Train (Stephens et al. 2018) with an approximate 1:30 pm local time equator overpass. AIRS (Chahine et al. 2006) is a grating spectrometer with 2378 channels spanning 650 to 2665 cm^{-1} . AIRS has a noise equivalent differential temperature ranging from 0.1 to 0.7 K, described in Figure 5 of Pagano et al. (2014). CrIS (Han et al. 2013) is a Michelson interferometer with three distinct spectral bands ranging from 650 to 1095 cm^{-1} with spectral resolution of 0.625 cm^{-1} , 1210 to 1750 cm^{-1} with spectral resolution of 1.25 cm^{-1} , and 2155 to 2550 cm^{-1} with spectral resolution of 2.5 cm^{-1} . CrIS noise is described in Figure 1 of Zavyalov et al. (2013), ranging from approximately 0.1 $\text{mW m}^{-2} \text{sr}^{-1} \text{cm}^{-1}$ in the long- and midwave bands, and about 0.01 $\text{mW m}^{-2} \text{sr}^{-1} \text{cm}^{-1}$ in the third band.

IASI, first launched in 2006, is deployed on MetOp-A, -B, and -C with equator overpass times of approximately 9:30am local time. IASI is similar to CrIS in that it is also a Michelson interferometer. It provides continuous coverage of the radiative spectrum from 645 to 2760 cm^{-1} at a spectral resolution of 0.25 cm^{-1} . IASI's noise equivalent differential temperature is described in Figure 3 of Hilton et al. (2012), and ranges from 0.3 K to 0.5 K at a reference temperature of

280 K. This results in noise ranging from approximately 0.1 to $0.45 \text{ mW m}^{-2} \text{ sr}^{-1} \text{ cm}^{-1}$ in the long- and midwave bands, and 0.1 to $0.01 \text{ mW m}^{-2} \text{ sr}^{-1} \text{ cm}^{-1}$ in the shortwave bands. While AIRS, CrIS and IASI are very similar instruments, we consider all three as part of our study because they differ in spectral resolution and error characteristics, which could result in different impacts on information content and the resulting synergy with ground-based instruments.

While the ABI, on GOES-16 and GOES-17, only offers 12 IR broadband measurements over wider spectral bands, it is the only instrument in geostationary orbit over the United States at this time that provides thermodynamic sounding information. The broadband channels on ABI have broad sensitivity across a large depth of the atmosphere and provide little information for sounding compared to the hyperspectral sounders. However, the nearly continuous observations from ABI over the United States would mean that the benefits of a ground-based synergy would not be limited to specific overpass times.

Given the community interest in moving towards IR sounding from geostationary orbit, we consider the Geostationary Interferometric Infrared Sounder (GIIRS) that is currently in geostationary orbit on the Feng-Yun 4 satellite (Yang et al. 2017). Work by Elwell et al. (2006) assessing noise characteristics of a different hyperspectral IR sounder for geostationary orbit suggest that GIIRS has greater noise than expected. Thus, we utilize noise characteristics of the GIFTS instrument, a prototype geostationary IR sounding instrument studied by NASA, the University of Wisconsin-Madison, and Utah State University (Elwell et al. 2006) in conjunction with the GIIRS spectral channels. The noise characteristics of GIFTS are closer to what is expected from the future geostationary sounders proposed by EUMETSAT and NOAA's GEO-XO program. We denote this hypothetical instrument as GIFTS throughout this paper to avoid confusion with the full characteristics of the GIIRS instrument.

The ground-based instrument of focus in this study is the AERI. The AERI is also a Michelson interferometer, similar to CrIS and IASI, that measures downwelling atmospheric emitted radiance between 520 and 3000 cm^{-1} at approximately 1 cm^{-1} resolution at better than 99% radiometric accuracy (Knuteson et al. 2004 a,b). The temporal resolution of the AERI is ideal for studying PBL processes (e.g., Tanamachi et al. 2008, Loveless et al. 2019), as a data source for data assimilation experiments associated with severe weather (e.g., Degelia et al. 2020, Hu et al. 2019, Coniglio et al. 2019), and the temporal evolution of static stability (e.g., Feltz and Mecikalski 2002, Feltz et al. 2003, Wagner et al. 2008). The AERI is chosen because of its worldwide deployment in multiple climate regimes as part of the U.S. Department of Energy's Atmospheric Radiation Measurements (ARM) program (Mlawer and Turner 2016). Since ARM launches radiosondes at each of its sites between two and four times a day, we have a multi-year collected dataset consisting of radiosonde thermodynamic profiles and AERI radiance observations. These radiosonde profiles provide the thermodynamic profiles used for radiative transfer simulations for this synthetic study and will be described in the following chapter.

Previous information content analyses and retrievals utilized limited selections of the thousands of channels available on each of these instruments. We choose to consider all channels on all of these instruments in order to identify their full capabilities. Utilizing the full spectral coverage of these instruments would also allow thermodynamic retrievals to overcome poor estimates of trace gases.

Chapter 4: Radiosonde Data

The information content analyses presented in Chapters 5 and 6 utilize radiosonde profiles to provide thermodynamic information for radiative transfer modeling. Additionally, these radiosonde profiles provide observations for the calculation of the a priori covariance matrix \mathbf{S}_a (equation 2.8) as part of the optimal estimation retrieval (equation 2.15) and for calculations of the averaging kernel \mathbf{A} (equation 2.21). Given that one of the goals of this study is to better understand the effects of water vapor on information content, this study utilizes ARM observation sites in the East North Atlantic (ENA; Dong et al. 2014) on the Azores islands, North Slope of Atlantic (NSA; Verlinde et al. 2016) in Barrow/Utqiagvik, AK, and Southern Great Plains (SGP; Sisterson et al. 2016) in Lamont, OK. This provides the analysis with profiles from a marine subtropical environment, a polar environment, and a mid-latitude continental environment in order to assess the gains in information content of a synergy of ground-based and space-based instruments in varying climate regimes. While SGP and NSA have radiosonde archives that extend back more than 15 years, ENA only has radiosonde data available beginning in September 2013. In order to maintain uniformity, this study uses profiles from 1 October 2013 to 30 September 2019 for all three stations to make up our radiosonde profile database. With six years of observations available, this will provide a large range of environments to simulate for the information content experiment in Chapter 5 and for the calculation of the a priori covariance matrix \mathbf{S}_a throughout this dissertation.

The first analysis presented in Chapter 5 will utilize clear sky profiles. This is because radiative transfer calculations in cloudy sky scenes require several orders of magnitude more calculations than clear sky scenes and one of the goals of the information content analysis is to expand upon the work of Ebell et al. (2013) and include a large number of profiles. Three cloudy

sky profiles will be selected from SGP for analysis in Chapter 6. These cloud free profiles are also used in the calculation of S_a . Profiles are flagged as possibly containing clouds if any relative humidity measurement in the radiosonde profile is greater than 90%. We also require a radiosonde to reach 100 hPa to ensure that the entire troposphere has been observed. As summarized in Table 4.1, these quality control measures result in a dataset that consists of 464 clear sky profiles at ENA, 491 at NSA, and 3765 at SGP – which will be used for analysis in Chapter 5. SGP has many times more profiles that meet the clear sky requirements than ENA and NSA in because SGP has nearly double the total number of archived radiosondes (as SGP launches four radiosondes a day while the other sites only launch two) but also experiences fewer clouds and thus a lower percentage of profiles are flagged for being cloudy.

Station	SGP	ENA	NSA
<i>Total Radiosondes</i>	8536	4739	5037
<i>Removed for Quality Control</i>	42	18	15
<i>Removed for not Reaching 100 hPa</i>	112	36	25
<i>Total Cloudy Profiles</i>	4617	4221	4506
<i>Total Clear Sky Profiles</i>	3765	464	491

Table 4.1: Overview of radiosonde data considered for this study. Total radiosondes are the number of radiosondes in the ARM archive from 1 October 2013 to 30 September 2019.

Since the radiative contributions of the atmosphere above the typical heights that radiosondes reach are necessary for radiative transfer calculations, the radiosonde-observed profiles are augmented with the United States Air Force standard atmosphere geophysical model (McClatchey 1972) to provide a continuous profile up to the height that is designated as the top of the atmosphere in each experiment. The model atmosphere is blended with the radiosonde

observations such that the modeled lapse rates of the upper atmosphere are preserved while increasing or decreasing the temperature and water vapor mixing ratio to match the top measurement of the radiosonde.

Chapter 5: Clear Sky Information Content Analysis

5.1 Introduction

Ebell et al. (2013) presented the benefits of a synergy of a ground-based microwave radiometer with the space-based IASI in terms of the increase in DOF and reduction in uncertainties. They found that a synergy of the ground-based microwave radiometer with IASI resulted in greater information content and reduced uncertainties compared to the ground-based sensor alone. Notably, these improvements were seen in the near-surface layer, even where IASI provides very little information. The results of their study are promising for the prospects of a synergy of ground-based and space-based sensors offering a significant improvement in thermodynamic sounding of the troposphere, especially the PBL. However, their study utilized only 100 profiles from a single site in Germany. They also note that their results are highly dependent upon the atmospheric state, in particular water vapor. Turner and Löhnert (2014) also identified that AERI's information content is dependent on water vapor. Given the small sample size of the study presented by Ebell et al. (2013) and their focus on a single site, the variability of information content and uncertainties with the atmospheric state are not fully characterized by their study.

Additionally, while the 2017 Decadal Survey and NRC (2009) reports set goals for the vertical resolution of soundings, instrument studies have focused on information content, leaving the vertical resolutions of both single instrument and synergistic retrievals under-investigated. Given the results of Ebell et al. (2013) that the synergy increases DOF compared to a single sensor and the relationship between DOF and vertical resolution where both depend on the diagonal elements of the averaging kernel \mathbf{A} (shown in equations 3.22 and 3.23), it is reasonable to conclude

that the vertical resolution of a ground-and-space-based synergy will be improved compared to a single sensor alone. However, quantifying those improvements and comparing the vertical resolution of the synergy to the goals of the 2017 Decadal Survey are necessary for proving the benefits of the synergy.

The analysis presented in this section will build upon the clear sky information content study presented by Ebell et al. (2013). We will extend the analysis to include multiple climate regimes, utilizing radiosonde profiles from the ARM stations at ENA, NSA, and SGP, described in Chapter 4. This provides our analysis with profiles from a marine subtropical environment, a polar environment, and a mid-latitude continental environment in order to assess the gains in information content of a synergy of ground-based and space-based instruments in varying climate regimes. The analysis focuses on clear sky profiles because simulating clouds in the IR requires several orders of magnitude more calculations to account for the radiative effects of clouds, which would make an analysis like this on such a large set of atmospheric profiles impractical. The vertical resolution of single instrument retrievals from ground-based and space-based sensors will also be quantified in this analysis, as will the improvements in vertical resolution offered by a synergy of the two sets of sensors.

5.2 Radiative Transfer Modelling

The input profiles for this analysis are the 4,720 clear sky profiles from the three ARM stations, ENA, NSA, and SGP, summarized in Table 4.1. These radiosonde profiles (augmented with upper atmosphere information from the United States Air Force standard atmosphere geophysical model) are interpolated onto the 101-level AIRS pressure grid for radiative transfer modeling. The AIRS pressure grid is chosen due to its widespread use in the satellite-based

sounding community. To make it practical to compute radiative transfer calculations over such a large number of profiles for all of the channels on each instrument described in Table 3.1, this analysis uses an optical spectral sampling (OSS) fast radiative transfer model (Moncet et al. 2008 and Moncet et al. 2015). OSS is written by Atmospheric Environmental Research Inc. (AER) and produces radiances and temperature and trace gas Jacobians for a given atmospheric state. The model is a lookup table with coefficients specifically derived for each instrument, derived from the Line-By-Line Radiative Transfer Model (LBLRTM, Clough et al. 2005). Currently, OSS is designed to simulate the spectral characteristics of AERI, AIRS, CrIS, and IASI. Because of the continuous coverage and high spectral resolution of IASI, radiance and Jacobian simulations for IASI are used to calculate those measures for ABI and GIIRS (what we are designating as GIFTS) by using their spectral response functions to the IASI channels. Radiative transfer calculations for the geostationary sensors, ABI and GIFTS, simulates those instruments from the viewing angles of GOES-16 (longitude of 75.2° W) for SGP, and Meteosat-11 (longitude of 0° E) for ENA. The geostationary sensors are not simulated for NSA because of the oblique viewing angle for the polar regions from geostationary orbit. The polar-orbiting sensors (AIRS, CrIS, and IASI) are simulated at nadir.

Radiative transfer calculations using OSS accounts for absorption by water vapor and the trace gases of carbon dioxide, methane, ozone, and nitrous oxide. In order for the analysis to focus on the effects that changes in the thermodynamic profiles (specifically water vapor) have on information content, similar to the study done by Ebell et al. (2013), the same trace gas concentrations are used for every profile, regardless of the station. A representative trace gas profile is chosen from a NUCAPS (Gambacorta 2013) retrieval over SGP, since the majority of profiles are from the SGP site. The decision is made to focus the information content analysis on

parameters both instruments can retrieve. Therefore, emissivity and skin temperature are specified in the calculations and not included as part of the averaging kernel calculations for the satellite-based sensors. The NASA Combined Aster and MODIS Emissivity for Land (CAMEL, Borbas et al. 2018 and Loveless et al. 2021) monthly climatology of surface emissivity is used for each of the three stations to provide characteristic surface emissivity for the calculations.

5.3 Constructing the A Priori Covariance Matrix:

Calculations of the averaging kernel (recall equation 2.21) needed to compute DOF and vertical resolution require an a priori covariance matrix \mathbf{S}_a (equation 2.8). Given the large differences in surface pressure across the three stations in this analysis, the natural log of the ratio of the surface pressure to each pressure level is used as a vertical coordinate to ensure that the surface information from each profile is covaried together. \mathbf{S}_a is calculated as a pseudo-global a priori – including profiles from every station. This is done to ensure that \mathbf{S}_a is constant across the stations in order to highlight the relationship between information content and variations in water vapor. Thus, 50 profiles from each season at each station are randomly selected and those 600 radiosonde profiles are combined to form \mathbf{S}_a , which is displayed in Figure 5.1.

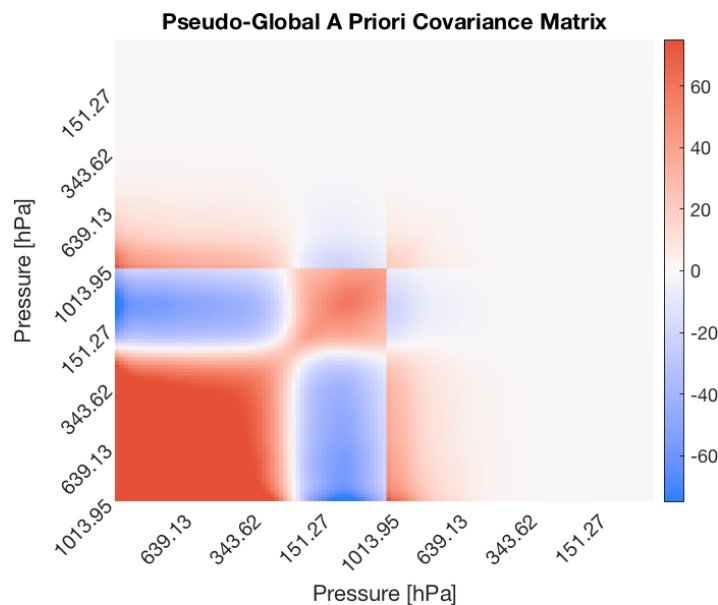


Figure 5.1: A priori covariance matrix used in this analysis. Bottom-left is temperature covaried against itself. Top-right is water vapor varied against itself. Top-left and bottom-right are temperature and water vapor covaried against each other.

5.4 Results

5.4.1 Degrees of Freedom

We begin by considering the results of the DOF (see equation 2.22) analysis for all 6 instruments described in Table 3.1. The DOF calculations across the full troposphere (which we denote as the surface to 200 hPa) are displayed in Figure 5.2. Both Ebell et al. (2013) and Blumberg et al. (2015) presented DOF calculations for AERI alone, finding roughly 5.5 DOF for temperature and roughly 3 DOF for water vapor across a similar layer, largely consistent with the full troposphere results we find for AERI. Ebell et al. (2013) finds about 4 DOF for both temperature and water vapor for IASI alone. Our methods produce about 5 DOF for temperature and 6 DOF for water vapor from IASI alone. This difference is likely attributable to the coarser grid of only 43 levels that Ebell et al. (2013) used compared to the AIRS 101 pressure levels used in this study, but channel selections, the a priori covariance matrix, and model differences may also contribute to the differences.

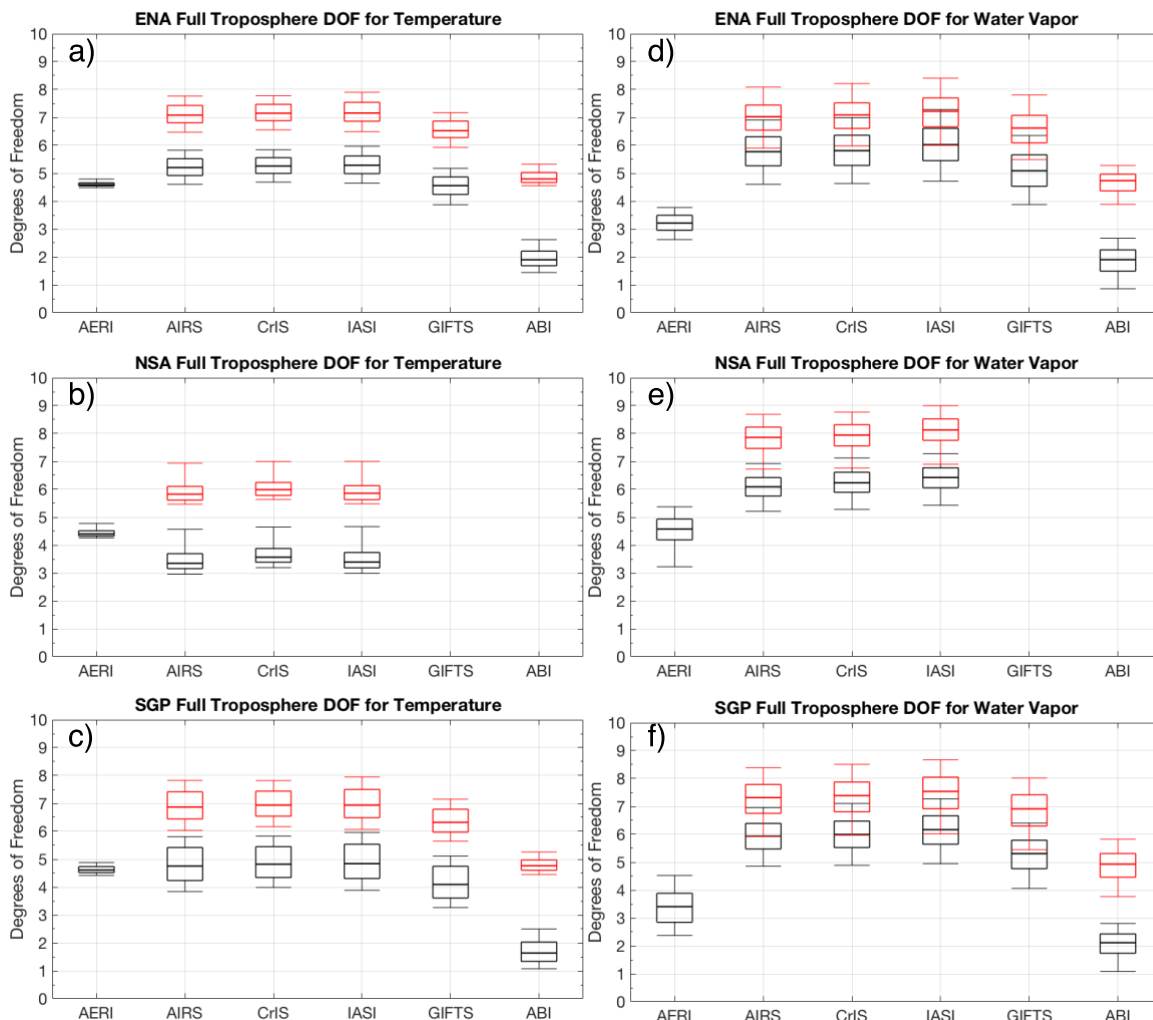


Figure 5.2: DOF for temperature (a-c) and water vapor (d-f) for the full troposphere (surface to 200 hPa). DOF for the individual sensors is displayed in black. DOF for the synergy of the AERI with each respective space-based sensor is displayed in red.

Assessing the results in Figure 5.2, AIRS, CrIS, and IASI (the three polar-orbiting hyperspectral sounders) all have very similar DOF to one another. While the results presented here for those three instruments are nadir only, we did not find significant changes in DOF with changes in scan angle (up to 35°) as we found that the Jacobians did not change much with scan angle. GIFTS has about 0.5 to 1 DOF less than the polar-orbiting sounders. We found that this is more of a result of the noise characteristics and the fewer total channels of the hypothetical GIFTS/GIIRS sensor compared to the AIRS, CrIS, or IASI than the sensor angle used to simulate

geostationary orbit. ABI has less than half of the information that the sounders offer, as would be expected given the few broadband channels that it has. The 2 DOF for temperature from ABI come from a combination of approximately 1 DOF near the surface from the window channels and 1 DOF in the free troposphere from the water vapor channels.

The combination of AERI with the space-based hyperspectral sounders (AIRS, CrIS, GIFTS, and IASI) results in a 30-40% increase in total DOF compared to the space-based sounder alone while the addition of AERI to the geostationary ABI results in more than doubling the information when compared to the ABI alone. The variations in DOF across the three sites are relatively small. Information content for AIRS, CrIS, and IASI at NSA is about 1 DOF lower for temperature, compared to SGP and ENA, and 1 DOF higher for water vapor. For the upward-facing AERI, profiles at NSA and SGP result in largely similar DOF for temperature, while the DOF for temperature at ENA is only marginally less. AERI gets about 4 to 5 DOF for water vapor at NSA, but only about 3 to 3.5 DOF at ENA and SGP. The synergy combinations largely follow the patterns of the space-based sensors, resulting in greater temperature information at ENA and greater water vapor information at NSA.

Figure 5.3 focuses on the PBL and lower free troposphere by displaying DOF calculations for the surface to 700 hPa layer. ABI only offers 1 DOF for temperature, while the space-based hyperspectral sounders produce about 1.5 to 2.5 DOF (more at ENA, less at NSA) for temperature in the PBL. The space-based hyperspectral sounders have about 1.5 to 2 DOF for water vapor while ABI has less than 0.5 DOF in the PBL. The benefits of ground-based remote sensing in the PBL are clear as AERI by itself produces about 1.5 times greater DOF for temperature in the surface to 700 hPa layer than any of the space-based hyperspectral sounders. However, the synergy of AERI with the space-based hyperspectral sounders promises even greater benefits, with results

indicating a doubling of DOF for temperature, and an increase of about 40-50% for DOF for water vapor as compared to the space-based hyperspectral sounders alone. The synergy of AERI with the space-based hyperspectral sounders produces greater DOF than AERI alone in the surface to 700 hPa layer. AERI paired with a space-based hyperspectral sounder would result in about 4 to 4.5 DOF for temperature and 3 to 4 DOF for water vapor. This would present a significant improvement in PBL sounding, compared to what is currently provided with space-based hyperspectral sounders alone. The increased DOF enables the retrieval of greater detail in the structure of variations in low-level temperature and water vapor, thus producing more finely resolved inversion and moist layers. Similar to the patterns identified in the full troposphere view in Figure 5.2, the space-based hyperspectral sounders provide marginally greater temperature DOF from the surface up to 700 hPa at ENA, with greatest water vapor DOF at NSA. AERI provides similar temperature information across the three sites, but greater water vapor information at NSA than at ENA or SGP. The variation of the synergies once again more closely follows the variation of the space-based sensors more than that of the AERI.

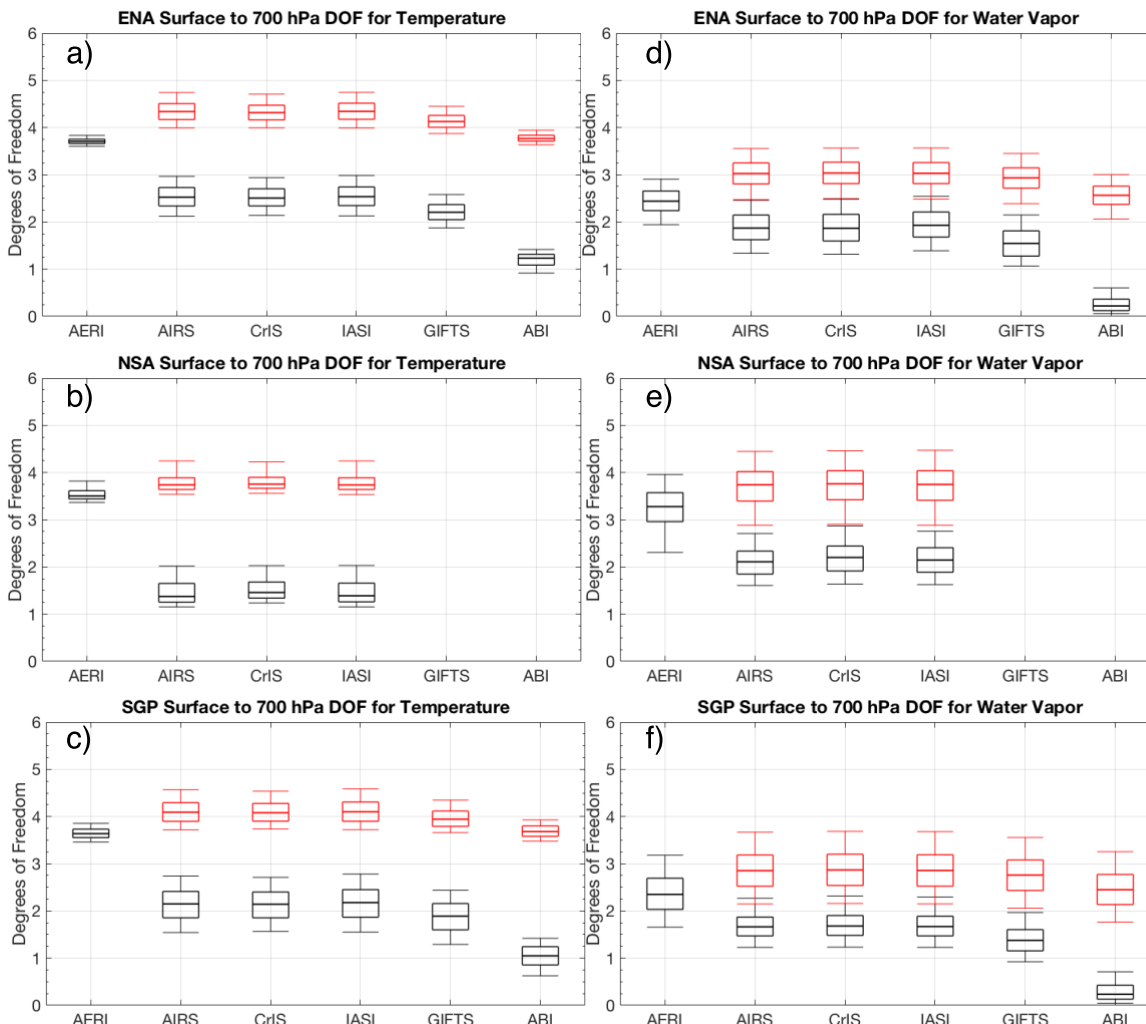


Figure 5.3: Same as in Figure 5.2 but for the surface to 700 hPa layer.

5.4.2 Variations in Information with Precipitable Water Vapor

While comparing DOF across the different sites may allow for broad generalizations (as ENA usually has greater atmospheric moisture content than NSA, for example), the profiles compiled for each site exhibit significant variability throughout the duration of the analyzed period so that some profiles at SGP may have greater moisture than profiles at ENA. To gain a better understanding of the effects of moisture on information content for each of these sensors, we compute the precipitable water vapor (PWV) of each profile using the SHARPPy program (Blumberg et al. 2017). Given how similar AIRS, CrIS, GIFTS, and IASI are in the DOF

calculations, we focus the remainder of the results section on CrIS since it is the most recent sounder put into operation by NOAA, while keeping in mind that we expect these results to be consistent with AIRS, GIFTS, and IASI. Given the relative lack of sounding information that ABI provides, we omit it from the remainder of the discussion.

To assess how DOF varies with PWV, we bin profiles for every 1 cm of PWV and compute the range of DOF for those profiles. While every PWV bin less than 4 cm contains greater than 650 profiles, the 4+ cm bin only contains 128 profiles. This 4+ cm bin still should be a large enough sample size to draw conclusions from, given that Ebell et al. (2013) had a sample of only 100 profiles.

Figure 5.4a displays AERI's DOF for temperature demonstrating that there is little variation in DOF with PWV at either the full troposphere view (surface to 200 hPa), or in the near-surface layer (surface to 700 hPa). Since DOF is an integrated quantity, it is difficult to discern the heights at which the variations may be found. In order to determine if PWV variations cause changes in what height levels the information is, we create composite mean averaging kernels from the profiles with 4+ cm of PWV (high PWV composite), with 2 – 3 cm (medium composite), and with less than 1 cm (low composite). Since DOF is the trace of the averaging kernel (equation 2.22), we can assess the changes in information at different heights by plotting the diagonal elements of the three sets of composite averaging kernels; this analysis for temperature with AERI is shown in Figure 5.4b. Just as there was no variation in DOF with varying PWV, there is no difference in information at different height levels with the varying precipitable water composites. This suggests that greater water vapor does not result in greater attenuation of the temperature signal aloft, compared to dry environments. Figures 5.5a, 5.5b, and 5.5c display the temperature Jacobians for AERI in the high, medium, and low PWV composites, respectively. Comparing the

three figures, only the shortwave channels at 1200 cm^{-1} and greater change with changing PWV. The signal from the CO_2 band, around 650 cm^{-1} , remains the same in each composite, resulting in the pattern seen in Figures 5.4a and 5.4b.

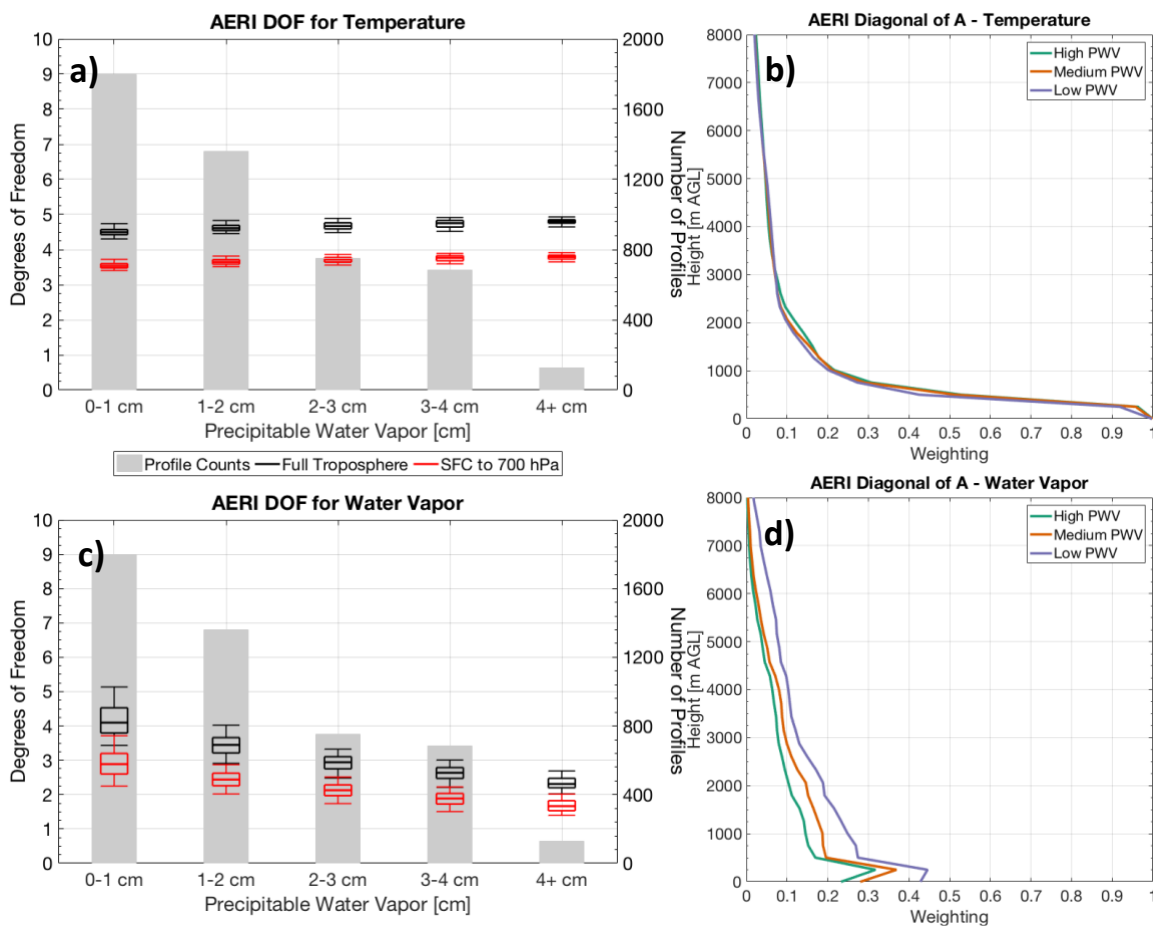


Figure 5.4: AERI DOF for temperature (a) and water vapor (c) binned for every 1 cm of PWV. Number of profiles in each PWV bin is displayed as the gray bars, DOF for the full troposphere (surface to 200 hPa) is displayed in black, and the DOF for the surface to 700 hPa is displayed in red. The diagonal of high (4+ cm, green), medium (2-3 cm, orange), and low (less than 1 cm, purple) PWV composite mean averaging kernels for AERI for temperature and water vapor are shown in b and d respectively.

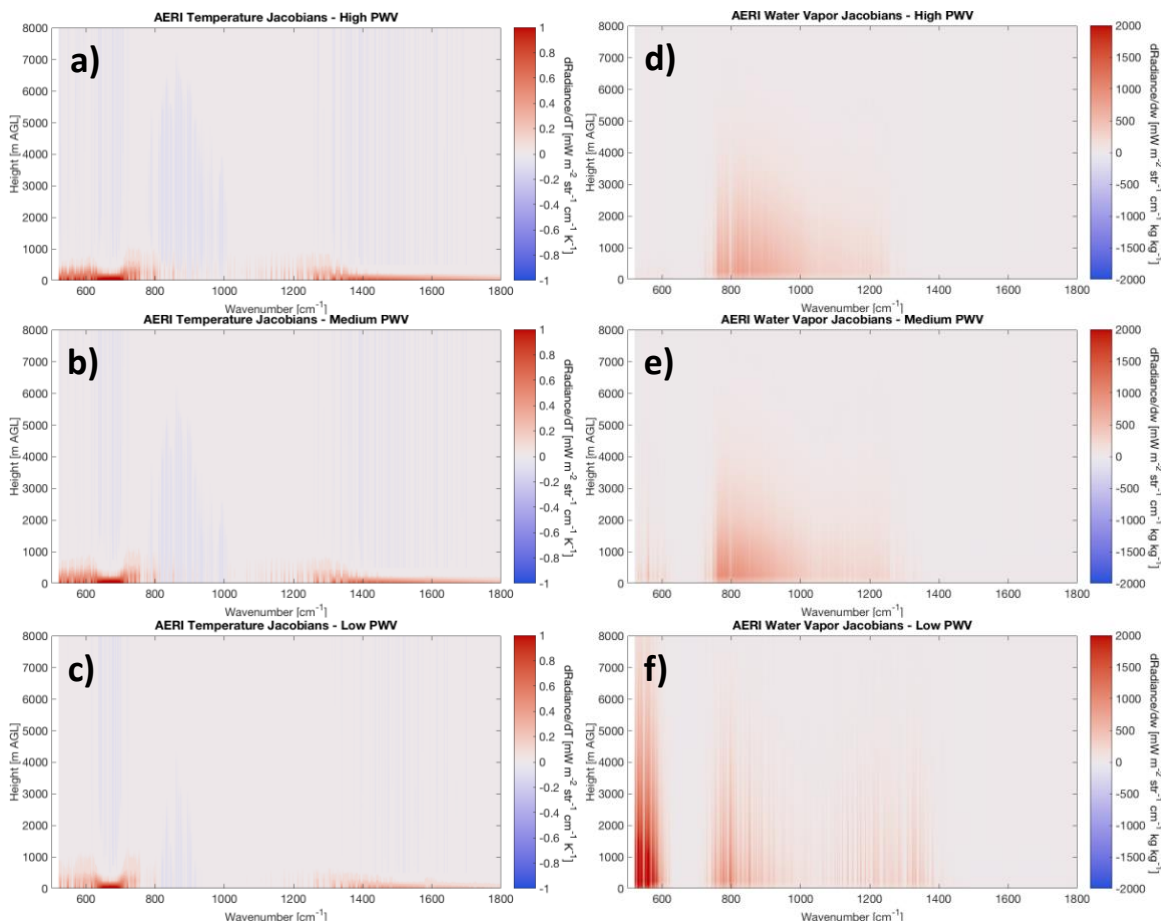


Figure 5.5: Composite temperature (a – c) and water vapor (d – f) Jacobians for AERI in the high (4+ cm, a and d), medium (2 – 3 cm, b and e), and low (less than 1 cm, c and f) PWV composites.

However, AERI’s DOF for water vapor is susceptible to changes in the PWV content of the environment, as shown in Figure 5.4c. AERI has greatest water vapor DOF in dry environments, and a minimum in DOF in very moist environments; this is in agreement with Turner and Löhnert (2014). On average, there is approximately a 1.5 DOF difference between the 0 – 1 cm bin and the 4+ cm bin for the surface to 200 hPa layer, and a difference of about one DOF for the surface to 700 hPa layer. Figure 5.4d reflects this pattern as the low PWV composite has the greatest information throughout the profile compared to the high and medium composites. The water vapor Jacobians for AERI for each of the three precipitable water composites are shown in Figures 5.5d, 5.5e, and 5.5f. Comparing Figures 5.5d and 5.5e, it is seen that the high and medium

precipitable water composites have very similar water vapor Jacobians, which matches the relative similarity seen in Figure 5.4c. However, the water vapor Jacobians for the low precipitable water composite in Figure 5.5f has weaker sensitivity to water vapor in the window channels from 800 to 1000 cm^{-1} compared to the high and medium composites, but much stronger signal in the far IR from 520 to 600 cm^{-1} . Thus, it is the far IR channels provided by the AERI, that result in the greater water vapor information throughout the profile in very dry environments (which tend to also be cold) that was seen in Figure 4.3d. The advantages of water vapor sounding in cold and dry environments using the far IR have also been documented by Bianchini et al. (2011).

Unlike AERI, the DOF for temperature from CrIS does vary with PWV, as is shown in Figure 5.6a. Across the surface to 200 hPa layer, CrIS has the least DOF in dry environments and maximizes DOF in the 3 – 4 cm and 4+ cm bins. The difference between the 0 – 1 cm bin and the 4+ cm bin is approximately 1.75 DOF on average. CrIS temperature DOF for the surface to 700 hPa layer, like the surface to 200 hPa layer, is also at a minimum in the driest environments. However, DOF for the surface to 700 hPa layer increases from about 1.5 in the 0 – 1 cm bin to 2.5 in the 2 – 3 cm PWV, bin but remains around 2.5 for the 3 – 4 cm and 4+ cm bins as well. Figure 5.6b reveals more detail on this difference between the surface to 200 hPa layer compared to the surface to 700 hPa layer DOF for temperature. The medium and high PWV composites have nearly the exact same information below 2500 m above ground level (AGL), reflective of the lack of variation in CrIS temperature DOF in the surface to 700 hPa layer between 2 cm and 4+ cm PWV. The difference between the medium and high composites is above 2500 m AGL, where the high composite has greater information than the medium composite, resulting in the DOF pattern in the surface to 200 hPa layer. The low PWV composite has the least information throughout the profile. Figures 5.7a, 5.7b, and 5.7c display composite temperature Jacobians for CrIS, which reveals that

only the water vapor channels in the midwave band are changing across the different composites. Note that this indicates that if a retrieval's channel selection does not include midwave bands for retrieving temperature, then its DOF will not be sensitive to variations in PWV. Synthesizing these pieces together, higher concentrations of water vapor generally result in increased temperature information for CrIS. However, beyond very dry environments, greater PWV will not result in greater information in the PBL.

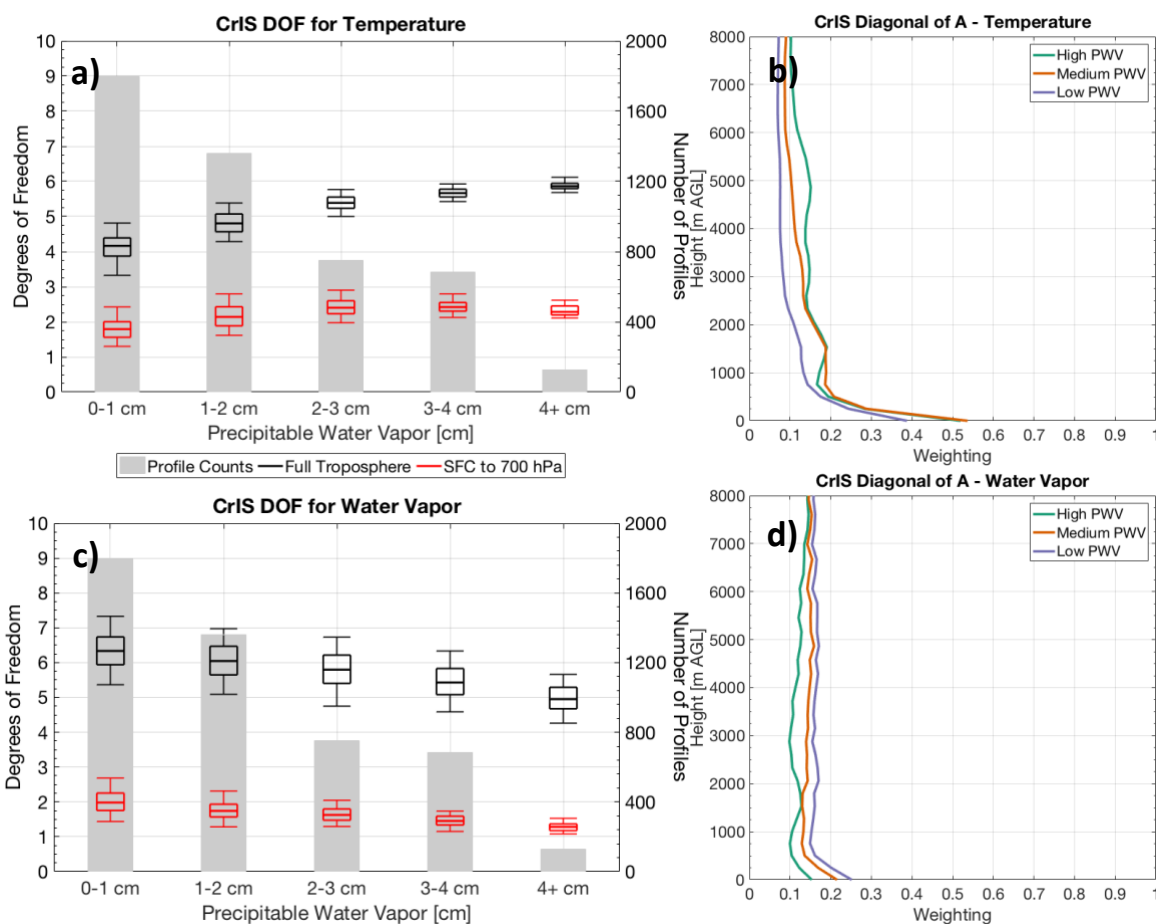


Figure 5.6: Same as in Figure 5.4 but for CrIS.

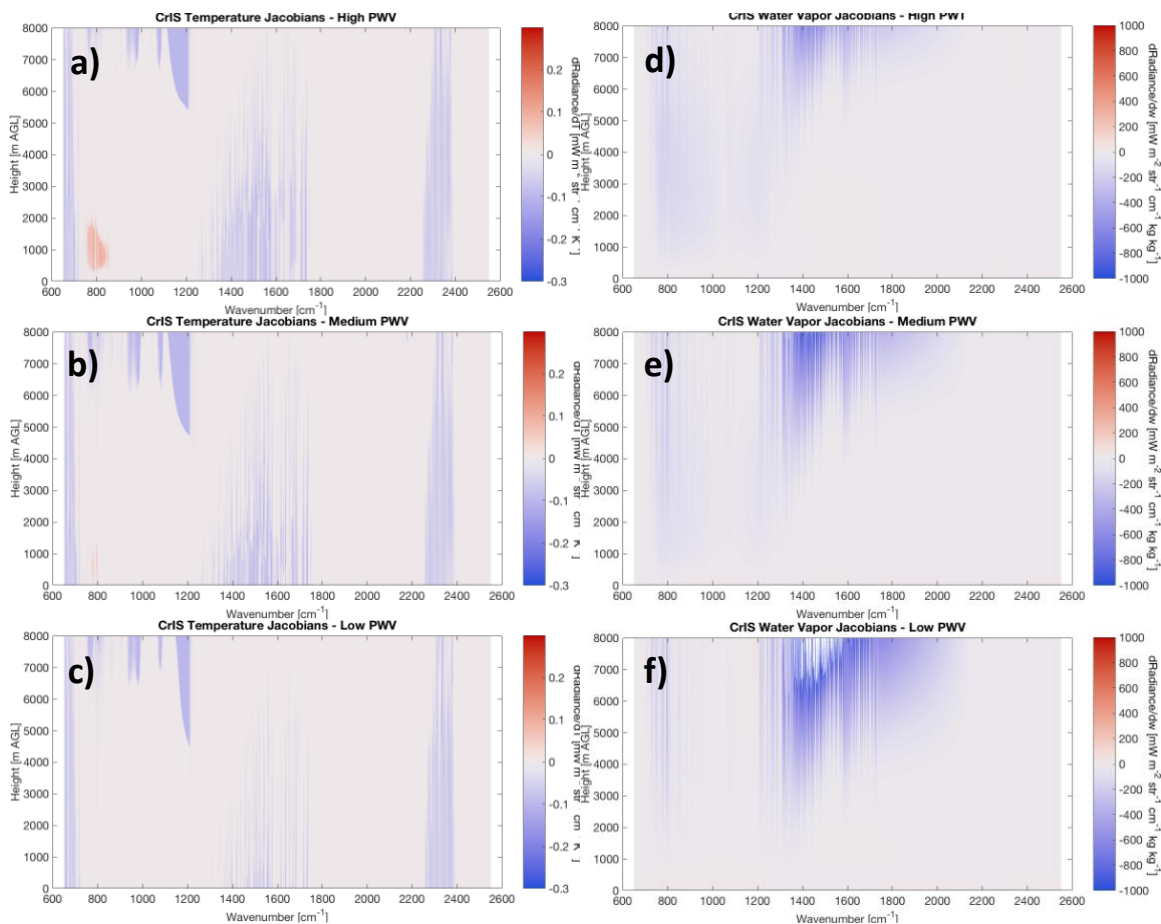


Figure 5.7: Same as in Figure 5.5 but for CrIS.

Figure 5.6c displays CrIS DOF for water vapor with varying PWV. In general, across the surface to 200 hPa layer, CrIS has greater DOF for water vapor in dry environments than in moist environments, opposite the pattern seen for temperature with CrIS. The median water vapor DOF in the 0 – 1 cm bin is about 1.5 greater than the median DOF in the 4+ cm bin. The variation in DOF across the surface to 700 hPa layer is similar to the surface to 200 hPa layer, with the greatest information in dry environments and the 4+ cm bin having about 0.5 DOF less than the 0 – 1 cm bin. Figure 5.6d reveals that the dry environments result in greater water vapor information throughout the profile, while the very moist environments result in the least water vapor information throughout the profile. Figures 5.7d, 5.7e, and 5.7f show that the water vapor

Jacobians in the midwave band from 1210 cm^{-1} to 1750 cm^{-1} are strongest in the low PWV composite, resulting in the patterns seen in Figure 5d.

Figure 5.8 displays the variations in DOF and information with PWV for the synergy of CrIS and AERI (referred to as CrIS+AERI for the rest of this paper). As will be displayed in the vertical resolution and uncertainties sections, signal from CrIS informs the synergy aloft, while AERI informs the synergy very close to the surface. Figure 5.8a reveals that the surface to 200 hPa DOF for temperature from CrIS+AERI varies primarily like temperature DOF for CrIS alone across the surface to 200 hPa layer with about 1.5 DOF less in the 0 – 1 cm bin than in the 4+cm bin. There is small variation across the PWV bins in the surface to 700 hPa layer. The diagonal elements of **A** in the three composites in Figure 5.8b gives a sense of how AERI and CrIS are blended in the synergy. Below 500 m AGL, the information of the composites is all the same, similar to what was seen for AERI in Figure 5.8b. Increasing in height from 1000 m AGL to 3000 m AGL the pattern of information transitions to reflect CrIS alone more than the AERI alone, and thus the low PWV composite has less information than the high and medium composites. Above 4000 m AGL, CrIS+AERI mirror the pattern seen for CrIS alone in Figure 5.6b.

As shown in Figure 5.8c, the DOF for CrIS+AERI for water vapor across the surface to 200 hPa layer has a maximum in the 0 – 1 cm bin and decreases with increasing moisture to have a minimum in the 4+ cm bin. The difference in DOF between the 0 – 1 cm bin and the 4+ cm bin is about two. The same pattern as was described for the DOF in the surface to 200 hPa layer is present in the surface to 700 hPa layer, with a difference of about one DOF between the maximum in the 0 – 1 cm bin and the 4+ cm bin. This is approximately the same difference that was seen between the same bins in Figure 5.4c for AERI water vapor DOF. Figure 5.8d shows how the AERI's sensitivity to water vapor in cold and dry environments from its far IR channels dominates

the pattern in information near the surface, driving the variations seen in the DOF for the surface to 700 hPa. This increased water vapor information from AERI's far IR channels causes the increased difference in DOF across the surface to 200 hPa layer between the 0 – 1 cm bin and the 4+ cm bin compared to the pattern seen for CrIS alone.

We will conclude this section noting that despite these variations in DOF across the two layers we have considered, CrIS+AERI offers greater DOF in every PWV bin than AERI or CrIS alone. This indicates that the synergy would be expected to provide an improvement in thermodynamic sounding accuracy in all ranges of environments.

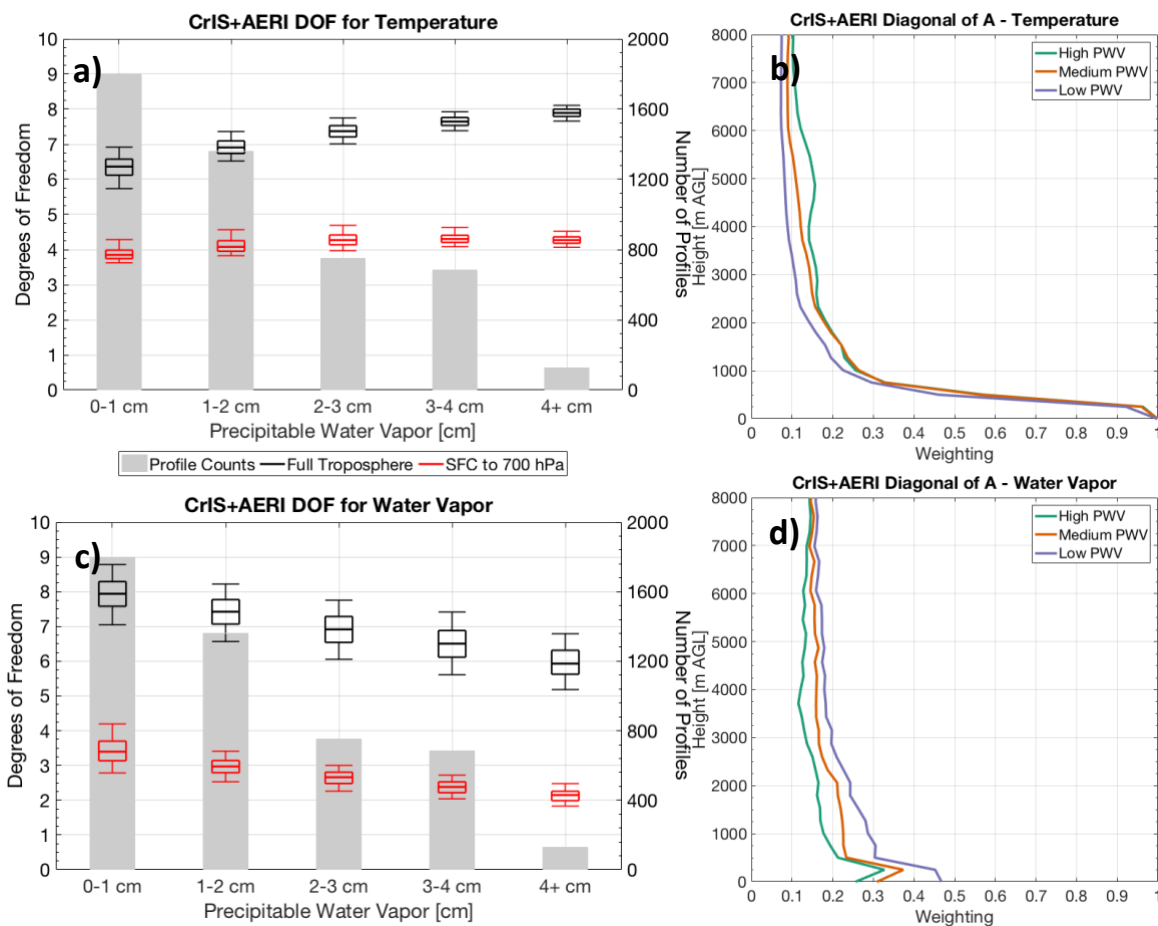


Figure 5.8: Same as in Figure 5.4 but for CrIS+AERI.

5.4.3 Vertical Resolution

As noted in equation 2.23 (from Hewison 2007), the averaging kernel allows for calculation the vertical resolution of a retrieval by spreading the diagonal elements of the averaging kernel (the same elements used to calculate DOF) across the vertical grid used for calculations. The vertical resolution of a retrieval is analogous to the thickness of the layer over which the signal is coming from when the retrieval makes an estimate at a particular level. Vertical resolution for AERI, CrIS, and CrIS+AERI is shown in Figure 5.9. The shadings for each sensor are between the 25th and 75th percentiles of all 4,720 profiles included in this analysis. As noted earlier, the vertical resolution of a retrieval is dependent on the grid used in calculations. Since we use the AIRS 101 pressure levels, this coarser grid under-estimates the vertical resolution that AERI is capable of near the surface. This can be seen when comparing our calculations for AERI's temperature resolution over the lowest 200 m of the atmosphere with those presented by Turner and Löhnert (2014) and Blumberg et al. (2015), who did their vertical resolution calculations on a grid designed for the AERI. As seen in Figure 5.9a, the vertical resolution of the AERI below 200 m AGL is never better than about 250 m, which is the resolution of the grid near the surface. [Note that Turner and Löhnert (2014) and Blumberg et al. (2015) demonstrated that the AERI's vertical resolution for temperature at any height below 1 km is approximately that height; i.e., at 50 m AGL the vertical resolution is 50 m, whereas at 500 m AGL the vertical resolution is 500 m]. Above 250 m AGL, the vertical resolution for temperature for the AERI largely increases linearly with height such that it has a resolution of about 1000 m at 1000 m AGL, and 2000 m at 2000 m AGL. AERI and CrIS are comparable in vertical resolution between 1000 m and 2000 m AGL, with a resolution of about 1500 m. The vertical resolution of CrIS for temperature is about 2500 – 3500 m through most of the free troposphere, gradually getting larger with height. CrIS+AERI

provides the greatest improvements, compared to CrIS alone, in the bottom 1000 m. The synergy of CrIS+AERI results in an improvement of about 400 m in vertical resolution compared to CrIS alone in the bottom 1000 m. The synergy of the two instruments is better than that of the individual instruments between about 500 m AGL and 5000 m AGL, though marginal improvements are seen all the way up to 8000 m AGL.

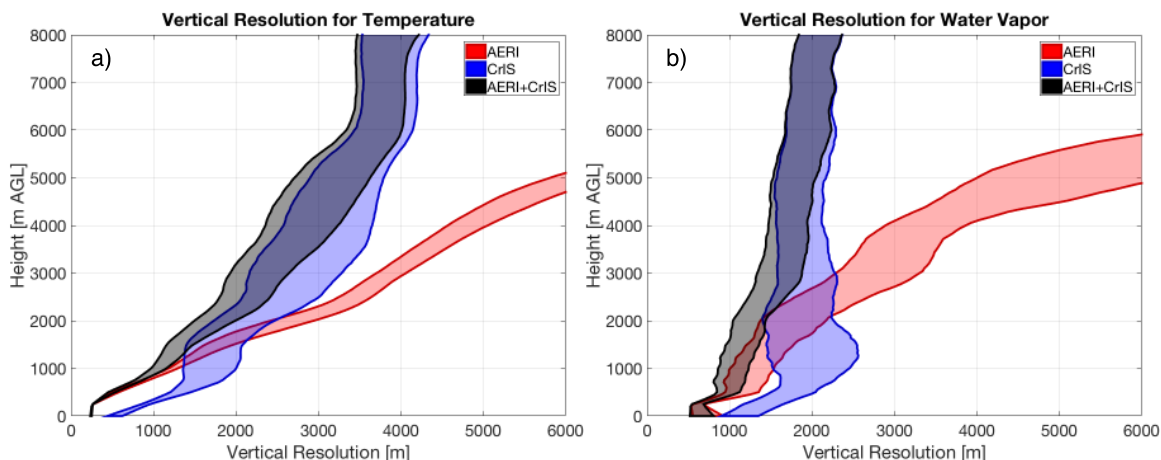


Figure 5.9: Vertical resolution for AERI (red), CrIS (blue), and the synergy of CrIS+AERI (gray) for temperature (a) and water vapor (b). Shading is between the 25th and 75th percentiles for all 4,720 profiles in the analysis.

Vertical resolution for water vapor sounding is displayed in Figure 5.9b. AERI's vertical resolution for water vapor (Figure 5.9b) is about 800 m at the surface and increases with height. [Again, the vertical grid chosen does matter, as the vertical resolution of the water vapor profiles from Turner and Löhnert (2014) is about 200 m at the surface and rapidly decreases to 700 m at approximately 300 m AGL, which is in rough agreement with this work]. The vertical resolution of the water vapor profiles from the AERI and CrIS are comparable in the 1000 m to 3000 m AGL range, with AERI having better resolution below, and CrIS being better aloft. Overall, vertical resolution of water vapor for CrIS is better than 2500 m throughout the lowest 8000 m of the troposphere. CrIS+AERI provides an improvement of about 400 m in resolution over the bottom

2000 m of the troposphere. Similar to what was shown in Figure 5.9a for temperature, CrIS+AERI is better than either instrument individually from about 500 m up to 4000 m AGL.

The 2017 Decadal Survey set a goal of 1000 m resolution soundings, which is exceeded in the bottom 1000 m AGL for both temperature and water vapor by CrIS+AERI. Neither temperature nor water vapor sounding above 1000 m for CrIS+AERI meets the 1000 m resolution goal. However, the improvements in vertical resolution made by CrIS+AERI near the surface improves the retrieval in the PBL where sharp gradients in temperature and water vapor are present. These improvements will aid in detecting the strength and vertical location of the capping inversion and detecting low-level variations in water vapor – two important features that would improve monitoring of both the timing and severity of severe convection.

Figure 5.10 displays the composite vertical resolution profiles for AERI, CrIS, and CrIS+AERI in the high, medium, and low PWV composites. Given the relationship that the averaging kernel has with the calculation of DOF and vertical resolution (again, recall equations 2.22 and 2.23), it is expected that the patterns displayed in Figure 5.10 are similar to what was discussed in the previous section.

AERI's vertical resolution for temperature, shown in Figure 5.10a, is not affected by variations in precipitable water below 3000 m AGL. Above 3000 m AGL, the vertical resolution in the low PWV composite becomes worse than the medium and high composites, but the AERI's information content above 3000 m AGL is limited anyway, and thus the AERI-retrieved profiles are typically not used above that level (e.g., Hu et al. 2019; Coniglio et al. 2019, Degelia et al. 2020). The vertical resolution of water vapor for AERI is shown in Figure 5.10d. As was shown previously, the sensitivity of the AERI's far IR bands improves water vapor sounding in cold and dry environments, resulting in improved vertical resolution in the low PWV composite.

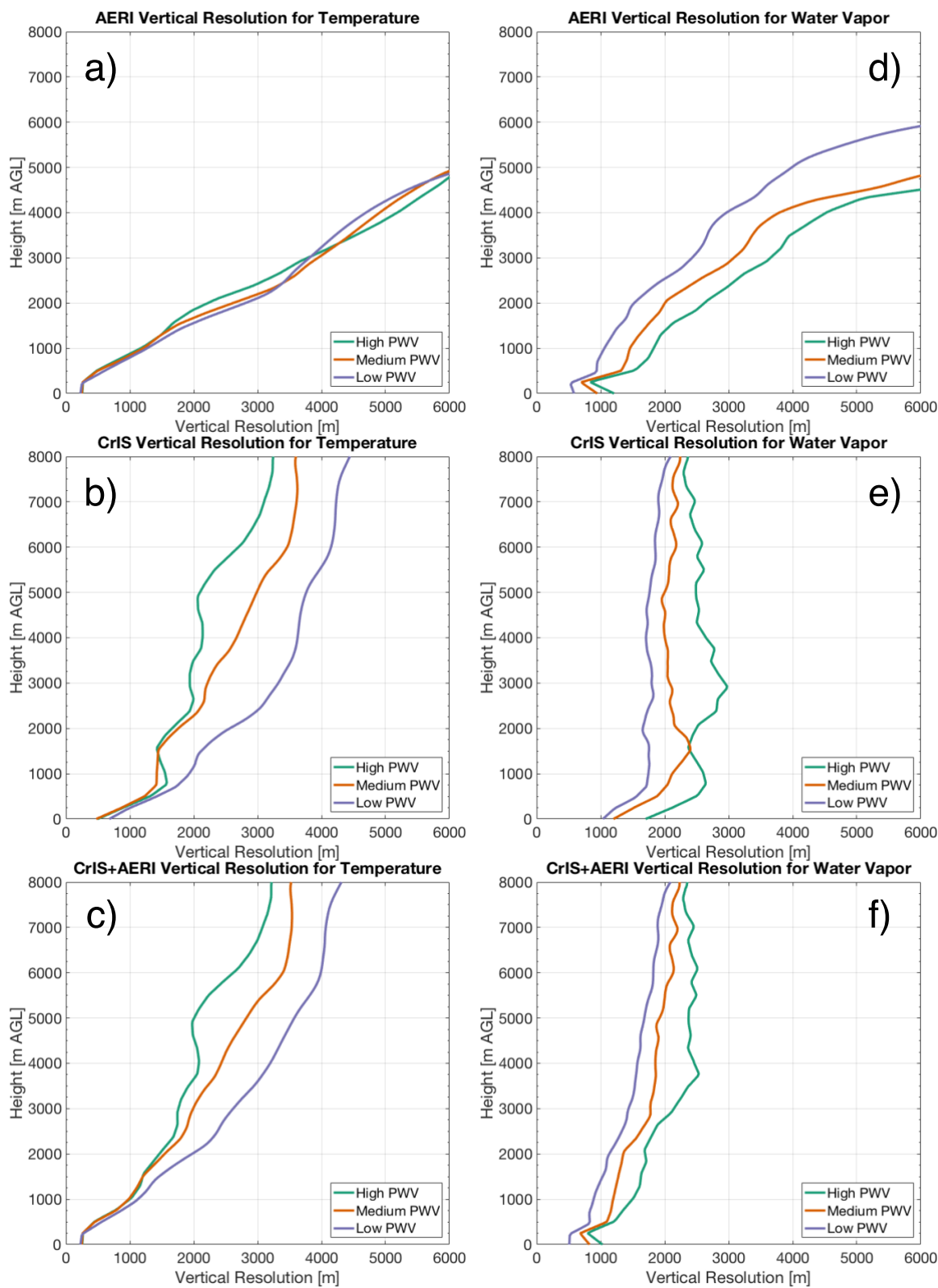


Figure 5.10: Vertical resolution for temperature (a-c) and water vapor (d-f) for AERI (a and d), CrIS (b and e), and CrIS+AERI (c and f) in high (4+ cm, green), medium (2-3 cm, orange), and low (less than 1 cm, purple) PWV composites.

Vertical resolution of temperature for CrIS is shown in Figure 5.10b. The PWV composites result in similar vertical resolution for temperature below 500 m AGL, but the vertical resolution of the low PWV composite is about 100 m worse than the high and medium composites. Above 500 m AGL, the low PWV composite is about 1000 m worse than the medium composite. The high and medium composites are similar from the surface up to 2000 m AGL. The high PWV composite results in the best vertical resolution above 2000 m AGL. The variations in vertical resolution across the three PWV composites shown here range from about 500 m at 1000 m AGL to almost 2000 m at 5000 m AGL. This suggests that temperature soundings from CrIS would have notably better vertical resolution in moist environments than in dry environments. However as was shown in the previous section, this effect would only be seen if the CrIS midwave bands (which are sensitive to water vapor) are included in a given temperature retrieval. A method retrieving temperature separately from water vapor (as suggested by Smith et al. 2021) would not see this effect. In contrast to our results for temperature, dry environments result in the best vertical resolution for water vapor sounding from CrIS, as seen in Figure 5.10e. The high PWV composite results in the worst vertical resolution for water vapor throughout the profile. The difference between the high and the low PWV composites is about 500 - 1000 m throughout the profile.

The vertical resolution composites for CrIS+AERI in Figures 5.10c and 5.10f result in a blend of the results of the composites for AERI alone and CrIS alone. For temperature, there is no variation in the vertical resolution of temperature soundings by CrIS+AERI below 800 m AGL. Above 2000 m AGL, CrIS+AERI behaves like CrIS alone for temperature, with better resolution in the high and medium PWV composites than in the low PWV composite. Both AERI and CrIS have better vertical resolution for water vapor sounding in the low PWV composite than in the high and medium PWV composites, which results in CrIS+AERI also having better vertical

resolution of water vapor in the low PWV composite throughout the profile as well. In general, CrIS+AERI presents an improvement to vertical resolution of sounding both temperature and water vapor in all environments.

5.4.4 Uncertainties

The 1σ uncertainties are calculated by taking the square root of the elements of the diagonal of the posterior error covariance matrix (described in equation 2.20). Figure 5.11 displays the 1σ uncertainties for AERI, CrIS, and CrIS+AERI. The temperature uncertainties of the AERI increase with height while the uncertainties for CrIS are greatest near the surface, as is expected for the upward and downward pointing instruments respectively. Both AERI and CrIS have a maximum in water vapor mixing ratio uncertainty at about 1000 m AGL, roughly corresponding to the mean inversion height in the radiosonde dataset used in this study. If skin temperature Jacobians for an unknown skin temperature were to be included in the calculation of the averaging kernel, the near-surface uncertainties for CrIS would increase. Future work is needed to better understand the effects of skin temperature and surface emissivity on these uncertainties. Combining the temperature and water vapor mixing ratio uncertainties we consider the relative humidity uncertainties of each instrument in Figure 5.11c. The relative humidity uncertainty has a maximum for CrIS at the inversion height, where its water vapor mixing ratio and temperature uncertainties were greatest as well. AERI's relative humidity uncertainty generally increases with height.

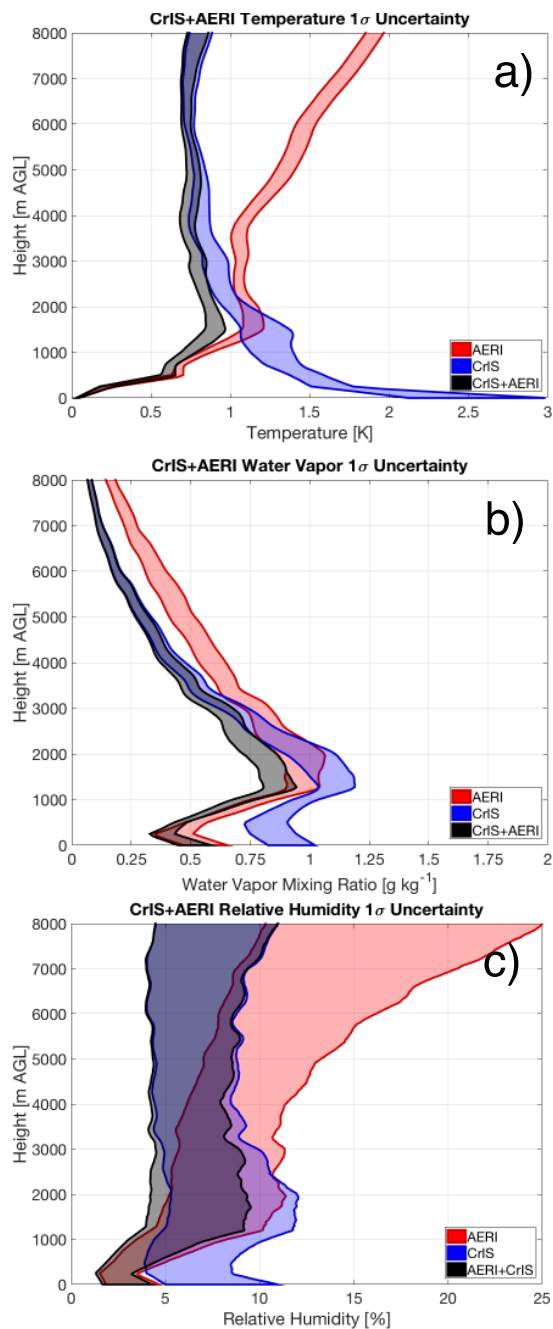


Figure 5.11: 1 σ uncertainties for AERI (red), CrIS (blue), and CrIS+AERI (gray) for temperature (a), water vapor mixing ratio (b), and relative humidity (c). Shading is between the 25th and 75th percentiles for all 4,720 profiles in the analysis. For reference, the 1 σ uncertainties of the a priori are about 14 K and 4 g kg⁻¹ at the surface.

The temperature and water vapor uncertainties for AERI very closely resemble the uncertainty profile displayed by Blumberg et al. (2015) and Turner and Löhnert (2014). Klein et al. (2015) also found very good agreement between the near-surface temperature in AERI

retrievals and collocated in-situ observations. While a different type of analysis, the radiosonde validation of NUCAPS presented in Sun et al. (2017) does not identify the local maximum in uncertainty at the top of the inversion around 1000 m AGL that we identify here. This could be a product of the majority of profiles in this analysis coming from SGP. Also note that Sun et al. (2017) has differences between radiosonde and NUCAPS retrievals about 40% greater for temperature for CrIS than this study, as expected given the noise assumptions.

CrIS+AERI results in a decrease of 0.5 – 1.5 K or about a 50% reduction in uncertainties in the lowest 1000 m AGL, compared to CrIS alone. Similarly, CrIS+AERI results in a decrease of about 50% in the water vapor mixing ratio uncertainties and reduces the relative humidity uncertainties by half in the lowest 1000 m AGL. While the greatest improvements are in the lowest 1000 m, improvements of CrIS+AERI compared to CrIS alone occurs up to 4000 m AGL. Similar to what was seen with vertical resolution, between 500 m and 4000 m AGL CrIS+AERI is better than either AERI or CrIS alone – once again emphasizing the benefits of a combined retrieval.

Given that these instruments have far less information than the number of layers used in the radiative transfer calculations, the information gained at each level is spread over multiple levels. Similarly, uncertainties associated with one layer result in uncertainties in other layers as well. As has been shown in Turner and Blumberg (2019), the posterior correlation matrix offers a useful view to understand the improvements of an instrument synergy by looking at the cross-layer correlations in uncertainties. The posterior correlation matrices for AERI, CrIS, and CrIS+AERI are shown in Figure 5.12. CrIS+AERI reduces the cross-layer sources of uncertainties compared to each instrument alone in the lowest 1000 m AGL, the same region that CrIS+AERI was shown to have the greatest improvements in vertical resolution and uncertainties. The improvement that the synergy offers in the lowest 1000 m compared to CrIS alone presents the case for why this

ground-based/space-based synergy should be considered as a solution to the difficult problem of PBL sounding.

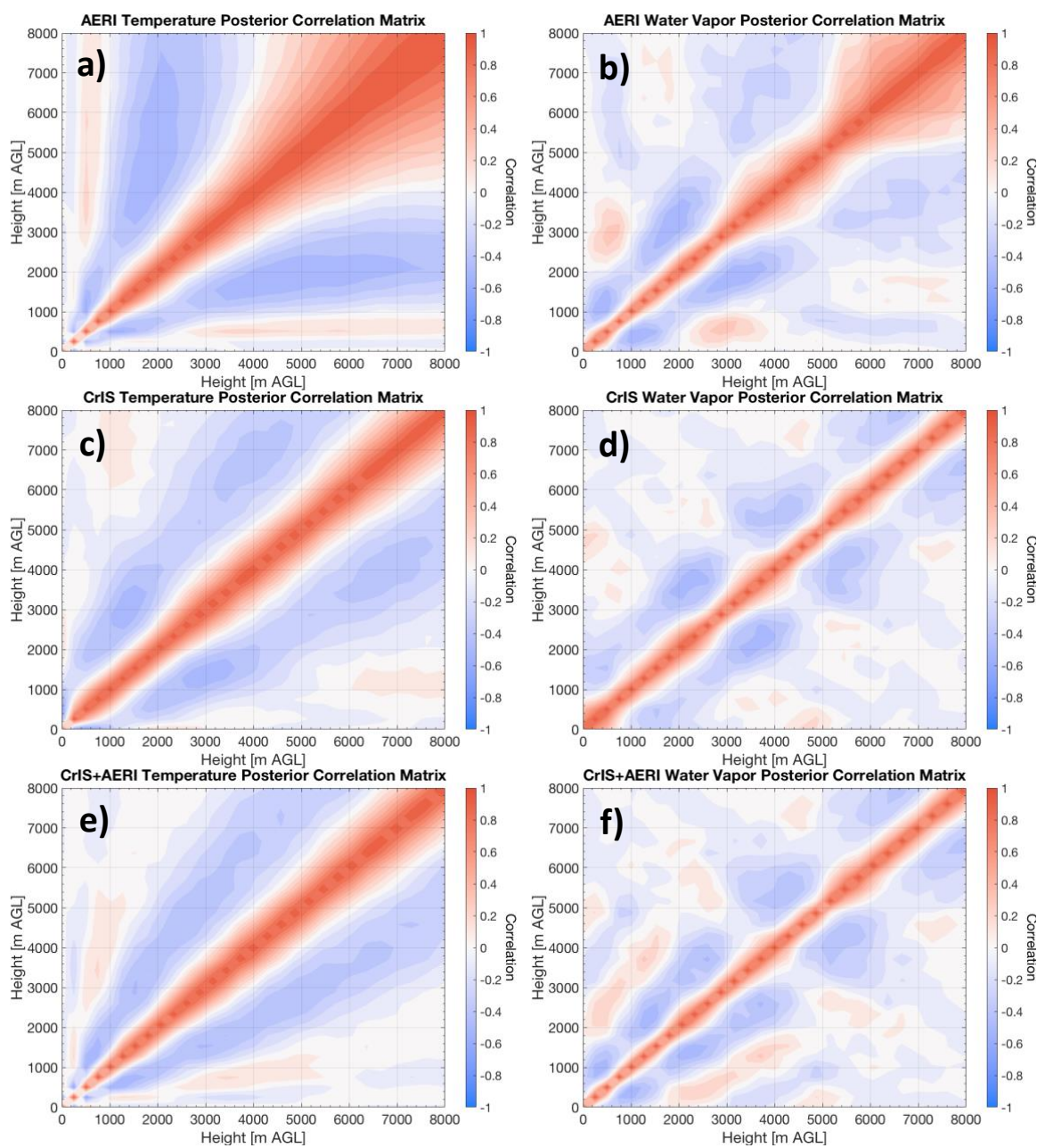


Figure 5.12: Posterior correlation matrix for temperature (a-c) and water vapor (d-f) for AERI (a and d), CrIS (b and e), and the synergy of CrIS+AERI (c and f).

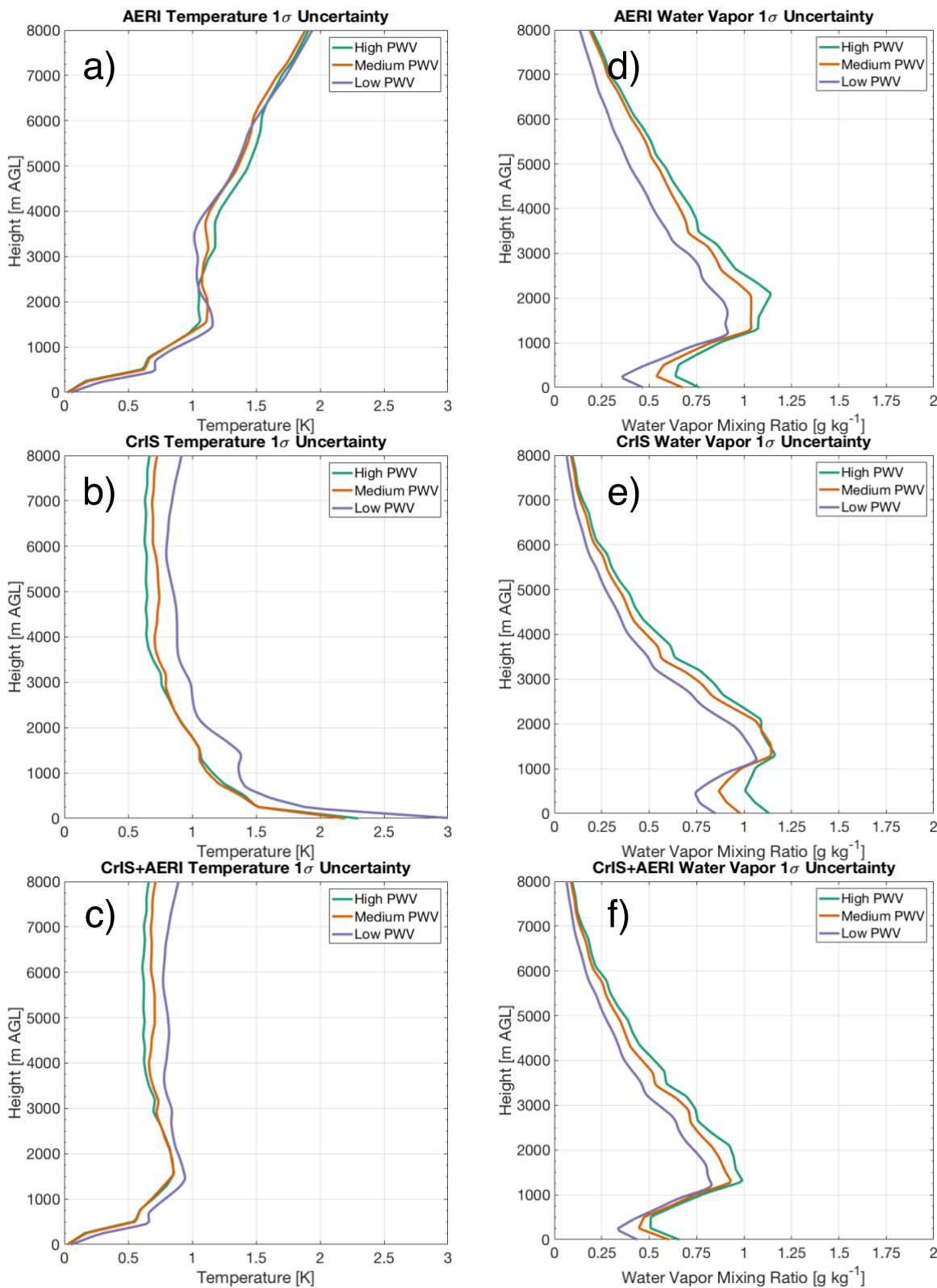


Figure 5.13: 1 σ uncertainties for temperature (a-c) and water vapor (d-f) for AERI (a and d), CrIS (b and e), and CrIS+AERI (c and f) in high (4+ cm, green), medium (2-3 cm, orange), and low (less than 1 cm, purple) PWV composites.

The composite mean profiles for uncertainty for the high, medium, and low PWV composites are presented in Figure 5.13. Overall, the environment has very little effect on changing the uncertainty profiles as the high and low PWV composite profiles are generally within 5 – 10% of the medium PWV composite. However, a general pattern can be identified that temperature uncertainties are slightly greater in dry environments, and water vapor uncertainties are greater in moist environments. CrIS appears to be most susceptible to changing environments, as water vapor uncertainties below 1000 m AGL can differ by as much 50% compared to the medium PWV state. CrIS+AERI reduces the variance in uncertainty that is dependent upon the atmospheric state and provides greater consistency in the uncertainty profiles, in addition to the reductions in uncertainty compared to CrIS alone.

5.5 Summary and Conclusions

This information content study has demonstrated the benefits of adding the AERI to the existing space-based operational hyperspectral IR sounding system in clear sky conditions. We have assessed these gains using DOF as a measure of information content and assessing the vertical resolution and uncertainties of temperature and water vapor sounding for AERI, CrIS, and CrIS+AERI for cloud-free conditions in three different climate regimes.

Adding the AERI to a retrieval with a space-based hyperspectral IR sounder, such as CrIS, results in a 30-40% increase in information across the entire troposphere for both temperature and water vapor. When focusing on the near-surface layer below 700 hPa, a synergy with the AERI provides double the temperature information and 1.5 times more water vapor information over what is currently provided by the space-based sounders alone. This improvement is consistent in

both dry and moist environments, despite the ranges of information content that both sensors have across varying PWV.

The combination of AERI with a space-based hyperspectral IR sounder results in significant improvements to the vertical resolution of the retrieval below 1000 m compared to what is currently available with a space-based hyperspectral IR sounder alone. The ground-/space-based synergy results in improved vertical resolutions from the surface up to 4000 m AGL. The vertical resolution of the CrIS+AERI synergy is better than the 1 km vertical resolution goal stated by the Decadal Survey below 1000 m AGL. While synergy does not meet the 1 km resolution soundings goal of the Decadal Survey above 1000 m AGL, the improvements to vertical resolution offered by a ground-/space-based synergy would improve the ability of retrievals to resolve PBL features like a capping inversion, resulting in better monitoring of convective initiation. We found that vertical resolution of temperature is best in moist environments, while the vertical resolution of the water vapor retrieval is best in dry environments. This is caused by AERI's far-IR channels being most sensitive to water vapor in dry environments, while the sensitivity of CrIS's midwave bands to water vapor result in CrIS's improved sounding of temperature in moist environments. This effect for CrIS would not be realized in retrievals that omit water vapor channels from its temperature retrieval (such as the method of Smith et al. 2021).

Similarly, the synergy between AERI and a space-based hyperspectral IR sounder results in a 50% decrease in uncertainties (compared to a space-based hyperspectral sounder alone) in the lowest 500 m. The Decadal Survey set a goal of 1 K uncertainties, which the CrIS+AERI synergy, explored in this study, exceeds throughout the troposphere. Water vapor mixing ratio uncertainty is reduced by 25% in the lowest 1000 m AGL but does not meet the 0.3 g kg^{-1} goal of the Decadal Survey. We have shown that this reduction in uncertainty is a result of the two instruments, with

their different views of the atmosphere, reducing the cross-layer correlations of uncertainties in the posterior correlation matrix. It has been shown that the ground-/space-based synergy produces a reduction in these uncertainties in both dry and moist environments, though the temperature uncertainties are somewhat greater in dry environments and water vapor uncertainties are greater in moist environments.

While the discussion in this chapter has focused on the improvements that AERI brings to the existing sounding methods with space-based hyperspectral IR sounders, users of ground-based sensors may realize benefits of a ground-/space-based synergy as well. We have found that the inclusion of a space-based hyperspectral IR sounder results in about a 20% increase in DOF across the surface to 700 hPa layer, compared to the ground-based AERI alone. The synergy also offers improvements to vertical resolution and uncertainties above 500 m AGL. Given that the ABI is the only instrument currently in geostationary orbit providing nearly continuous observations over North America, it may be worthwhile for ground-based instrumentation users to consider a synergy with the ABI. While we have found that a synergy with an imager like ABI does not result in increases in DOF near the surface (compared to the AERI alone), the ABI does increase DOF by about 15% in in the free troposphere.

Chapter 6: Cloudy Sky Information Content Analysis

6.1 Introduction

The effects of clouds on the synergy of upward and downward pointing sensors are under-researched as previous studies, such as Ebell et al. (2013) and the analysis presented in Chapter 5, have primarily focused on clear sky conditions. However, in an assessment of the HIRS sounder, Wylie and Menzel (1999) found that only 25% of observations were clear sky scenes, with 32% of observations being opaque clouds and 43% semi-transparent clouds. With the possible exception of the clear sky pre-convective environment, observations in cloudy sky conditions tend to be more important for reducing forecast errors (McNally 2002). While non-precipitating clouds are largely transparent at frequencies used for microwave sounding, clouds are significant emitters in the IR. Thus, the presence of clouds will significantly affect the shape of Jacobians and in turn the retrievals and NWP assimilation techniques that depend on those Jacobians.

Both NWP and thermodynamic retrievals that utilize IR radiances from space-based sensors will use various cloud-clearing methods in partly cloudy scenes and along the edges of cloud formations to make greater use of IR sounding data. Cloud-clearing attempts to remove the signal of the cloud in the radiance field in order to estimate the clear sky contribution to the observed radiances. The data assimilation or retrieval then uses that estimated cloud-cleared radiance. The NUCAPS retrieval supplements cloud-cleared IR radiances with microwave observations for its thermodynamic retrieval.

Outside of partly cloudy scenes and cloud edges where cloud-clearing methods may be applied, only microwave sensors offer observations below a cloud layer in the space-based observing system. However, Turner and Löhnert (2014) demonstrates that a ground-based IR

sensor may retrieve thermodynamic profiles up to the cloud base (and by the same logic a space-based IR sensor may retrieve down to the cloud top). In this regard, the ground-and-space-based synergy of IR sensors would pose a potential solution to IR sounding in cloudy environments. This setup would allow for the ground-based sensor to inform the retrieval below the cloud layer and the space-based sensor inform the retrieval above the cloud layer. While it seems intuitive how each sensor would inform the retrieval in environments with optically thick clouds, how that information would blend when clouds are not completely opaque and in partly cloudy scenes is an open question. How cloud cover affects the information content available above the cloud for a space-based sensor, and below the cloud for a ground-based sensor, is under-investigated as well. This section will present three case studies to incrementally advance the understanding of the information content of a ground-and-space-based synergy of IR sensors in cloudy sky conditions.

6.2 Experimental Design

Designing a synthetic study for cloudy sky scenes is difficult because clouds have a large amount of variability in terms of their height, thickness, and droplet size and density. Additionally, simulating cloudy sky radiances for IR hyperspectral sounders requires several orders of magnitude more calculations than clear sky radiances in order to account for the radiative effects due to the emission and scattering of clouds in the IR. This significantly limits the size of an analysis like this that attempts to account for clouds. Thus, this analysis will explore the synergy of CrIS+AERI using three case studies of single layer liquid water clouds. Recall that the results of the clear sky information content analysis in Chapter 4 suggest that AIRS and IASI would have similar results to CrIS – so the results with CrIS in this analysis would be expected to be similar if the analysis were to be applied to these other instruments. The three case study profiles are taken

from the radiosonde dataset at the ARM SGP site (Sisterton et al. 2016). The cloud height will significantly affect the location at which temperature Jacobians peak, while cloud properties will only somewhat alter the scattering properties of the cloud. Therefore, it is assumed that the information content of each sensor and the synergy will be more dependent on the height of the clouds than the cloud properties (like droplet size and number density). The three cases will vary the cloud base heights at 3000 m (Case 1), 2000 m (Case 2), and 500 m (Case 3) AGL while simulations will maintain the same cloud properties in each case. The temperature and dew point temperature profiles for the three cases are shown in Figure 6.1. For each case, the information content of the synergy will be assessed across varying cloud optical depths (COD) and varying cloud fraction.

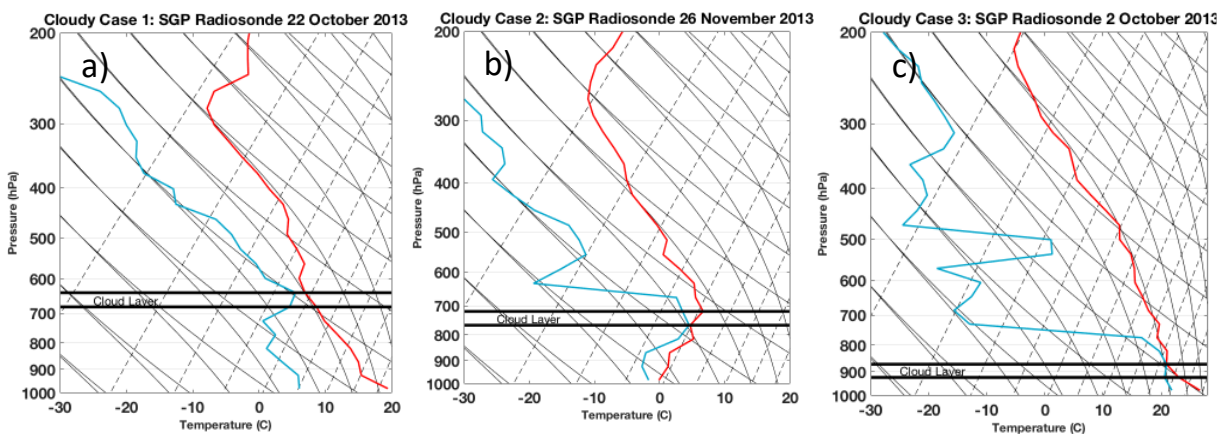


Figure 6.1: Temperature (red) and dew point temperature (blue) profiles used for each cloudy sky case, interpolated to the 500 m grid used for radiative transfer calculations. The black lines indicate the location of the cloud layer in the simulations.

6.2.1 Constructing the A Priori Covariance Matrix

Recall that calculating the averaging kernel (recall equation 2.21) requires an a priori covariance matrix \mathbf{S}_a (equation 2.8). The clear sky analysis in Chapter 5 utilized a pseudo-global a priori which comprised of profiles from all three ARM stations. This was done to ensure that \mathbf{S}_a was constant throughout the calculations to highlight the variations in information content caused

by water vapor. Both Aires (2011) and Ebell et al. (2013) have highlighted the sensitivity of retrievals to S_a . In practice, it is likely that the prior will be derived from a single location that is climatologically similar to the location of the sounding. For example, NUCAPS (gambacorta 2013) will utilize a climatology on a 2.5° grid as part of its prior lookup table. For the analysis in this section, since the three profiles are chosen from the SGP site, we utilize the 3,765 clear sky radiosonde profiles from SGP to construct S_a . This result is shown in Figure 6.2. Overall, while the magnitude of the values are different, the general patterns remain similar to the pseudo-global prior used in Chapter 5 (Figure 5.1).

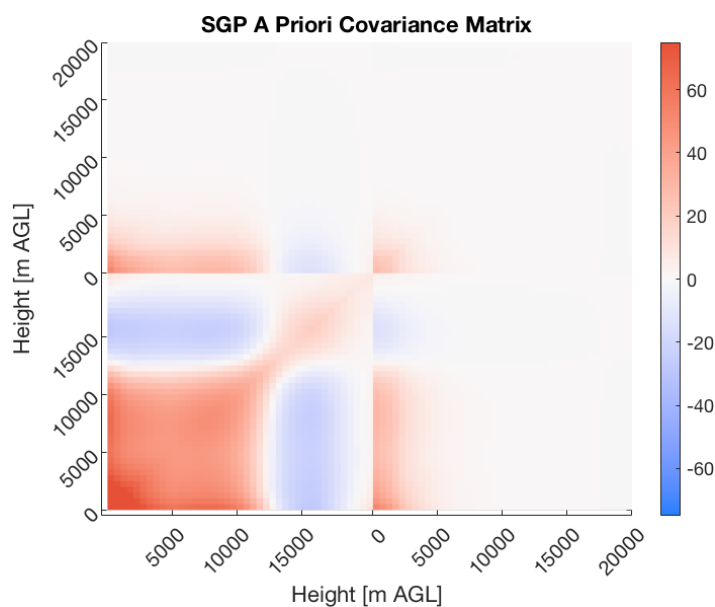


Figure 6.2: A priori covariance matrix used in this analysis. Bottom-left is temperature covaried against itself. Top-right is water vapor varied against itself. Top-left and bottom-right are temperature and water vapor covaried against each other.

6.2.2 Radiative Transfer Modelling

The LBLDISORT (LBLDIS, Turner et al. 2003, Turner 2005) model is used to simulate cloudy sky radiances for CrIS and AERI. LBLDIS utilizes layer optical depths for a given thermodynamic profile from LBLRTM (Clough et al. 2005), which are calculated assuming a

cloud-free atmosphere. LBLDIS computes the scattering and absorption of the cloud layer and combines that information with the cloud-free layer optical depths from LBLRTM in order to simulate cloudy sky radiances. The COD is varied to be run at: 0 (clear sky), 0.1, 0.5, 1, 5, 10, 20, and 40. In all three cases, a liquid water cloud is simulated with a gaussian distribution of droplets with an effective radius set to 7.5 μm . Conceptually, this is similar to a stratus cloud. LBLDIS is limited to 66 height levels, so instead of using the AIRS pressure grid, a 500 m grid is used up to 32.5 km (approximately 8 hPa). The vertical resolution of the grid is balanced with having layers in the upper stratosphere to account for radiative contributions above the tropopause that strongly impact space-based radiance measurements. In each case, the geometric thickness of the cloud is 500 m, or one model layer. Perturbations of +1 K and -10% water vapor mixing ratio are used at each level in order to calculate Jacobians for AERI and CrIS. Aside from the model difference, the radiative effects of carbon dioxide, methane, ozone, and nitrous oxide are considered in these simulations, just as in the clear sky analysis in Chapter 5. The same trace gas profiles used in Chapter 5 are applied in this analysis as well. The CAMEL dataset (Borbás et al. 2018 and Loveless et al. 2021) is also used to provide surface emissivity for the SGP site for these calculations. Finally, CrIS is simulated to have a nadir overpass, just as in the clear sky analysis in Chapter 5.

6.2.3 Computing Jacobians in Partly Cloudy Scenes

Because the sensitivity across the field of view (FOV) or field of regard (FOR) of an instrument is not uniform, radiances (and Jacobians) in partly cloudy scenes depend not only the aerial cloud fraction but also on the location of the clouds within the FOV or FOR. Being a ground-based instrument, AERI's FOV is so small that it is reasonable to assume that cloud cover is binary for AERI: either completely clear or completely cloudy. However, CrIS has a 14 km diameter

FOV at the surface when at nadir, and a FOR that consists of nine FOVs aligned in a 3x3 grid. At this point, the decision is made to simulate a match-up between CrIS and AERI where the retrieval is performed on the FOV that encompasses AERI's location, as opposed to the larger spatial footprint of the FOR. While most space-based retrievals (such as NUCAPS) utilize a radiance measurement averaged across the nine FOVs in a FOR, the decision to use a single FOV is made because the smaller FOV ensures the environment viewed by CrIS is closer to what is being measured by AERI. Furthermore, there is precedent to utilize the individual FOVs in this scenario, as cloud-clearing techniques will identify and utilize clear sky FOVs adjacent to the partly cloudy FOVs (eg: Susskind et al. 2003, Li et al. 2005).

Smith (1967) first showed that the total radiance I at frequency ν in partly cloudy scenes may be calculated as:

$$I_{\nu} = N I_{CD_{\nu}} + (1 - N)I_{CR_{\nu}} \quad (5.1)$$

where N is the cloud fraction and I_{CD} is the radiance from the cloudy part of the scene and I_{CR} is the radiance from the clear part of the scene. Equation 5.1 assumes a uniform sensitivity across the FOV though. The sensitivity of the CrIS FOV to the scene is quite complex (see Han et al. 2018) though it is generally most sensitive in the center of the FOV and least sensitive on the edges. Thus, the sensitivity of the FOV is approximated as a cone here (see Figure 6.3). Returning to equation 5.1, rather than the cloud fraction N , the clear and cloudy radiance contributions need to be weighted by the fraction of the total FOV sensitivity that is cloud covered (we will call this variable S_{CD}). Thus, our partly cloudy radiance I may be computed as:

$$I_{\nu} = S_{CD} I_{CD_{\nu}} + (1 - S_{CD})I_{CR_{\nu}} \quad (5.2)$$

This method to calculate the radiance assumes within the FOV, the clear and cloudy regions are homogenous within themselves. Radiative transfer calculations also assume that the same

thermodynamic profile is present across the FOV, with the presence of the cloud layer being the only difference between the clear and cloudy regions.

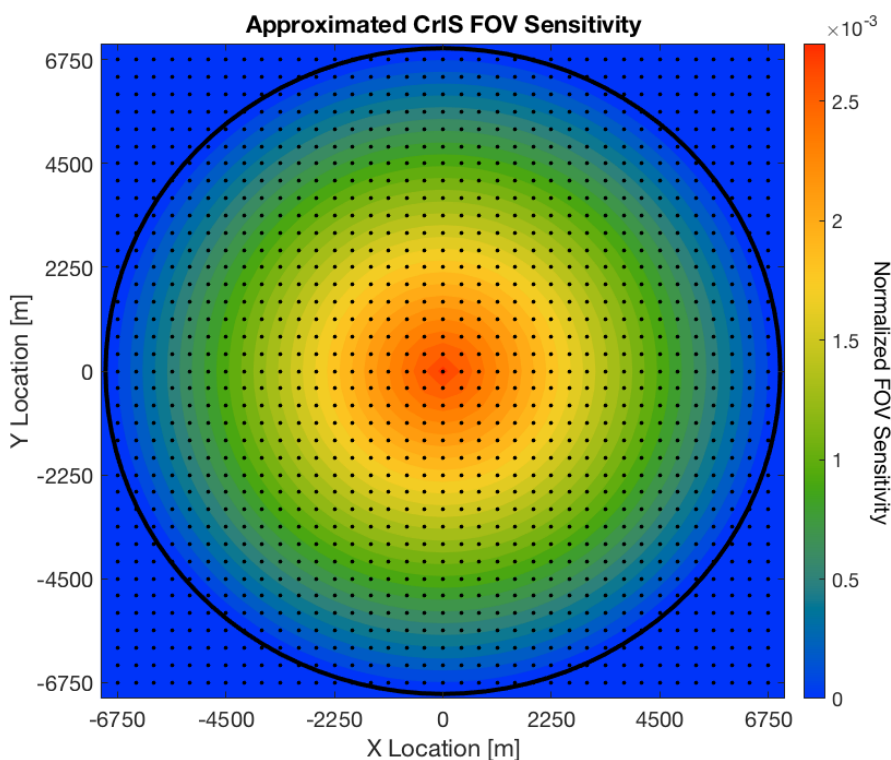


Figure 6.3: Approximate sensitivity of the CrIS FOV. Dots represent the 375 m grid of the resolution of the Visible Infrared Imaging Radiometer Suite (VIIRS).

Lastly, the locations of the clouds within the FOV must be simulated in order to calculate radiances in the partly cloudy scene. In practice, knowledge of the location of clouds within the CrIS FOV can be known from the Visible Infrared Imaging Radiometer Suite (VIIRS) that is onboard S-NPP and NOAA-20 with CrIS. The University of Wisconsin-Madison and University of Maryland Baltimore County produce collocated CrIS and VIIRS data for NASA (Revercomb and Strow, 2020). Li et al. (2005) has utilized a similar data product to perform cloud-clearing for AIRS radiances by using the Moderate Resolution Imaging Spectroradiometer (MODIS) that is onboard the Aqua satellite with AIRS. Therefore, a grid with spacing of 375 m (the spatial resolution of VIIRS, Hillger et al. 2013) is overlaid on the approximated CrIS sensitivity in order

to calculate S_{CD} (as shown in Figure 6.3). The selection of which pixels are clear or cloudy are selected randomly. Figures 6.4a, 6.4b, and 6.4c display the histograms of the total CrIS FOV sensitivity that is cloudy for 25%, 50%, and 75% areal cloud fractions respectively. Randomly selected pixels may roughly approximate scattered cumulus in the real world but will not simulate the scenario when clouds are completely contained to one side of the FOV. This additional scenario is accounted for in what will be referred to as Cloudy Scene 2, which simulates a cloud mass approaching from the south. The orientation of clear and cloudy pixels for approximately 25%, 50%, and 75% areal cloud fraction in this scenario is displayed in Figures 6.4d, 6.4e, and 6.4f respectively, which correspond to cloudy FOV sensitivities of about 16.6%, 52.6%, and 83.4% respectively.

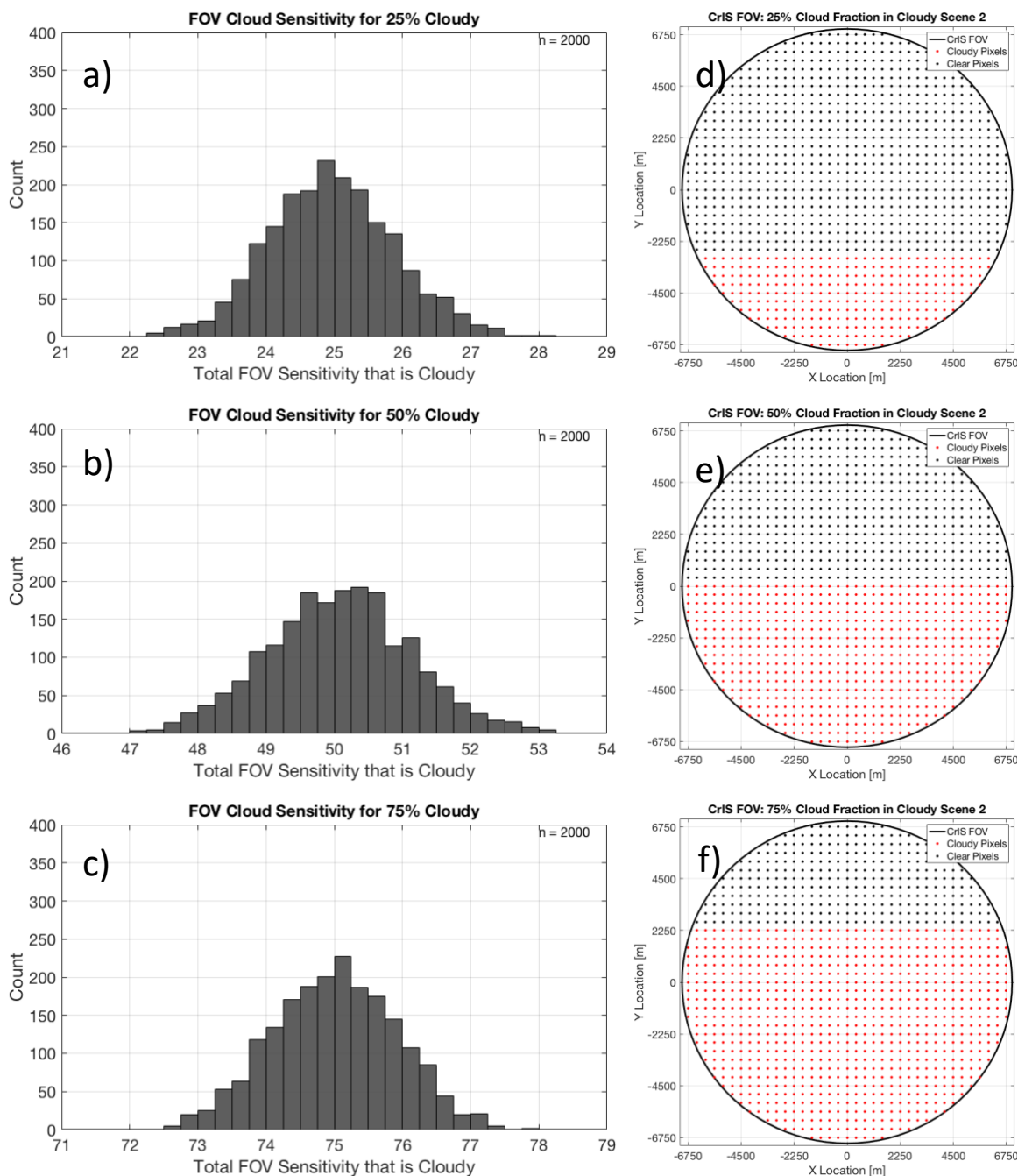


Figure 6.4: a-c display the histograms of the fraction of the total CrIS FOV sensitivity that is cloudy, given random placements of the clear and cloudy pixels, for 25% (a), 50% (b), and 75% (c) areal cloud fraction. d-f display the pattern of clear and cloudy pixels when simulating a cloud mass approaching from the south with 25% (d), 50% (e), and 75% (f) areal cloud fractions.

6.3 Results

The results will be organized such that we first consider the scenario with 100% aerial cloud fraction and observe changes in DOF (equation 2.22) with varying the COD for each of the three cases: Case 1 with a cloud base at 3000 m AGL, Case 2 with a cloud base at 2000 m AGL, and Case 3 with a cloud base at 500 m AGL. In the second section of the results, we keep COD equal to 40 and assess the changes in DOF for Case 2 (with a cloud base at 2000 m AGL) with respect to varying aerial cloud fraction.

6.3.1 Information Content with Varying Cloud Optical Depth

6.3.1a Case 1: 3000 m AGL Cloud Base

First, we will consider how information content varies with COD, given a cloud fraction of 100% and beginning with the Case 1 with the cloud base at 3000 m (and cloud top at 3500 m) AGL. DOF calculations for AERI, CrIS, and CrIS+AERI are shown in Figure 6.5. Across the full troposphere (designated as the surface to 200 hPa to maintain continuity with the clear sky analysis in Chapter 5), Figure 6.5a shows that both CrIS and AERI have greater DOF for temperature when the cloud is optically thin (COD less than 1) than in clear sky conditions. Optically thick clouds result in nearly the same total DOF as in clear sky conditions for each sensor though the vertical location of that information is very different in the two scenarios.

In Figure 6.5b it is shown that above the cloud (designated as the cloud top up to 200 hPa), AERI's DOF for temperature increases from a COD of 0 to a COD of 0.5, with a maximum in DOF occurring with a COD of 0.5. AERI's above-cloud temperature DOF decreases with increasing COD for CODs greater than 1 and approaches zero with a COD of 40. It would be expected that AERI has no information above optically thick clouds. Comparatively, CrIS's above-

cloud DOF for temperature increases with increasing COD, resulting in 1 DOF greater than clear sky conditions when the COD is greater than 5.

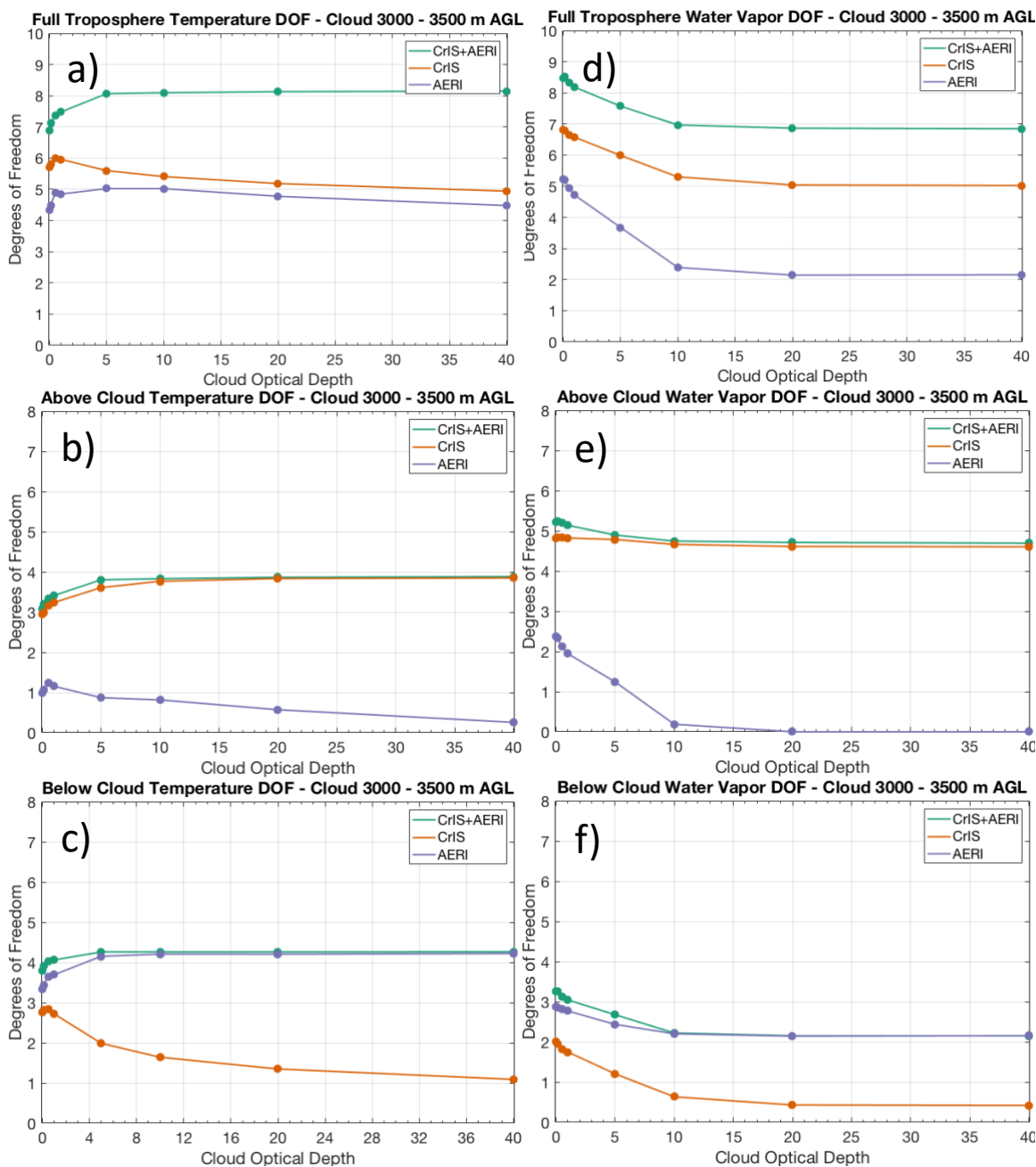


Figure 6.5: DOF for AERI (purple), CrIS (orange), and CrIS+AERI (green) for the full troposphere (a and d), above-cloud (b and e), and below-cloud (c and f). DOF for temperature is shown in the left column (a-c) and water vapor in the right column (d-f).

Figure 6.5c displays the DOF for temperature below the cloud (designated as the surface up to cloud base). Below the cloud, the sensors have the reversed relationships with COD. AERI's DOF increases as the cloud becomes optically thicker (similar to CrIS's above-cloud DOF). CrIS's below-cloud temperature DOF marginally increases as COD goes from 0 to 0.5. However, CODs greater than 1 result in less DOF than in clear sky conditions. Unlike AERI's temperature DOF above the cloud, CrIS's DOF below the cloud unexpectedly approaches one instead of zero. This will be addressed in further detail below.

Across Figures 6.5a, 6.5b, and 6.5c, it is shown that CrIS+AERI has greater DOF throughout the troposphere than AERI or CrIS alone. While the DOF from the surface to 200 hPa for both AERI and CrIS decreases marginally at high CODs compared to clear sky, CrIS+AERI actually has greater DOF at high COD (Figure 6.5a). This is because CrIS+AERI benefits from the increased DOF at high COD from CrIS above the cloud (Figure 6.5b), in addition to the increased DOF at high COD from AERI below the cloud (Figure 6.5c). Figures 6.5b and 6.5c also confirm the hypothesis that at high CODs, the synergy of CrIS+AERI will revert to what CrIS provides above the cloud and what AERI provides below the cloud.

The DOF for water vapor across the full troposphere is displayed in Figure 6.5d. Unlike the sensors' response with temperature, as COD increases, both AERI and CrIS lose water vapor information: CrIS losing 2 DOF and AERI losing 3 DOF compared to clear sky conditions. However, CrIS+AERI only loses about 1.5 DOF at high COD compared to clear sky. In the above-cloud layer (Figure 6.5e), the water vapor DOF from CrIS remains unchanged despite varying COD. AERI's water vapor DOF decreases compared to clear sky conditions as soon as the cloud is introduced (COD of 0.1) and goes to 0 at CODs greater than 10. CrIS+AERI has greater DOF above the cloud layer than CrIS in clear sky conditions, benefiting a small amount from the

additional information AERI provides above the cloud layer. But for CODs greater than 1, CrIS+AERI's DOF for water vapor above the cloud layer is completely derived from what CrIS provides above the cloud layer. Below the cloud layer (Figure 6.5f), DOF for CrIS decreases to less than one at high CODs. AERI loses 1 DOF at high COD compared to clear sky. For CODs greater than 1, the DOF for CrIS+AERI below the cloud is nearly equal to what is provided by AERI.

Figures 6.6a and 6.6b display the diagonal of the averaging kernel for temperature for AERI and CrIS respectively for simulations at select CODs. Given that DOF is the trace of the averaging kernel (equation 2.23), this shows the levels at which changes in information content are occurring. For both sensors, the cloud presents a boundary which acts to sharpen the temperature Jacobians at the level of the cloud, thus increasing information at that level. For AERI, that peak in information comes at the cloud base, while that peak comes at the cloud top for CrIS. The optically thick cloud allows each sensor to retrieve the temperature of the cloud layer, whereas in clear sky it would have very little information about that layer.

Figures 6.6c and 6.6d display the diagonal of the water vapor averaging kernels for AERI and CrIS respectively. Increasing COD results in less water vapor information for AERI above 1000 m AGL despite the cloud base being at 3000 m AGL. This is because the cloud saturates the AERI radiance measurement and in doing so, reduces the sensitivity of AERI to perturbations in the water vapor field at those levels. This can be seen in Figure 6.7 where AERI has large sensitivity to water vapor perturbations below 3000 m AGL in clear sky conditions but becomes less sensitive to perturbations in the water vapor profile as the cloud becomes optically thicker. Figure 6.6d shows that CrIS's water vapor information does not change above the cloud, despite varying CODs.

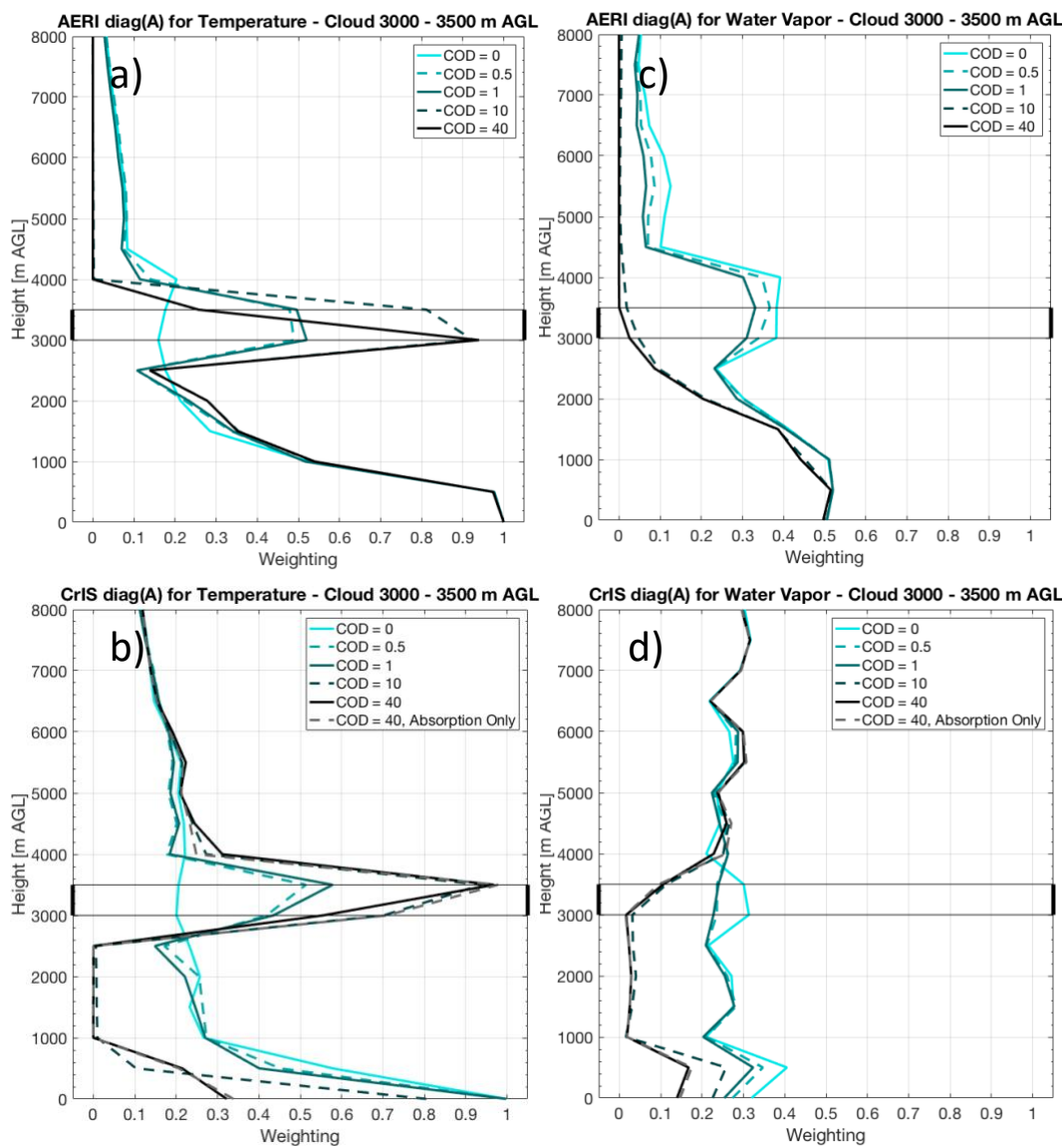


Figure 6.6: Diagonal of the averaging kernel for AERI (a and c) and CrIS (b and d) at select cloud optical depths. Diagonal of the averaging kernels for temperature are shown in a and b, and water vapor is displayed in c and d. Absorption only refers to the LBLDIS calculation that only considers the absorption of the cloud layer and not the contributions from scattering.

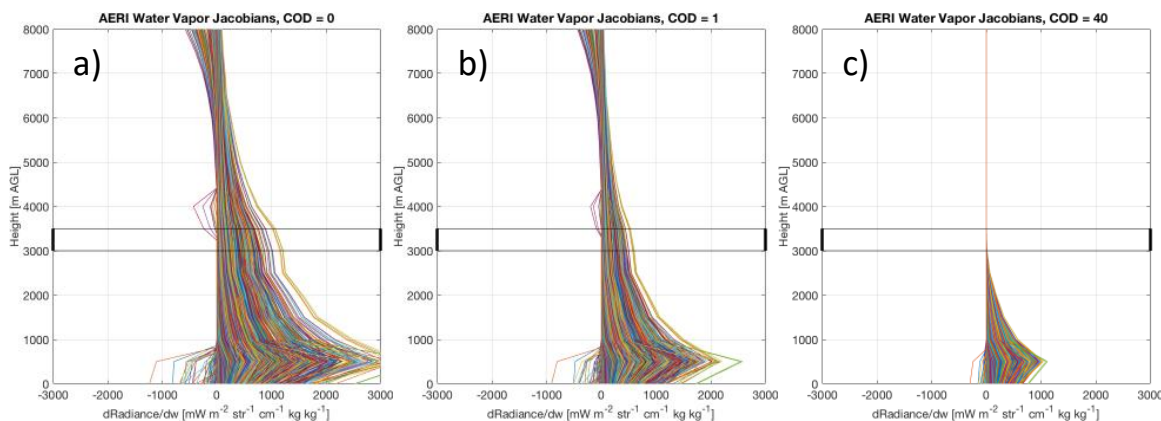


Figure 6.7: AERI water vapor Jacobians for clear sky (a), a cloud optical depth of 1 (b), and cloud optical depth of 40 (c).

Figures 6.6b and 6.6d also provide perspective for why the below-cloud DOF for CrIS is not zero (as would be expected) for a COD of 40. Some of the below-cloud DOF for CrIS comes from the cloud base, but there are also contributions to DOF from the surface and 500 m AGL. In order to test if this is a result of scattering of information through the cloud, LBLDIS is run to only consider the absorption of the cloud – this result is also displayed in Figures 6.6b and 6.6d. The absorption-only run produces nearly the exact same result as the full LBLDIS calculations. Similar results are found when setting surface emissivity equal to zero. Temperature and water vapor Jacobians for CrIS with a COD of 40, presented in Figures 6.8a and 6.8b, reveal that this information comes from a weak sensitivity at 500 m AGL and below in the longwave from 700 cm^{-1} to 1100 cm^{-1} and in the midwave from 1400 cm^{-1} to 1800 cm^{-1} . These unexpected results will be discussed further in the next section.

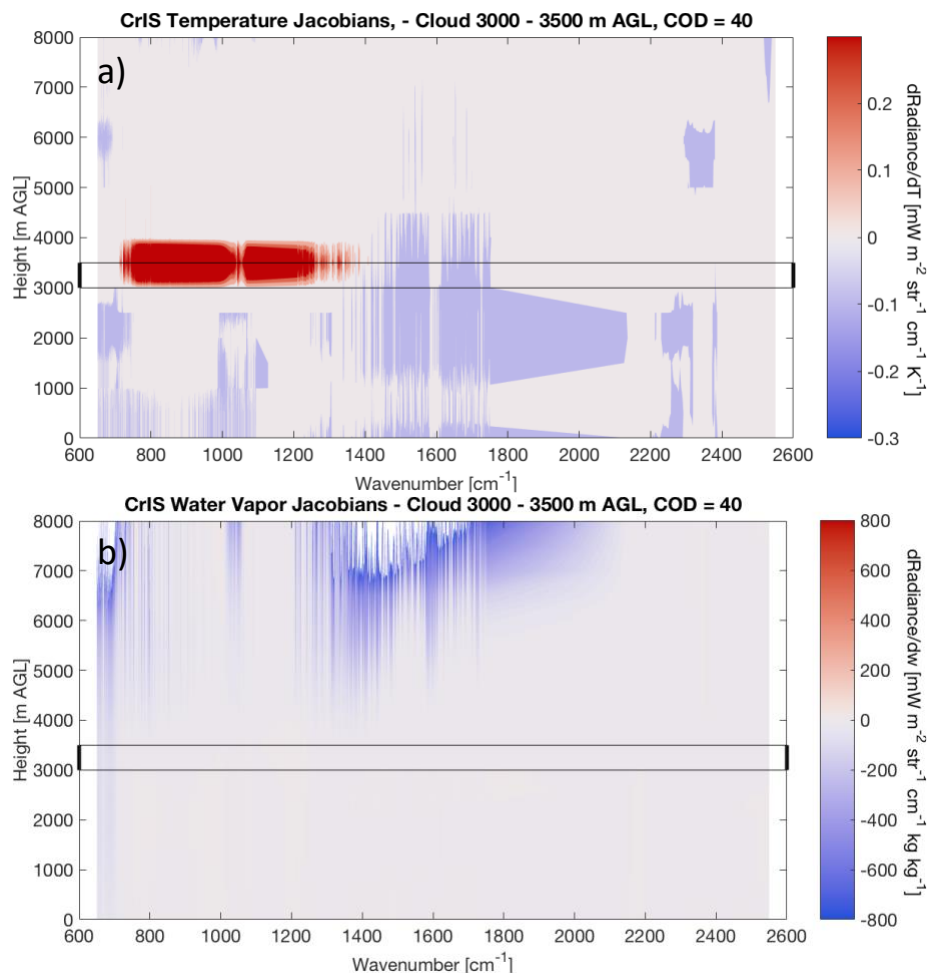


Figure 6.8: CrIS temperature (a) and water vapor (b) Jacobians for a cloud optical depth of 40.

6.3.1b Case 2: 2000 m AGL Cloud Base

Figure 6.9 displays the DOF for Case 2 with a cloud base at 2000 m AGL. Overall, similar patterns to what was seen in Case 1 persist with the cloud base just 1000 m lower. While AERI and CrIS lose about 0.5 and 1 DOF respectively throughout the troposphere for temperature in a scene with an optically thick cloud compared to clear sky, CrIS+AERI gains 1 DOF (Figure 6.9a). CrIS+AERI benefits from both the increased above-cloud DOF (Figure 6.9b) for CrIS, and the increased below-cloud DOF (Figure 6.9c) for AERI, without suffering the loss of information that both sensors have at high CODs.

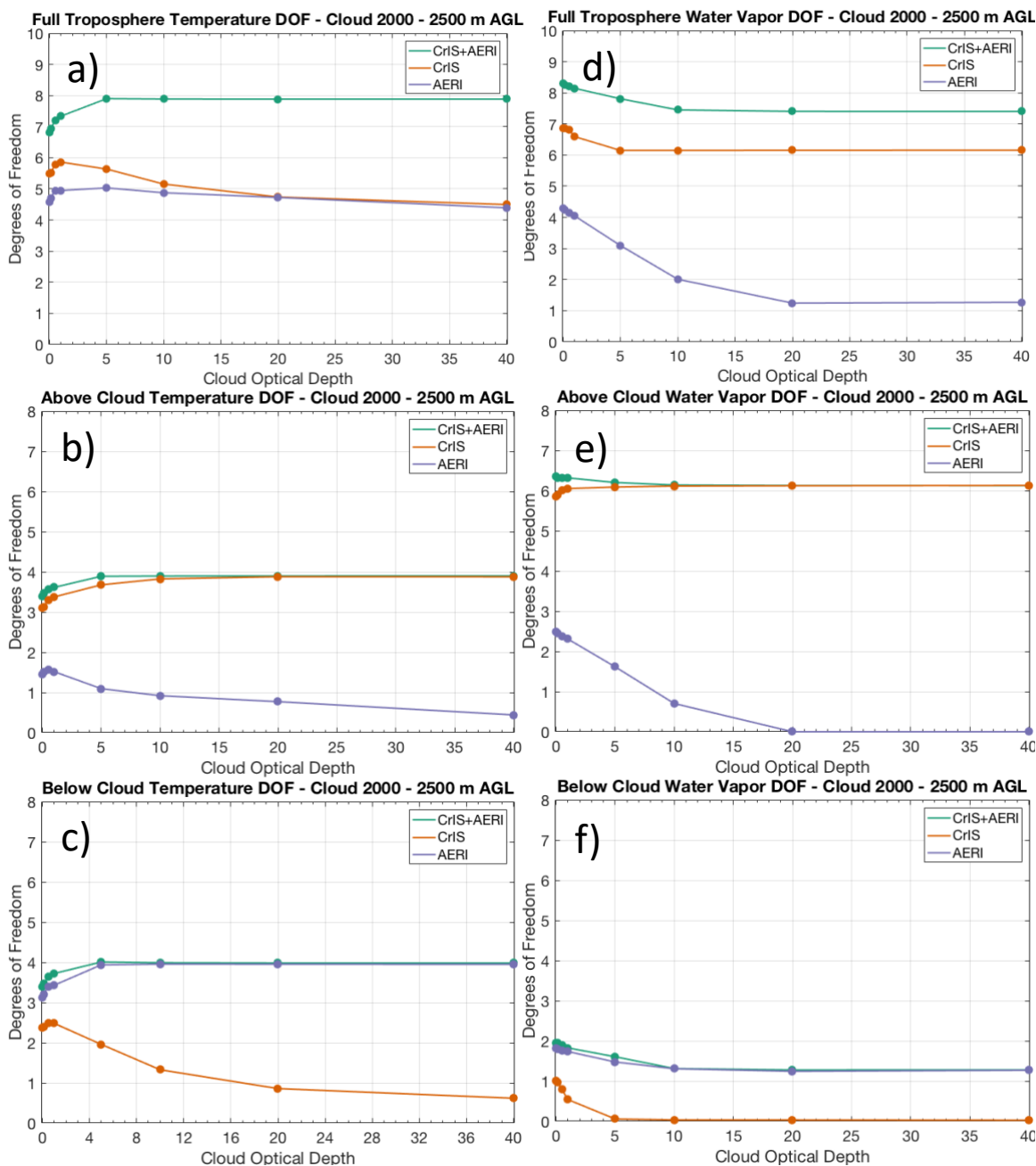


Figure 6.9: Same as in Figure 6.5 but for a cloud base of 2000 m AGL.

As seen in Figure 6.9d, water vapor DOF across the full troposphere for the 2000 m AGL cloud base behaves similarly to the 3000 m AGL cloud in Case 1 as well. While CrIS loses almost 1 DOF at high CODs compared to clear sky and AERI loses 3 DOF, CrIS+AERI only loses 0.75 DOF for water vapor across the full troposphere. Above the cloud (Figure 6.9e), AERI's water vapor DOF decreases as the cloud becomes optically thicker and goes to zero at CODs of 20 and

greater. CrIS's above-cloud water vapor DOF remains nearly the same across the range of CODs simulated here. Below the cloud (Figure 6.9f), CrIS's water vapor DOF goes to zero and AERI's decreases by about 0.5 DOF at high CODs compared to clear sky. CrIS+AERI reverts to CrIS above the cloud and AERI below the cloud at CODs greater than 5.

The trace of the diagonal of the averaging kernel for select CODs is presented in Figure 6.10. Just as was shown with a cloud base at 3000 m AGL, increasing the COD of the 2000 m AGL cloud results in an increase of temperature information at the cloud top for CrIS, and at the cloud base for AERI. Increasing COD has minimal effect on water vapor information above the cloud for CrIS but results in a decrease of water vapor information between 1000 m AGL and the cloud base for AERI. AERI's decrease in water vapor information below the cloud is a result of the cloud saturating the spectrum, reducing the sensitivity to small perturbations in the water vapor field (as was shown for the 3000 m AGL cloud in Figure 6.8).

One key difference between the 2000 m AGL cloud base case and the 3000 m AGL cloud base case is CrIS's information below the cloud layer at high CODs. While Case 1 with a 3000 m AGL cloud base showed CrIS having information at 500 m AGL and the surface for both temperature and water vapor with a COD of 40, CrIS's information at a COD of 40 is zero below the cloud base for both temperature and water vapor in the 2000 m AGL cloud case. This is the pattern that would be expected of CrIS at high CODs, as opposed to the unexpected result of Case 1. As will be shown in Case 3, it is not likely that this difference is a result of the differing cloud heights.

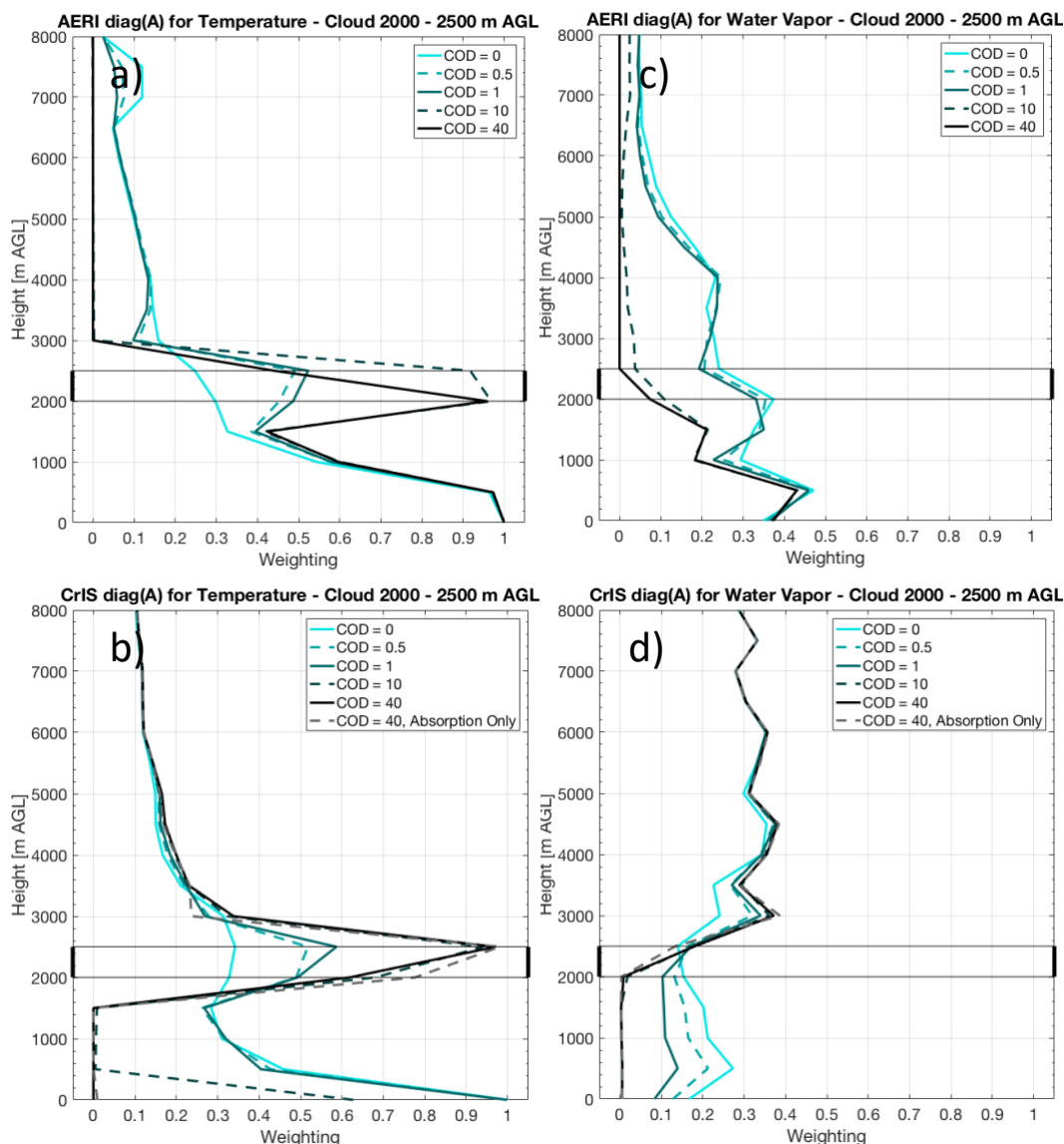


Figure 6.10: Same as in Figure 6.6 but for a cloud base of 2000 m AGL.

6.3.1c Case 3: 500 m AGL Cloud Base

The DOF for Case 3 with the cloud base at 500 m AGL is displayed in Figure 6.11. In Case 1 and Case 2, AERI's above-cloud DOF for temperature increased compared to clear sky conditions for the simulations with COD less than 1 (Figures 6.5b and 6.9b). In this case, the cloud layer is so low that AERI's above-cloud DOF for temperature only decreases with increasing COD compared to clear sky. At high optical depths, AERI only lost 1 DOF for temperature above the cloud in Case 1 (Figure 6.5b) and 2 (Figure 6.9b) but in Case 3 AERI loses 2 DOF compared to

clear sky. Figure 6.11c shows that below the cloud layer AERI does not see an increase in DOF with increased COD as what shown in Case 1 (Figure 6.5c) and 2 (Figure 6.9c), but this is because there are only two model layers below the cloud so 2 DOF is the maximum DOF possible below the cloud. Figure 6.12a shows that the cloud is so low that AERI has the maximum information from the surface to 500 m AGL layer in clear sky, so the additional absorption of the cloud does not provide additional information as was seen in Case 1 and Case 2. The increasing COD only reduces AERI's temperature information above the cloud. In Figure 6.11e it is shown that AERI's above-cloud DOF for water vapor decreases with increasing COD, just as was seen in Case 1 and Case 2. Below the cloud in Figure 6.11f, the cloud is again so low that changing the COD does not affect the DOF for AERI. Synthesizing the three cases together, the lower the cloud is, the less information that AERI may derive from the atmosphere.

While AERI is significantly limited in its total DOF by low clouds, CrIS is least affected by the 500 m AGL cloud compared to Case 1 and Case 2. The total DOF for CrIS for both temperature and water vapor (shown in Figure 6.11a and 6.11d respectively) across the full troposphere changes very little with varying COD. Similar to what was seen in the previous cases, the increased absorption by the cloud results in CrIS gaining temperature information about the cloud top (Figure 6.12b) at the expense of information below the cloud layer. Combining the information shown in Figures 6.11b, 6.11c, and 6.12b, CrIS has so little information below the 500 m AGL cloud base to start with that the increased temperature DOF above the cloud cancels out the losses below the cloud at high CODs. This combination results in nearly the same DOF across the troposphere in clear sky as with a COD of 40. The water vapor DOF for CrIS has very little change either above-cloud (Figure 6.11e) or below the cloud (Figure 6.11f).

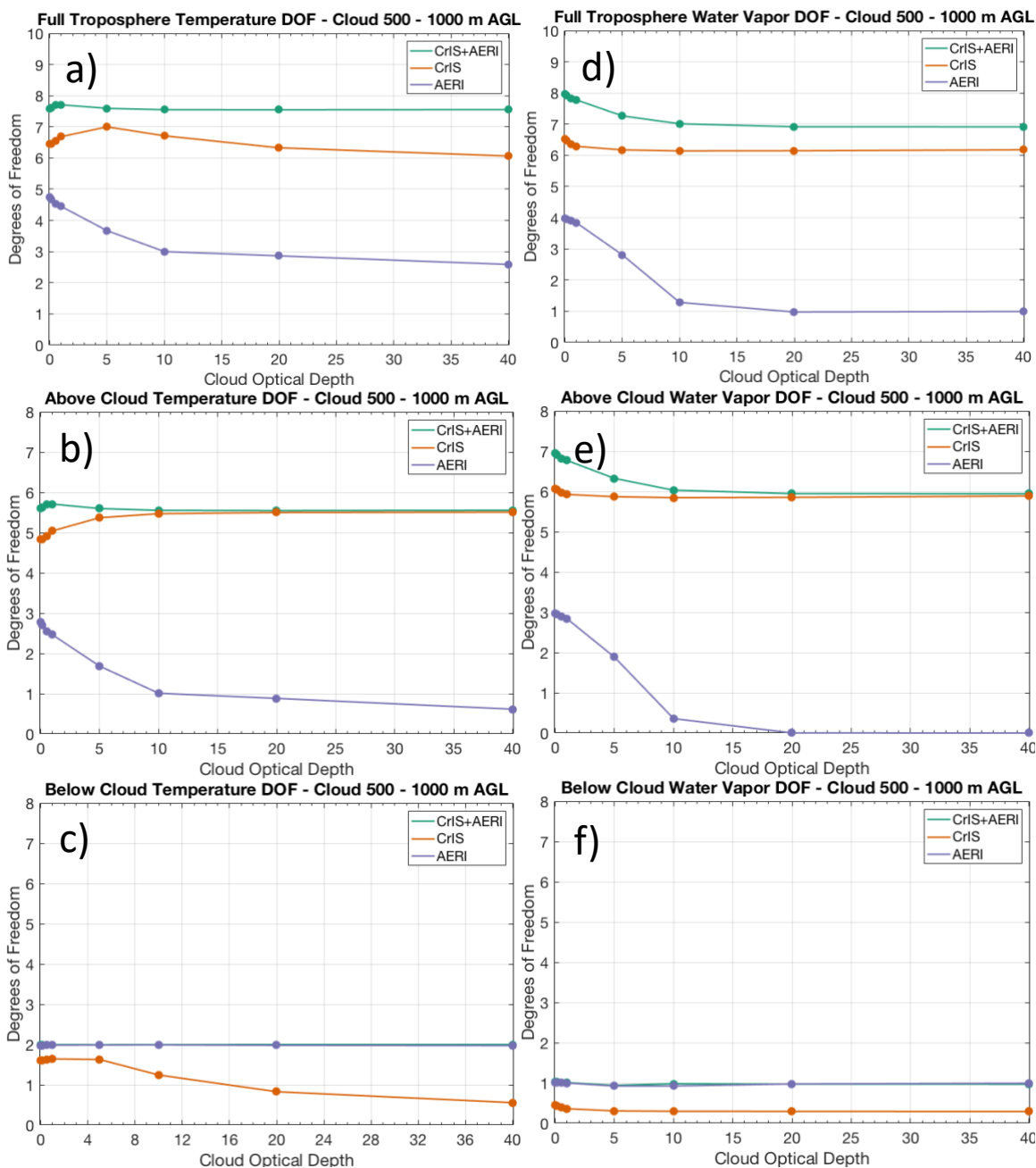


Figure 6.11: Same as in Figure 6.5 but for a cloud base of 500 m AGL.

While the total DOF for CrIS is similar in both clear sky and with a COD of 40, the vertical location of that information changes, resulting in CrIS having very little information below the cloud. While AERI provides very little information at high CODs in this case, it still provides observations of the PBL where CrIS cannot make observations due to the absorption of the cloud.

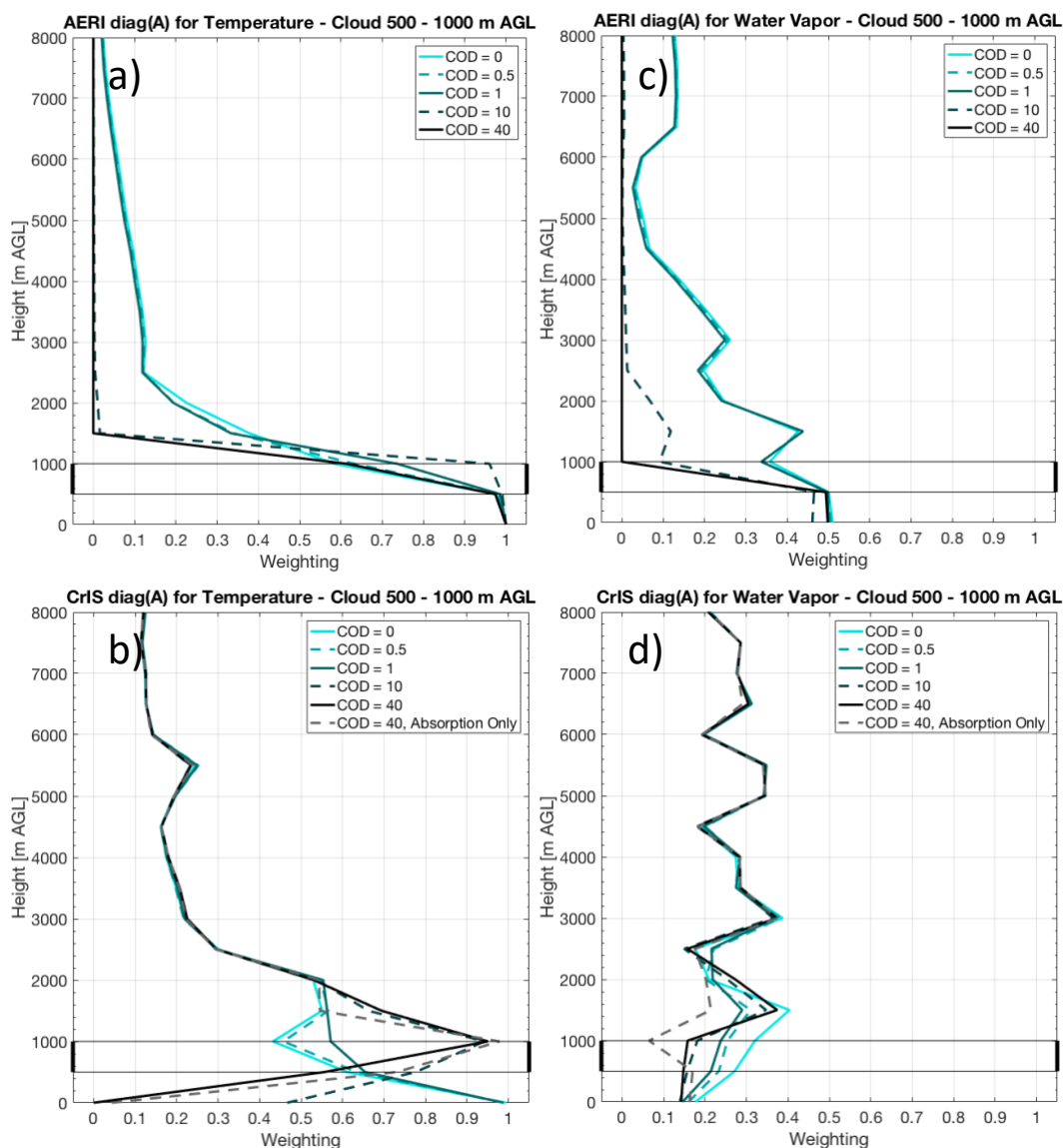


Figure 6.12: Same as in Figure 6.6 but for a cloud base of 500 m AGL.

In Figure 6.12d, we can also see that the model produces an unrealistic signal for CrIS below the cloud at high CODs, as was seen with Case 1. CrIS's water vapor information throughout the troposphere is nearly identical for every simulation above 1500 m AGL. At the cloud top (at 1000 m AGL), the clear sky simulation results in the greatest information, and increasing optical depths result in decreased information (COD of 40 results in the least information). The same pattern is seen at 500 m AGL at the cloud base. However, the varying CODs does not result in a

meaningful change in water vapor information at the surface. Recall that in Case 1 (Figure 6.6d), the water vapor information did decrease at the surface with increased COD, it just did not go to zero as expected. This suggests that there is not necessarily something unique about a cloud at 2000 m AGL, but rather these features are a result of modelling error of some unknown cause.

6.3.2 A Comment on Unexpected Results

The hypothesis coming into this analysis would be that at high CODs and 100% cloud cover, the above-cloud information content of AERI and the below-cloud information content for CrIS would be zero. Across the three cases, we see that the above-cloud DOF for AERI approaches zero (only the height index that is the cloud top provides a small bit of information above the cloud, which is included as part of the above-cloud DOF summation). However, for CrIS Cases 1 and 3 result in information originating from the near-surface layer even at high CODs (as was shown in Figures 6.6b and 6.6d for Case 1, and. 6.12b and 6.12d for Case 3). Comparatively, Case 2 followed our hypotheses exactly, as CrIS's below-cloud information went to zero (besides a small bit of information from the height index that is the cloud base). Furthermore, CrIS's below-cloud information does not follow the same pattern in Case 1 and Case 3. In Case 1, CrIS has non-zero temperature and water vapor DOF below the optically thick cloud. In Case 3, only CrIS's below-cloud water vapor DOF is non-zero.

Given the inconsistencies in how CrIS's below-cloud information behaves, it is difficult to conclude that this is a physical phenomenon, having signal below an optically thick cloud. Case 2 is colder than Cases 1 and 3 (Figure 6.1), so it is possible that the cooler atmosphere with lower specific humidity explains some of the differences. In general though, given the relationship of transmission (t) to optical depth (τ):

$$t = e^{-\tau} \quad (5.3)$$

there is no reason to expect radiative signal of the surface to be transmitted through a cloud with an optical depth of 40 (transmittance would be about 10^{-18}), even in scenes with a warm and moist PBL. It was shown in Figures 6.6, and 6.12 that this information is not being scattered through the cloud. One path of further exploration on the topic would be assessing the CODs that the model interpolates at IR frequencies because the model assumes that the user-input COD is at a visible frequency.

6.3.3 Information Content with Varying Cloud Fraction

To calculate information content with varying cloud fraction, locations of clouds within the CrIS FOV are randomly chosen in order to determine the fraction of the total CrIS FOV sensitivity that is cloudy. We also consider the situation where the clouds are constrained to one side of the FOV, simulating an approaching cloud mass (Cloudy Scenario 2). The distribution of the cloud covered FOV sensitivities from the random simulations and the pattern of Cloudy Scenario 2 are shown in Figure 6.4. Given the similarity of the three cases analyzed in the previous section, the rest of this analysis will focus on Case 2 with the cloud base at 2000 m AGL since the below-cloud DOF for CrIS in that case behaved as we would expect at high CODs. The partly cloudy scenes are simulated to have a COD of 40.

Figure 6.13 displays the box plot representing the range of DOFs possible for CrIS in the above- and below-cloud layers. Given the lack of variability produced by randomly selecting locations of cloudy and clear pixels within the FOV, the mathematical maximum and minimum cloud covered fraction of the total FOV sensitivity (S_{CD}) for a given aerial cloud fraction are also simulated and are displayed in Figure 6.13 for reference. This simulates the largely unrealistic

scenario where clouds are only located at the center of the FOV (maximizing the sensitivity of the FOV to the cloud cover) and when clouds are located around the edges of the FOV (minimizing the sensitivity of the FOV to the cloud cover). Figure 6.13 also shows that the DOF in the scenario where the cloud shield is contained to one side of the FOV (Cloudy Scenario 2) is not much different than the average of a large number of random simulations. In general, it is shown that increasing cloud fraction causes similar response in DOF to increasing COD shown in the previous section. CrIS's above-cloud DOF for temperature increases with increasing cloud fraction, and below-cloud DOF for temperature decreases with increasing cloud fraction (Figure 6.13a). Above-cloud DOF for water vapor remains similar with increasing cloud fraction, similar to the pattern shown in Figure 6.9e with increasing COD. Below-cloud DOF for water vapor goes to zero as the cloud fraction increases, the same response as with high CODs. The response of CrIS DOF to cloud cover is greatest when the aerial cloud fraction is greater than 50%. Sun et al. (2017) compares the NUCAPS retrieval to radiosondes with varying cloud fraction. While the IR measurements are supplemented with a microwave sounder in NUCAPS, they found that retrieval errors are also most sensitive when cloud fraction is greater than 50%.

In general, the greatest mathematically feasible variations occur with the 50% and 75% aerial cloud fractions – of which CrIS's below-cloud DOF is most sensitive to those variations. CrIS's below-cloud DOF can vary up to 0.75 DOF for both temperature and water vapor at a cloud fraction of 75% simply based on the location of clouds within the FOV. The methods used to simulate cloud location within the FOV here did not identify the full extent of those mathematically feasible variations. However, given the patterns of clouds required for the maximum and minimum cloud covered FOV sensitivity, it is not something likely to be seen in the real world.

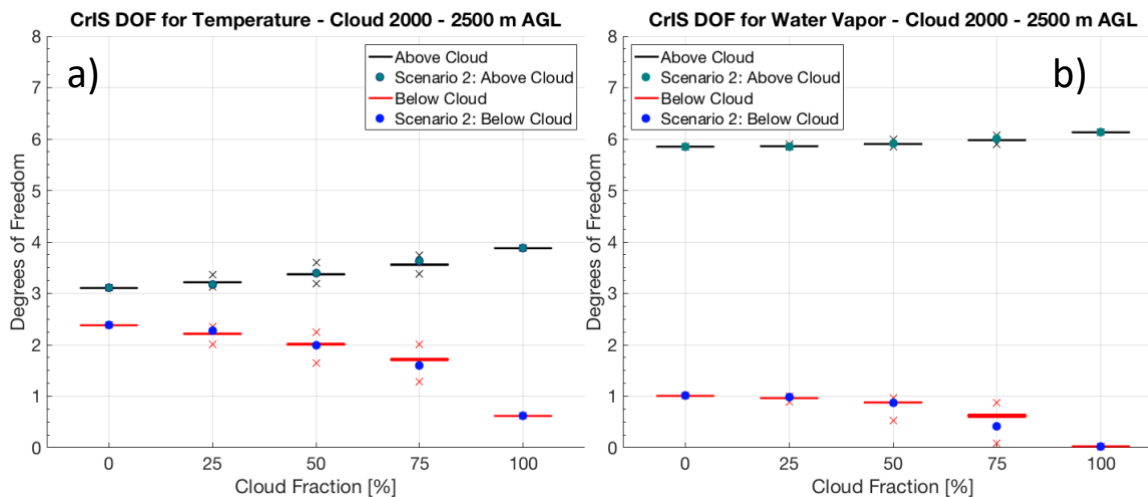


Figure 6.13: CrIS DOF for temperature (a) and water vapor (b). Above-cloud DOF is represented in black, below-cloud DOF represented in red. For reference, the DOF at the mathematical maximum and minimum sensitivity possible for the given areal cloud fraction are represented with an x. Teal and blue dots represent DOF in cloudy scenario 2 for above-cloud and below-cloud respectively.

The box plots for DOF for CrIS+AERI in the above-cloud and below-cloud layers are presented in Figure 6.14. Because AERI's cloud cover is binary, the partly cloudy scenes are simulated to have AERI with and without cloud cover. While the AERI cloudy sky simulation at 0% cloud fraction, and AERI clear sky simulation at 100% cloud fraction are physically impossible, they are presented to show the end points of those simulations where AERI would be located in the single cloudy pixel with a cloud fraction less than 1% and located in the single clear pixel with a cloud fraction greater than 99% respectively.

In general, it is shown that the synergy of CrIS+AERI has significantly less variability with cloud fraction than CrIS alone. Above the cloud, the synergy only changes about 0.25 DOF when AERI is in clear sky versus cloudy sky. Below the cloud, that difference is about 0.5 DOF for temperature and ranges from approximately 0.25 DOF for water vapor with a 0% cloud fraction to 0.75 DOF at 100% cloud cover. In the case of the synergy of CrIS+AERI, above-cloud DOF for temperature is most sensitive near cloud fractions of 0% – as any cloud cover introduced results

in the increased absorption at the cloud layer, resulting in the increased DOF (as was explained in the previous section). Otherwise, the synergy has almost the exact same DOF despite the varying cloud fraction. This means that the information content of the ground-and-space-based synergy in cloudy scenes would not only be greater than that of CrIS alone, but also more consistent regardless of the scene.

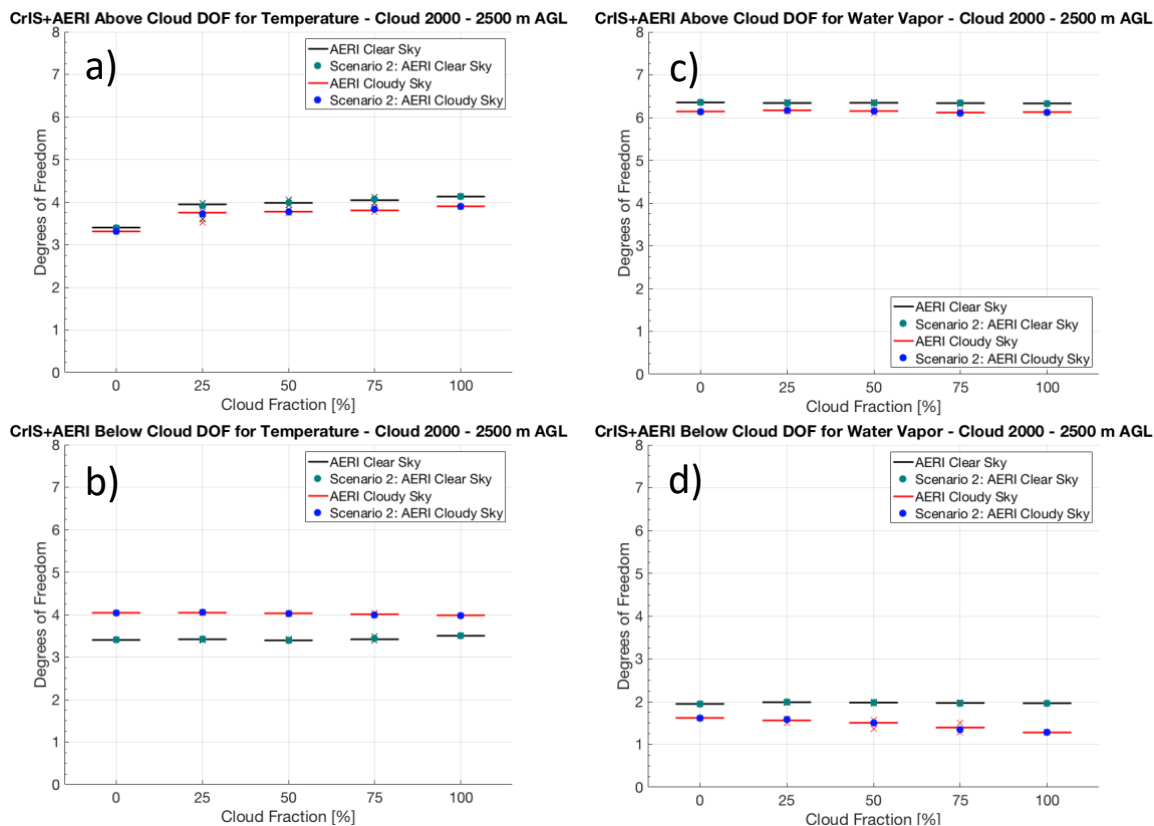


Figure 6.14: CrIS+AERI DOF for temperature (a and b) and water vapor (c and d). Above-cloud DOF is presented in a) and c) and below-cloud DOF presented in b) and d). The simulations for AERI in clear sky are presented in black, and AERI in cloudy sky presented in red. For reference, the DOF at the mathematical maximum and minimum sensitivity possible for the given areal cloud fraction are represented with an x. Teal and blue dots represent DOF in cloudy scenario 2 when AERI is in clear sky and when AERI is in cloudy sky respectively.

6.5 Summary and Conclusions

This chapter has assessed the DOF of CrIS and AERI in cloudy sky conditions in order to understand the benefits of the synergy of CrIS+AERI with varying COD and varying cloud fraction. Simulations shown here confirm the hypothesis that in the case of an optically thick cloud, the synergy of CrIS+AERI would be informed by CrIS above the cloud layer and informed by AERI below the cloud layer. It is found that CODs greater than one result in a decrease in total DOF across the troposphere compared to clear sky conditions for both AERI and CrIS. However, the synergy of CrIS+AERI loses less total water vapor information than CrIS or AERI while also increasing the total temperature information compared to a clear sky scene. Introducing AERI to the observing system helps mitigate the loss of IR sounding information in scenes with opaque clouds because AERI provides the information below the cloud layer that is otherwise lost when using a space-based IR sounder alone. As shown in Chapter 5 in clear sky conditions, the synergy maximizes the information available from both of these sensors.

The information content of CrIS with varying cloud fraction behaves similarly to varying the COD, with greater cloud fraction acting as an increase in COD. Effects of the clouds on DOF in the partly cloudy scene are most sensitive when cloud fractions are greater than 50%. The 2000 simulations of randomly selecting the locations of cloudy and clear pixels within the CrIS FOV did not produce much variability in CrIS DOF for given aerial cloud fractions. It has been shown however, that below-cloud DOF for CrIS could vary up to 0.75 when considering the mathematically possible maximum and minimum in cloud covered FOV sensitivity (though this variation is likely an over-estimation given the cloud patterns necessary to create those variations). However, the synergy of CrIS+AERI is not sensitive to the location of clouds within the CrIS

FOV. This analysis has assumed a homogenous CrIS FOV, and testing that assumption is necessary to prove the benefits and viability of the synergy in both clear sky and cloudy sky scenes.

While the unexpected and unexplained result of CrIS having non-zero information content below optically thick clouds does not restrict us from drawing important conclusions on the performance of the synergy of CrIS+AERI in cloudy skies, the model should be further evaluated to understand why it produces the results it does. It has been suggested that assessing how the model assigns CODs to the IR frequencies after receiving a user-input COD at visible frequencies is one path of further exploration.

The changes in information content with cloud cover for CrIS and AERI shown here suggest that retrievals from IR sensors should be evaluated cloudy environments in addition to clear sky environments. Sun et al. (2017) assessed the accuracy of NUCAPS temperature retrieval compared to radiosondes across varying cloud fractions and found that the retrieval had similar performance regardless of cloud fraction from the middle troposphere (650 hPa by their designation) up to the stratosphere. However, the differences between radiosonde and retrieval went from 1.5 K at 0% cloud fraction to 2.5 K at 85% cloud fraction for the surface to 650 hPa layer. Like Sun et al. (2017), the simulations for partly cloudy scenes shown here also suggested that CrIS is most sensitive to cloud cover when the FOV has greater than 50% aerial cloud fraction. While NUCAPS utilizes both IR and microwave space-based sounders in its retrieval, results of Ebell et al. (2013) suggest that a space-based microwave sounder would provide only 1 DOF for temperature and nearly zero DOF for water vapor below 3 km. In this sense, AERI (and particularly the synergy of CrIS+AERI) still provides an improvement over the current space-based observing system, even when the IR sensors are limited by cloud cover. Based the results in this Chapter, supplementing CrIS with ground-based AERI observations in cloudy sky scenes would be

expected to reduce the retrieval errors that Sun et al. (2017) found in both partly cloudy and fully overcast scenes.

One limitation of a synthetic study of this sort is that all of the information known for the modelling, which is not always practical in an operational setting. IR sounding in cloudy environments requires observations from additional instruments. The imagers that make collocated observations with AIRS and CrIS are able to derive cloud top pressure and some cloud properties, which could be used in modeling the cloudy sky radiances for a retrieval in the cloudy scene. From the ground-based perspective, the AERIOe retrieval (Turner and Löhnert 2014, Turner and Blumberg 2019) requires cloud base height observations from another instrument. Currently AERI's are deployed in research settings and almost always collocated with a ceilometer or lidar that could provide such observations. One requirement of a future network of ground-based profilers would be to have lidars or ceilometers collocated with an IR sensor for this reason. While an active sensor like a lidar or ceilometer would be able to identify clouds with very low optical depths, work by Ackerman et al. (2008) suggest that cloud masks from passive visible and IR imagers are only reliable when the COD is greater than 0.4. Thus, the small increases in DOF for semi-transparent clouds compared to clear sky conditions may not be realized in practice if the IR retrieval depends on the cloud mask from a visible and IR imager to determine if clouds are present. The computational expense of calculating cloudy sky radiances also limits the practicality of IR sounding in cloudy sky environments. AERIOe for example utilizes the cloud base height to make assumptions about the cloud contributions to the radiance field before retrieving temperature and water vapor below that height. Recent work by Martinazzo et al. (2021) to create a fast model for cloudy sky radiances in the IR may make simulations of cloudy sky radiances more practical on the timescales necessary for operational retrievals.

Chapter 7: Developing a Synergistic Retrieval

7.1 Introduction

To this point, it has been demonstrated that the synergy of ground-based and space-based sensors provides greater information content and vertical resolution in the lower troposphere compared to the current observing system, which is space-based only. These results have been displayed for synthetic information content analyses that have used radiosonde profiles as input conditions for radiative transfer calculations. This chapter will utilize real radiance measurements from CrIS and AERI to display that the improvements the synthetic information content analyses showed for the synergy of CrIS+AERI may be replicated in practice with an optimal estimation retrieval.

A pristine clear sky case is identified on 20 June 2015 from the PECAN (Geerts et al. 2017) dataset. On this day, AERI was located in central Kansas and S-NPP CrIS made an overpass at approximately 830 UTC. A radiosonde collocated with the AERI was launched at 900 UTC. This provides an ideal set up where the CrIS overpass is close in time to the radiosonde observation, which will be the reference to assess retrieval performance. Figure 7.1 displays the location of the AERI within the CrIS granule. Each point in Figure 7.1 represents a CrIS FOR. However, as was described in Chapter 6, the motivation would be to utilize a single FOV because of the smaller footprint and therefore greater overlap in the scene being observed by CrIS and AERI. The radiances for each instrument for this scene were presented in Figure 2.1. The scanning angle for the CrIS FOV that is closest to AERI is 14.7° from nadir. While the information content analyses in previous chapters focused on nadir only views from CrIS, changes in scan angle were not found to have much impact on clear sky information content.

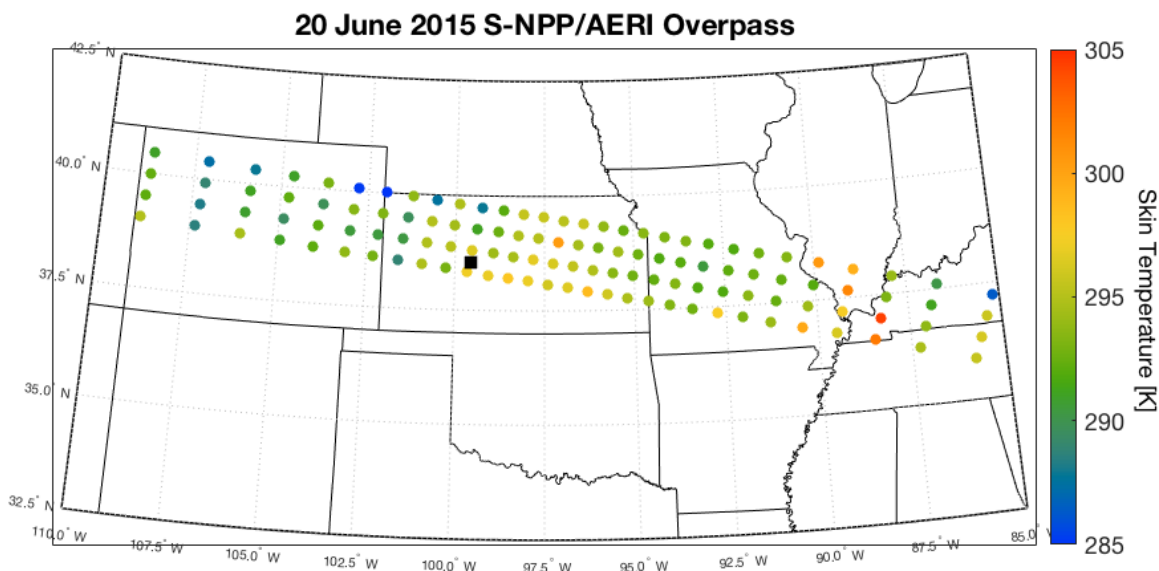


Figure 7.1: Location of AERI (black square) within the S-NPP CrIS granule for the overpass at approximately 830 UTC on 20 June 2015.

7.2 Algorithm Details

While the framework for existing and well-documented retrievals could be modified for a synergistic retrieval, the decision is made to create a new primitive retrieval for this analysis. This is because a retrieval such as AERIOe (Turner and Löhnert 2014) has been tuned to optimize its performance with AERI radiances but has never been used with CrIS. The goal for the primitive retrieval developed here is to present an objective comparison between CrIS and AERI and display the benefits of a synergy of the two sensors in a combined retrieval. It is expected that the retrieval presented here for AERI and CrIS individually should perform notably worse than the existing retrievals (AERIOe and NUCAPS) that utilize their observations because it has not been assessed beyond this single case. Future work will seek to apply lessons learned in tuning the algorithms for individual instruments in order to improve the synergistic algorithm presented here.

We will utilize the Gauss-Newton optimal estimation framework described in Chapter 2 for the retrieval. Recall that the iterative Gauss-Newton optimal estimation equation is described in equation 2.15. The method iterates on the difference between the measured radiance y and the

simulated radiance for the given estimated state vector. As is noted in Chapter 2, Turner and Löhnert (2014) implemented a γ factor to add greater weight to the prior in order to stabilize the model and help it overcome a poor first guess. γ starts out large and gets smaller with each iteration in the retrieval. While Turner and Löhnert (2014) subjectively determined the ideal γ factor was [1000, 300, 100, 50, 30, 10, 3, 1, 1...] for their retrieval, it was found that $\gamma = [5000, 1500, 500, 150, 50, 5, 5...]$ resulted in reasonable results for this case study. The retrieval was found to be very sensitive to γ and would return unphysical solutions if γ was allowed to go to 1. Thus, the retrieval was allowed to converge if $\gamma = 5$ and the retrieval satisfied the convergence criteria described in equation 2.16.

We utilize LBLRTM version 12.6 (Clough et al. 2005) as the forward model for the algorithm. Future versions of the algorithm will seek to implement the OSS fast model, but LBLRTM is used for this case study because of the greater accuracy that it offers. The same trace gas profiles of CO₂, N₂O, CH₄, and O₃ that were used for modelling in the previous chapters are utilized here and are held constant in the retrieval throughout each iteration. In order to highlight the vertical resolution of the AERI near the surface, the vertical grid has a resolution of 25 m near the surface and gradually increases to 500 m resolution at 1500 m AGL. The resolution remains 500 m up to 60,000 m AGL, which is considered top of atmosphere for these calculations. This pattern in resolution is chosen based on results in Chapter 5 and in Blumberg et al. (2015) that suggest AERI's vertical resolution is about 1500 m at 1500 m AGL. The grid ensures that the vertical resolution offered by either AERI or CrIS will not be limited by the vertical grid used for calculations.

The a priori covariance matrix \mathbf{S}_a is calculated from all clear sky profiles at SGP, which were summarized in Table 4.1. This is the same set of radiosondes used to calculate \mathbf{S}_a in Chapter

6 but applied to a different vertical grid in this case. The \mathbf{S}_a matrix used for the retrieval is displayed in Figure 7.2 and has the same general patterns that have been seen in \mathbf{S}_a used for Chapters 5 and 6. The first guess x_a is the mean of all summer SGP clear sky radiosondes. The final solution was not found to be sensitive to whether x_a was calculated with all SGP radiosondes or only summer radiosondes. The decision was made to follow the seasonal first guess used in AERIOe (Turner and Löhnert 2014) for this retrieval as well. As has been done in the information content studies in previous chapters, we use the instrument noise characteristics (from Table 3.1) for the error covariance matrix \mathbf{S}_ϵ .

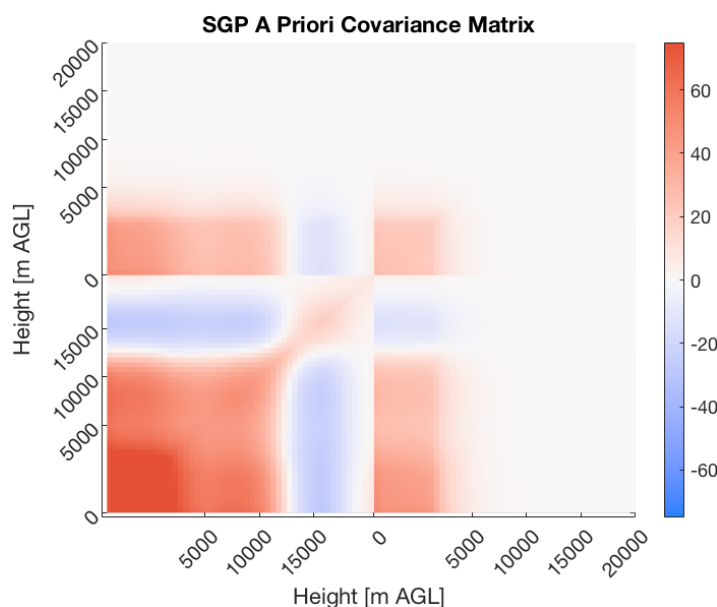


Figure 7.2: A priori covariance matrix used in this analysis. Bottom-left is temperature covaried against itself. Top-right is water vapor varied against itself. Top-left and bottom-right are temperature and water vapor covaried against each other.

7.3 Results

The results of the retrieval for AERI and CrIS alone in addition to the synergy of CrIS+AERI compared to the collocated radiosonde are presented in Figure 7.3. Figure 7.3a displays the results for the temperature retrievals. Each retrieval identifies the presence of a nocturnal inversion, though each retrieval produces inversions of varying degrees of strength

(difference between surface temperature and temperature at the inversion) and varying heights. AERI has the closest comparison to the radiosonde from the surface up to 1000 m AGL and has the best representation of the nocturnal inversion compared to CrIS and CrIS+AERI. For water vapor in Figure 7.3b, AERI produces a solution that is very close to the radiosonde measured profile from the surface up to 1000 m AGL. CrIS and CrIS+AERI detect the small increase in moisture identified by the radiosonde at 1200 m AGL, but it is obvious that signal is spread across several layers. Figure 7.4 displays the same data for the differences calculated between the radiosonde measurement and the retrievals. Figure 7.4a shows that AERI tends to have the better temperature representation in the lowest 1000 m ALG (as was noted with Figure 7.3a). Overall, there is no clear pattern of one sensor having a better comparison across a large layer. Similar is seen for the water vapor differences in Figure 7.4b. Results of the information content analysis in Chapter 5 suggest that CrIS+AERI should converge to the solution of AERI alone near the surface and CrIS alone aloft, with a blend in information between 500 m and 4000 m AGL. Those results also suggest that CrIS+AERI should have the superior retrieval compared to either sensor individually, which is also not the case.

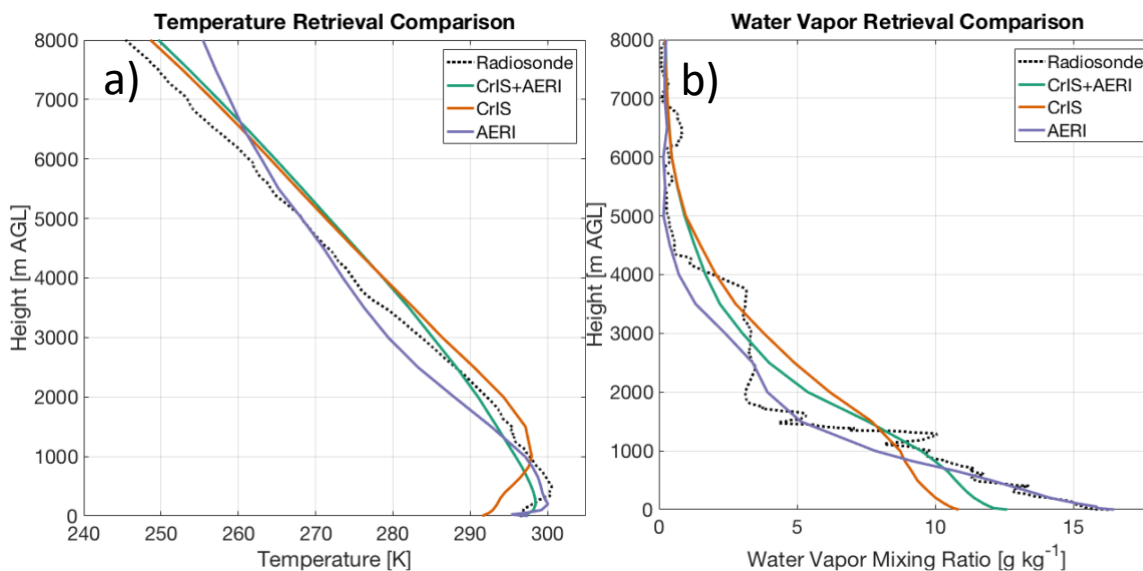


Figure 7.3: Temperature (a) and water vapor (b) comparisons of the AERI (purple), CrIS (orange), and CrIS+AERI (green) retrievals to radiosonde observation (black dotted).

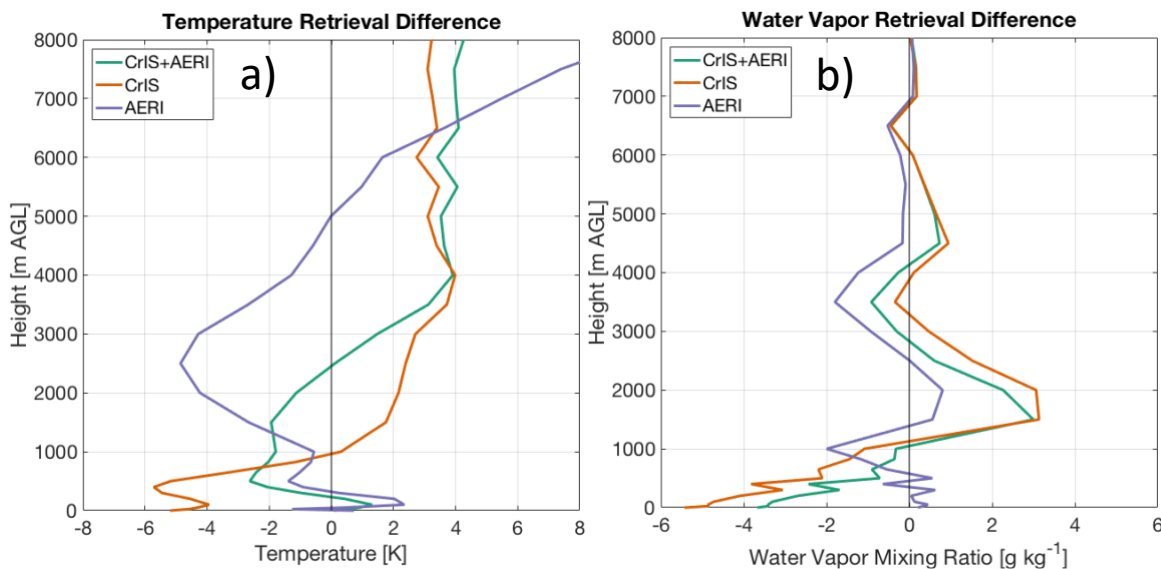


Figure 7.4: Differences in temperature (a) and water vapor (b) between the AERI (purple), CrIS (orange), and CrIS+AERI (green) retrievals to the radiosonde observation. Differences are calculated such that a positive difference indicates the retrieval has greater temperature or water vapor than the radiosonde.

We can compute the vertical resolution of the retrieval by following equation 2.23 again.

However, since γ does not go to 1 in the retrieval, the definition of the averaging kernel is slightly different than what was presented in equation 2.21:

$$\mathbf{A} = (\gamma \mathbf{S}_a^{-1} + \mathbf{K}_i^T \mathbf{S}_\varepsilon^{-1} \mathbf{K}_i)^{-1} (\mathbf{K}_i^T \mathbf{S}_\varepsilon^{-1} \mathbf{K}_i). \quad (7.1)$$

The vertical resolution of the retrievals is shown in Figure 7.5. Here, the pattern is what we would have expected based on the results of the information content study as AERI has greater resolution than CrIS below 1500 m AGL for temperature and 2000 m AGL for water vapor, while CrIS is better than AERI above those heights. The vertical resolution of CrIS+AERI tracks closely to AERI near the surface and is better than both single instrument retrievals from 1000 m AGL up to 5000 m AGL before largely converging with the resolution of CrIS alone. The heights at which AERI has superior vertical resolution compared to CrIS (and vice-versa), and the region where CrIS+AERI is better than either sensor alone very closely match what was identified in the clear sky information content study in Chapter 5. This is an encouraging result, and suggests that a synergy of CrIS+AERI would exceed the 1 km resolution sounding goal set by the Decadal Survey in the lowest 1000 m of the atmosphere.

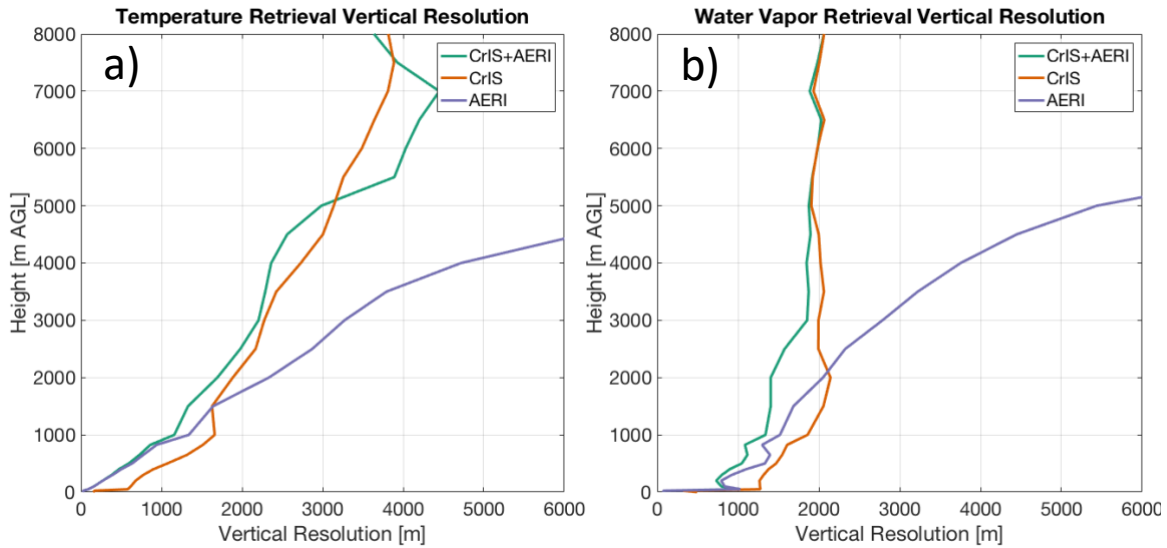


Figure 7.5: Vertical resolution of the temperature (a) and water vapor (b) retrievals. AERI is shown in purple, CrIS in orange, and CrIS+AERI in green.

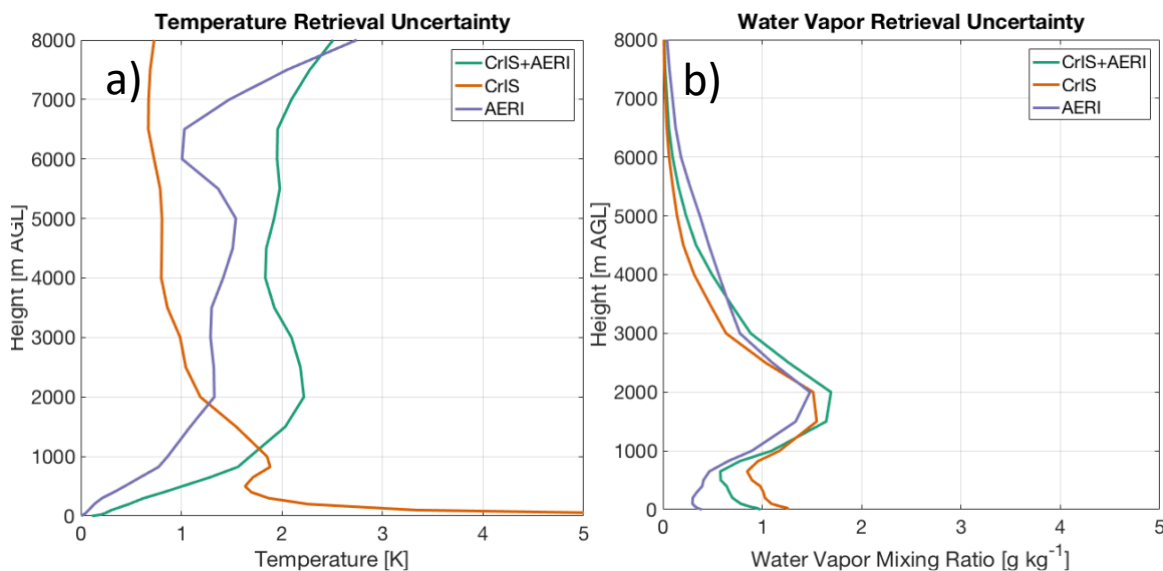


Figure 7.6: 1σ uncertainties of the temperature (a) and water vapor (b) retrievals. AERI is shown in purple, CrIS in orange, and CrIS+AERI in green.

The 1σ uncertainties of each retrieval are presented in Figures 7.6a and 7.6b for temperature and water vapor respectively. AERI alone has the least uncertainty of the three retrievals (for both temperature and water vapor) from the surface up to 2000 m AGL. Above 2000 m AGL, CrIS has the least uncertainty for both temperature and water vapor. CrIS+AERI has the greatest temperature uncertainty of the three retrievals above 1000 m AGL. Instead of the synergy reducing uncertainty (as was expected based on results in Chapter 5), the combination of two sensors has increased uncertainty compared to the individual sensor retrievals when applied to real data. One possible explanation is that the differences in the retrieved state from CrIS and AERI are quite large in comparison to the 1σ uncertainties. For example, in Figure 7.6a it is shown that at 2000 m AGL both CrIS and AERI have a 1σ uncertainty of about 1.25 K. However, as seen in Figure 7.4a, the difference between the temperature retrievals at 2000 m AGL is 6 K. Thus, the synergy of CrIS+AERI is receiving two very different signals from the two sensors that are informing it. This leads to the conclusion that the retrievals are over-constrained: That is the uncertainties are too small. Aires (2011) identified something similar where a synergy of IASI and AMSU-A provided

no improvement because the uncertainty of the IASI instrument was so small that the AMSU-A measurements made no impact on the combined retrieval. One key difference between the result here and the result of the Aires (2011) study is that Aires (2011) did not find that the uncertainties increased in the synergy but rather matched that of IASI alone.

To test if the retrievals are indeed over-constrained, the retrievals are run again with five times greater noise in the error covariance matrix \mathbf{S}_ϵ to assess how increased noise changes the retrievals. These results are displayed in Figure 7.7. First, there is much less variation among the three retrievals, as the first guess has greater influence on the retrievals than in the standard run shown in Figure 7.3. The 1σ uncertainty profiles for the retrievals with five times greater noise are displayed in Figure 7.8. These results are much more in-line with what the information content analysis in Chapter 5 suggested, as CrIS+AERI has the least uncertainty throughout the profile compared to AERI and CrIS alone. While CrIS+AERI does not have the best comparison to the radiosonde here compared to AERI and CrIS alone, the combined retrieval may provide better comparisons to radiosondes than the lone instrument retrievals on average in a large dataset.

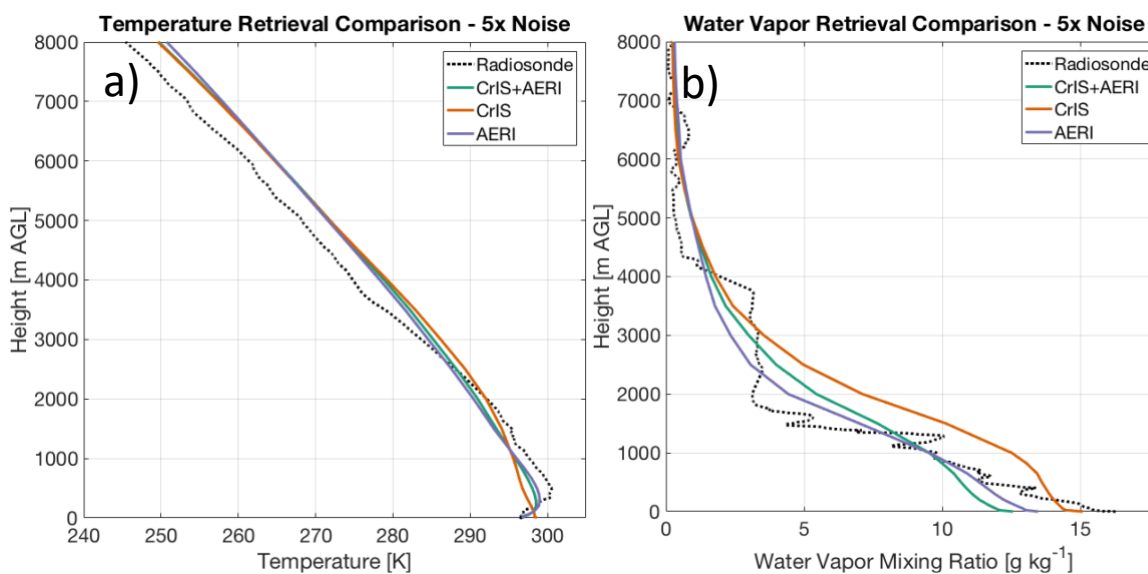


Figure 7.7: As in Figure 7.3 except the retrievals are run with five times greater noise.

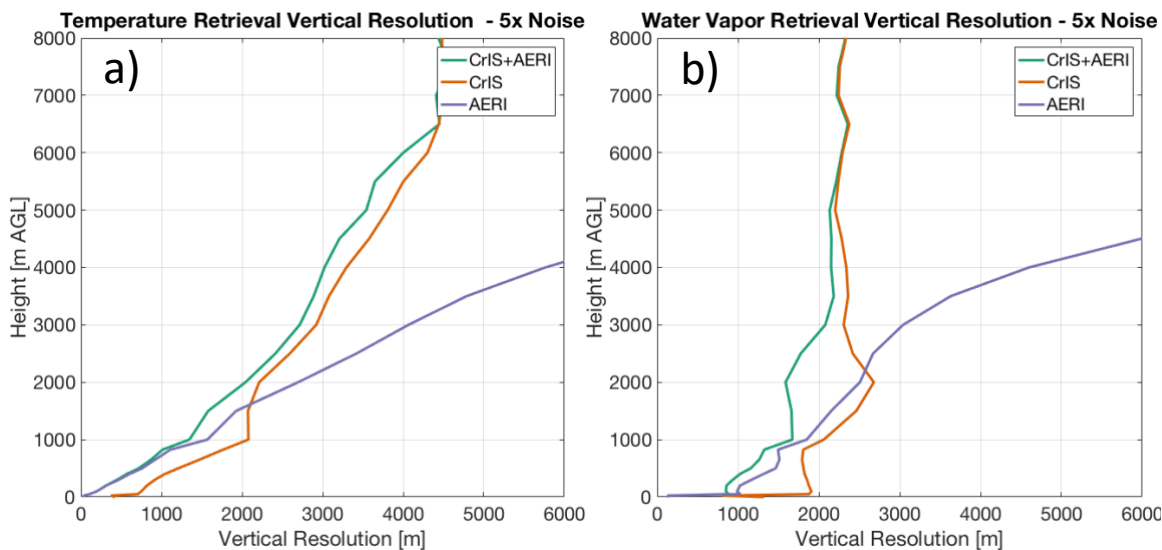


Figure 7.8: As in Figure 7.6 except the retrievals are run with five times greater noise.

Heterogeneity of both the surface and the atmosphere is an unavoidable issue with the matchup between the two sensors and is likely a factor in the conflicting signals from AERI and CrIS in this scene. However, quantifying that influence is difficult. The center of the CrIS FOV is offset by 25 km from the AERI location, thus (given the 7 km radius) AERI is 18 km outside the CrIS FOV. The NUCAPS skin temperature retrievals shown for the CrIS FORs in Figure 7.1 provide some indication on the regional gradients in surface heterogeneity, with adjacent FORs having skin temperature differences around 5 K. Investigating the effects of local heterogeneities on the matchup between the large aerial footprint of the space-based sensor with the AERI is a key piece of future work required to demonstrate the value of the ground-and-space-based synergy.

7.4 Summary and Future Work

In summary, the combined retrieval of CrIS+AERI was not found to have superior comparisons to the radiosonde observation than the lone instrument retrievals from AERI and CrIS. This goes against our expectations, in light of the results of the information content analysis

in Chapter 5. A significant finding however, is that CrIS+AERI offers greater vertical resolution than AERI or CrIS alone throughout the majority of the profile, replicating one of the major findings of the synthetic information content study in Chapter 5. The results suggest CrIS+AERI would exceed the 1 km resolution goal stated by the 2017 Decadal Survey from the surface up to 1000 m AGL. The uncertainties of the CrIS+AERI retrieval did not match expectations given the results of the synthetic information content analysis, as CrIS+AERI had uncertainties greater than the individual instrument retrievals for large layers of the profile. It was shown that this is likely due to the retrievals being over-constrained, as CrIS+AERI provided smaller uncertainties compared to the single instrument retrievals (as was to be expected originally) when they were run with five times greater noise. Therefore, including additional sources of uncertainty in the construction of the error covariance matrix \mathbf{S}_ϵ is important to further develop the combined retrieval. Cimini et al. (2018) provides a framework for assessing model uncertainties (applied to a microwave absorption model) which could potentially be applied to LBLRTM in order to expand the \mathbf{S}_ϵ in physically meaningful ways instead of artificially inflating the uncertainties.

Even with the increased noise resulting in the expected pattern in uncertainty profiles for the three retrievals assessed, CrIS+AERI did not provide the best comparison with the radiosonde observation. Given that the retrieval runs with increased noise resulted in CrIS+AERI reducing uncertainties compared to either instrument individually, it is possible over a larger validation that CrIS+AERI would prove to have better comparisons to radiosonde observations than either instrument operating alone. Future work involves identifying a larger dataset of clear sky matchups between AERI and polar-orbiting sounders and comparing the ground-and-space-based synergy with radiosonde observations.

In general, the retrieval process was found to be quite unstable with low γ and identifying a progression of γ that produced physically reasonable results was only subjectively identified. Carissimo et al. (2005) developed a method to optimize the value of γ in the retrieval, which can be implemented for the combined retrieval presented here moving forward. Additional investigation is necessary to better understand the sources of instability in the retrieval. Increasing the magnitude of the error covariance matrix \mathbf{S}_e is likely to decrease that instability as well.

Lastly, the impact of heterogeneities on the matchup of the AERI and space-based sensor must be further explored. This single case study provides a bit of insight into what may happen to the combined retrieval in regions with a strong temperature gradient. Skin temperature retrievals from NUCAPS using the CrIS FORs found differences of about 5 K in adjacent FORs which are approximately 50 km apart. AERI and the CrIS FOV are offset by 25 km in this case, which may explain the 6 K difference between the single instrument retrievals at 2000 km AGL. These differences in observed scenes for CrIS and AERI may explain the relatively poor comparison between the CrIS+AERI retrieved profile and the radiosonde observations.

Chapter 8: Conclusions and Future Work

8.1 Summary of Results

The analyses presented were designed to advance the understandings of a synergy of ground-based and space-based sounders as a potential solution for improving thermodynamic retrievals in the PBL. We have assessed the synergy between the ground-based AERI with space-based IR sounders, with a particular focus on CrIS, in a clear sky information content study across multiple climate regimes, in Chapter 5. Notably, the improvements in vertical resolution offered by the synergy of CrIS+AERI have been documented, which has been previously understudied. The potential for the ground-based AERI to be a solution to IR sounding in cloudy sky environments was assessed in Chapter 6. Finally, a prototype of the synergistic retrieval between AERI and CrIS was developed and applied to a clear sky case study to determine if the improvements suggested by the clear sky information content study would be replicated in practice.

The clear sky information content study in Chapter 5 found that combining the ground-based AERI with one of the polar-orbiting IR sounders would result in an increase in DOF of 30-40% across the full troposphere as compared to what is offered by the space-based sensor alone. In the surface to 700 hPa layer, including AERI would double the DOF for temperature and offer 1.5 times more DOF for water vapor than what is provided by the polar-orbiting IR sounder alone. The vertical resolution and uncertainty profiles of the synergy of CrIS+AERI converge to AERI alone below 500 m AGL and converge to CrIS above about 4000 m AGL. Between 500 m and 4000 m AGL CrIS+AERI provides better vertical resolution and lesser uncertainties than either

instrument operating alone. CrIS is found to have more information on temperature in moist conditions, and less information on water vapor in moist conditions. Contrastingly, AERI has more information content on water vapor in cold and dry scenes due to its far-IR channels. CrIS+AERI reduces the variability that key retrieval parameters have with respect to PWV, as compared to either sensor individually. This makes the retrieval more consistent, regardless the thermodynamic state.

Chapter 6 assessed the information content of CrIS+AERI in cloudy scenes. It was shown that both AERI and CrIS lose water vapor information as clouds become optically thick, compared to clear sky conditions. It was also found that an optically thick cloud sharpens the Jacobians of both CrIS and AERI, enabling the retrieval of the temperature of the cloud layer. However, CrIS's information becomes limited to above the cloud, and AERI's information becomes limited to below the cloud at high CODs. The hypothesis is confirmed that at high CODs, the synergy of CrIS+AERI converges to the information content of AERI alone below the cloud, and CrIS alone above the cloud. In this regard, the synergy provides a significant improvement compared to what is provided by CrIS alone as the total temperature information increases with increased COD (compared to clear sky conditions) and mitigates the loss of water vapor information that AERI in particular experiences with increased COD. CrIS operating alone in partly cloudy scenes is found to be most sensitive when the aerial cloud fraction is greater than 50%, though the synergy of CrIS+AERI has almost no sensitivity to the aerial cloud fraction. As a whole, introducing AERI to the observing system helps mitigate the loss of information in scenes with opaque clouds because AERI provides the information below the cloud layer that is otherwise lost when using a space-based IR sounder alone.

Chapter 7 developed a synergistic retrieval for CrIS+AERI and applied it to a clear sky case study profile. Somewhat surprisingly, CrIS+AERI had a poor comparison to the collocated radiosonde, versus CrIS or AERI alone. Additionally, the uncertainties suggested that the combination of CrIS+AERI added uncertainty to the retrieval, rather than decreasing the uncertainties as suggested by the clear sky information content study. This is likely a result of the individual instrument uncertainties being too small, as inflating the error covariance matrix to be five times greater produced uncertainty profiles more in line with results from the clear sky information content study. A significant finding was that the vertical resolution of the retrieval replicated that of the information content study, thus suggesting that adding AERI to the observing system would provide soundings that would exceed the Decadal Survey's goal of 1 km resolution in the lowest 1000 m.

8.2 Broader Impacts

8.2.1 Sounding from Geostationary Orbit

The results of this study display the potential benefits of having a sufficient number of dedicated sounding instruments in geostationary orbit to provide nearly continuous global coverage. From the North American perspective, while the broadband channels on the ABI offer some sounding information, it is approximately 3 – 4 times less than that of a high-spectral resolution sounder. GIIRS has only provided observations since 2016 from geostationary orbit so the benefits of such an instrument on NWP and nowcasts may still yet to be fully realized. However, the international satellite community seems to be moving toward IR sounders in geostationary orbit becoming the new normal, with EUMETSAT's IRS instrument set to launch in the near future and NOAA's GEO-XO program suggesting the use of either one or two

geostationary IR sounders to cover North America. Preliminary studies suggest IR sounders in geostationary orbit would be beneficial for NWP (Li et al. 2018, Smith et al. 2020). Given the growing uses of soundings from polar-orbiting platforms (e.g.: Iturbide-Sanchez et al. 2018, Esmaili et al. 2020) it is hard to imagine IR soundings from geostationary orbit not becoming a staple of operational weather forecasting.

The information content and vertical resolution shown in Chapter 5, when combining the ground-based AERI with a space-based IR sounder, suggests the development of a ground-based nationwide network of profilers would provide thermodynamic soundings approaching the uncertainties and vertical resolution desired by the 2017 Decadal Survey, while exceeding those specifications in the lowest 1000 m of the atmosphere. While AERI provides near-continuous monitoring in a single location, the polar-orbiting sounders provide a spatial view of a region once every several hours. A combination of a network of AERIs with the near-constant monitoring offered by a geostationary sounder would provide the high-quality thermodynamic sounding desired by the 2017 Decadal Survey while also providing the temporal component monitoring that the NRC (2009) states is also crucial for improving NWP and nowcasting of high impact weather.

Numerous PBL studies utilizing AERI have proven the benefits of its high-temporal resolution with monitoring convective indices (e.g.: Wagner et al. 2008 and Loveless et al. 2019) or as a source of data assimilation into NWP (e.g.: Coniglio et al. 2019, Hu et al. 2019, Degelia et al. 2020, Lewis et al. 2020). Toporov and Löhnert (2020) have shown that convective indices are significantly more accurate when derived from a synergy of ground-based and space-based sensors instead of a single platform individually. Thermodynamic retrievals provided by a combination of AERI with a geostationary sounder would be expected to be a useful tool for monitoring the timing of convective initiation and better predicting the location of severe convection.

8.2.2 Applications to System Process Studies

In particular, the synergy would be expected to significantly improve the representation of the strength and vertical location of the capping inversion, compared to single-instrument retrievals. With the current polar-orbiting sounding system, the synergy could provide high quality soundings at two distinct time frames between 12 UTC and 00 UTC synoptic radiosonde launches, while the ground-based sensor provides the high-temporal resolution soundings of the PBL. Continuous observations from ground-based platforms could also be important in locations where the overpass times of the polar-orbiting sounders align with the synoptic time radiosonde launches. Understanding how to utilize the data from a polar-orbiting sounder beyond its specific overpass time would be important to maximizing the use of the synergy without a geostationary sounder. In this regard, the constant monitoring of the ABI could supplement the ground-based sensor. These observations could provide validations of PBL transitions for large eddy simulations and system process studies.

Adding the temporal component offered by pairing the ground-based sensor with a geostationary sounder could revolutionize PBL observations. The high-quality soundings at high-temporal resolution would provide observations of the capping inversion breaking before a severe weather event – which would have impacts on mesoscale studies in addition to operational weather forecasting. Better observations of the inversion could lead to an improved understanding on how outflow boundaries and PBL waves (such as bores and solitary waves) result in convective initiation. For example, Loveless et al. (2019) used AERI observations to show that bores will decrease convective inhibition. The physics of bores suggest that the capping inversion gets lifted and weakened, but those observations are difficult to make since

ground-based sensors alone struggle to offer a sufficiently accurate representation of the capping inversion. Therefore, observations of this sort can only be confirmed with well-timed radiosonde launches which require intensive resources and time to make. A nationwide network of ground-based sensors paired with a geostationary sounder would collect observations on numerous cases of these sorts of mesoscale phenomena on an almost daily basis during the convective season.

The heterogeneities of the surface and atmosphere are a caveat to using a synergy of ground-based and space-based sensors to observe mesoscale features. In the example case shown in this dissertation, AERI was 18 km outside the nearest CrIS FOV. If a goal of the ground-based and space-based synergy is to improve observations of mesoscale phenomena like gravity waves, then those horizontal differences in the observed scene become important (that can be the difference between viewing ahead of or behind the feature of interest). Improving the spatial resolution of IR soundings would be needed to minimize the consequences of pairing the point observation of the ground-based sensor with the areal observation of the space-based sensor.

8.3 Future Work

Given that the majority of analyses presented here in addition to those by Ebell et al. (2013) and Toporov and Löhnert (2020) have made progress in demonstrating the benefits of the ground-and-space-based synergy in ideal/synthetic settings, a major piece of future work to prove the viability of the ground-and-space-based synergy would be to automate the retrieval so that it can both process a large set of profiles from prior data for process studies as well as run daily in near real-time in order to contemporaneous retrievals for NWP assimilation and operational decision support. This would enable expansive validation of the retrieval in order to confirm (or deny) the benefits that have been found in synthetic studies. Chapter 7 showed however, that finding

additional sources of uncertainty to include in the error covariance matrix is necessary to prevent the retrieval from becoming over-constrained. A neural network, as was used by Toporov and Löhnert (2020), could also prove to be a beneficial method for retrieving the atmospheric state from a single instrument or a synergy of multiple instruments.

Supplementing space-based sounders with ground-based sensors would limit improvements in thermodynamic sounding to over land only. However, results from both Kwon et al. (2012) and Sun et al. (2017) suggest that retrieval errors are greatest over land, so this would present a solution to the locations and scenarios with greatest errors. The land surface presents a heterogeneous FOV for the satellite sensor based on the local variations in skin temperature and surface emissivity. Future work is necessary to address how the heterogeneous FOV of the space-based sensor affects the matchup with the point observations from a ground-based sensor. A future study could make use of the SeeBor dataset (Borbas et al. 2005) to better understand the effects that variable skin temperature and surface emissivity over land have on the uncertainties of space-based sensors and how that may affect the space-based/ground-based synergy. Large eddy simulations could also provide synthetic data for such a study. The LAFe campaign (Wulfmeyer et al. 2018) had numerous AERIs within 50 km spacing and could provide a dataset with multiple AERI observations within a single FOV and in adjacent FOVs of a space-based sounder.

As has been noted earlier in this dissertation, cloudy sky environments present a complex problem for IR sounding given the computations necessary for simulating cloudy sky IR radiances. However, as shown in Chapter 5, these sensors provide information in cloudy sky environments, especially when united in a synergy. In fact, these sensors could provide more temperature information in certain cloudy scenes than in clear sky scenes. The development of fast models (e.g.: Martinazzo et al. 2021) to simulate cloudy sky radiances may make IR sounding in cloudy

sky scenes more practical via direct simulation of the cloud instead of removing the signal of the cloud from the measurement (as cloud-clearing does). Given the frequency of cloudy sky scenes (Wylie and Menzel 1999), it is important to find ways to make use of these observations in cloudy sky environments because impactful weather tends to happen in cloudy sky environments.

Lastly, funding the development of a ground-based network of profilers presents a large obstacle. For example, the per unit cost of the current generation of AERIs is approximately \$400,000. While mass manufacturing could lower the price per instrument while future simplified designs could also lower the unit cost substantially, a very large infrastructure investment from federal and state governments and their partners would be necessary to fund such a network. Additionally, questions remain on the density of sensors required to exploit the benefits of such a network. The NRC (2009) suggested about 400 profiling sites across the United States with approximately 150 km spacing (for reference, there are about 140 WSR-88D radars in the continental United States). Assessments of the cost-benefits of each sensor to NWP and nowcasting efforts by local weather forecasting offices would likely be the preferred analysis of the federal government to identify the ideal density of such a network. The New York Mesonet (Shrestha et al. 2021) consists of 17 different profiling sites across the state and provides daily examples of the benefits of an operational profiling network on a smaller scale. The assimilation of retrievals from AERIs deployed at the ARM SGP site in Oklahoma have been shown to improve local convective forecasts (Lewis et al. 2020). Lastly, the PECAN (Geerts et al. 2017) campaign also featured observations from a combination of 6 fixed profiling sites and 5 mobile profiling sites throughout the Central Plains in the summer of 2015 which have been used to assess the benefits of a ground-based profiling network on NWP (e.g.: Coniglio et al. 2019, Hu et al. 2019, Degelia et al. 2020). While small networks of ground-based sensors have been proven to benefit

local short-term (less than 24 hours) forecasts, observation system simulation experiments (OSSE) are necessary to quantify the benefits of larger theoretical networks of profilers. As has been discussed above, a synergy of ground-and-space-based sensors would provide improved monitoring of convective indices, most importantly between synoptic time radiosonde launches. These observations should be able to improve nowcasting abilities to identify regions with instability to support severe convection and the timing of when that convection would occur.

References

- Ackerman, S. A., R. E. Holz, R. Frey, E. W. Eloranta, B. C. Maddux, M. McGill, 2008: Cloud detection with MODIS. Part II: Validation. *J. Atmos. Oceanic Technol.*, **25**, 1073-1086, doi: 10.1175/2007JTECHA1053.1.
- Aires, F., 2011: Measure and exploitation of multisensor and multi-wavelength synergy for remote sensing: 1. Theoretical considerations, *J. Geophys. Res.*, **116**, D02301, doi:10.1029/2010JD014701.
- _____, O. Aznay, C. Progent, M. Paul, and F. Bernardo, 2012: Synergistic multi-wavelength remote sensing versus a posteriori combination of retrieved products: Application for the retrieval of atmospheric profiles using MetOp-A. *J. Geophys. Res.*, **117**, D18304, doi:10.1029/2011JD017188.
- Bianchini, G., L. Palchetti, G. Muscari, I. Fiorucci, P. Di Girolamo, and T. Di Iorio, 2011: Water vapor sounding with the far infrared REFIR-PAD spectroradiometer from a high-altitude ground-based station during the ECOWAR campaign. *Geo. Phys. Res.*, **116**, D02310, doi:10.1029/2010JD014530.
- Bloch, C., R. O. Knuteson, A. Gambacorta, N. R. Nalli, J. Gartzke, and L. Zhou, 2019: Near-real-time surface-based CAPE from merged hyperspectral IR satellite sounder and surface meteorological station data. *J. Appl. Meteor. Climatol.*, **58**, 1613-1632, doi:10.1175/JAMC-D-18-0155.1.
- Blumberg, W. G., D. D. Turner, U. Löhnert, and S. Castleberry, 2015: Ground-based temperature and humidity profiling using spectral infrared and microwave observations. Part II: Actual retrieval performance in clear-sky and cloudy conditions. *J. Appl. Meteor. and Climatol.*, **54**, 2305-2319, doi:10.1175/JAMC-D-15-005.1.
- _____, K. T. Halbert, T. A. Supinie, P. T. Marsh, R. L. Thompson, and J. A. Hart, 2017: SHARPPy: An open-source sounding analysis toolkit for the atmospheric sciences. *Bull. Amer. Meteor. Soc.*, **98**, 1625-1636, doi:10.1175/BAMS-D-15-00309.1.
- Borbas, E. E., S. W. Seemann, H. Huang, J. Li, and W. P. Menzel, 2005: Global profile training database for satellite regression retrievals with estimates of skin temperature and emissivity. Proceedings of the XIV. International ATOVS Study Conference, Beijing, China, University of Wisconsin-Madison, Space Science and Engineering Center, Cooperative Institute for Meteorological Satellite Studies (CIMSS), Madison, WI, pp. 763-770.
- _____, G. Hulley, M. Feltz, R. Knuteson, and S. Hook, 2018: The Combined ASTER MODIS Emissivity over Land (CAMEL) part 1: Methodology and high spectral resolution application. *Remote Sens.*, **10**, 643, doi:10.3390/rs10040643.

- Carissimo, A., I. De Feis, and C. Serio, 2005: The physical retrieval methodology for IASI: The d-IASI code. *Environ. Model. Software*, **20**, 1111–1126, doi:10.1016/j.envsoft.2004.07.003.
- Chahine, M. T., 1974: Remote sounding of cloudy atmospheres. I. The single cloud layer. *J. Atmos. Sci.*, **31**, 233-243, doi: 10.1175/1520-0469(1974)031<0233:RSOCAI>2.0.CO;2.
- _____, and Coauthors, 2006: AIRS: Improving weather forecasting and providing new data on greenhouse gases. *Bull. Amer. Meteor. Soc.*, **87**, 911-926, doi:10.1175/BAMS-D-87-7-911.
- Chen, S.-Y., C.-Y. Liu, C.-Y. Huang, C.-C. Hsu, H.-W. Li, P.-H. Lin, J.-P. Cheng, and C.-Y. Huang, 2021: An analysis of FORMOSAT-7/COSMIC-2 radio occultation data in the troposphere. *Remote Sensing*, **13**, 717, doi:10.3390/rs13040717.
- Cimini, D., P. W. Rosenkranz, M. Y. Tretyakov, M. A. Koshelev, and F. Romano, 2018: Uncertainty of atmospheric microwave absorption model: Impact on ground-based radiometer simulations and retrievals. *Atmos. Chem. Phys.*, **18**, 15231-15259, doi:10.5194/acp-18-15231-2018.
- Clough, S. A., M. J. Iacono, and J. L. Moncet, 1992: Line-by-line calculations of atmospheric fluxes and cooling rates: Application to water vapor. *J. Geophys. Res.*, **97**, 15761-15785, doi: 10.1029/92JD01419.
- _____, and M. J. Iacono, 1995: Line-by-line calculations of atmospheric fluxes and cooling rates. 2: Application to carbon dioxide, ozone, methane, nitrous oxide, and halocarbons. *J. Geophys. Res.*, **100**, 16519-16535, doi:10.1029/95/JD01386.
- _____, M. W. Shepard, E. J. Mlawer, J. S. Delamere, M. J. Iacono, K. Cady-Pereira, S. Boukabara, and P. D. Brown, 2005: A summary of the AER codes. *J. Quant. Spectrosc. Radiat. Transfer*, **91**, 233-244, doi:10.1016/j.jqsrt.2004.05.058.
- Coniglio, M.C., G.S. Romine, D.D. Turner, and R.D. Torn, 2019: Impacts of targeted AERI and Doppler lidar wind retrievals on short-term forecasts of the initiation and early evolution of thunderstorms. *Month. Wea. Rev.*, **147**, 1149-1170, doi:10.1175/MWR-D-18-0351.1
- Conrath, B. J., R. A. Hanel, V. G. Kunde, and C. Prabhakara, 1970: The infrared interferometer experiment on Numbus 3. *J. Geophys. Res.*, **75**, 5831-5857, doi:10.1029/JC075i030p05831.
- Degelia, S.K., X. Wang, D.J. Stensrud, and D.D. Turner, 2020: Systematic evaluation of the impact of assimilating a network of ground-based remote sensing profilers for forecasts of nocturnal convection initiation during PECAN. *Mon. Wea. Rev.*, **148**, 4703-4728, doi:10.1175/MWR-D-20-0118.1.

- Dong, X., B. Xi, A. Kennedy, P. Minnis, and R. Wood, 2014: A 19-month record of marine aerosol-cloud-radiation properties derived from DOE ARM mobile facility deployment at the Azores. Part I: Cloud fraction and single-layered MBL cloud properties. *J. Clim.*, **27**, 3665–3682, doi:10.1175/JCLI-D-13-00553.1.
- Ebell, K., E. Orlandi, A. Hünerbein, U. Löhnert, and S. Crewell, 2013: Combining ground-based with satellite-based measurements in the atmospheric state retrieval: Assessment of the information content. *J. Geophys. Res. Atmos.*, **118**, 6940–6956, doi:10.1002/jgrd.50548.
- Elwell, J. D., and Coauthors, 2006: A Geosynchronous Imaging Fourier Transform Spectrometer (GIFTS) for hyperspectral atmospheric remote sensing: Instrument overview and preliminary performance results. *Space Dynamics Lab Publications*, Paper 36, Available at: https://digitalcommons.usu.edu/cgi/viewcontent.cgi?article=1035&context=sdl_pubs.
- Esmaili, R. B., and Coauthors, 2020: Adapting satellite soundings for operational forecasting within the Hazardous Weather Testbed. *Remote Sens.*, **12**, 886, doi:10.3390/rs12050886.
- Feltz, W. F., and J. R. Mecikalski, 2002: Monitoring high-temporal-resolution convective stability indices using the ground-based Atmospheric Emitted Radiance Interferometer (AERI) during the 3 May 1999 Oklahoma–Kansas tornado outbreak. *Wea. Forecasting*, **17**, 445–455, doi:10.1175/1520-0434(2002)017<0445:MHTRCS>2.0.CO;2.
- _____, W. L. Smith, H. B. Howell, R. O. Knuteson, H. Woolf, and H. E. Revercomb, 2003: Near-continuous profiling of temperature, moisture, and atmospheric stability using the Atmospheric Emitted Radiance Interferometer (AERI). *J. Appl. Meteor.*, **42**, 584–597, doi:10.1175/1520-0450(2003)042<0584:NPOTMA>2.0.CO;2.
- Gambacorta, A., 2013: The NOAA unique CrIS/ATMS processing system (NUCAPS). Algorithm theoretical basis documentation. Version 1.0, NOAA, Silver Spring, MD, p. 73 Available at: https://www.ospo.noaa.gov/Products/atmosphere/soundings/nucaps/docs/NUCAPS_ATBD_20130821.pdf.
- Gartzke, J., R. Knuteson, G. Przybyl, S. Ackerman, and H. Revercomb, 2017: Comparison of satellite-, model-, and radiosonde-derived convective available potential energy in the Southern Great Plains region. *J. Appl. Meteor. Climatol.*, **56**, 1499–1513, doi:10.1175/JAMC-D-16-0267.1.
- Geerts, B., and Coauthors, 2017: The 2015 Plains Elevated Convection At Night field project. *Bull. Amer. Meteor. Soc.*, **98**, 767–786, doi: 10.1175/BAMS-D-15-00257.1.
- Han, Y. and Coauthors, 2013: Suomi NPP CrIS measurements, sensor data record algorithm, calibration and validation activities and record data quality. *J. Geophys. Res. Atmos.*, **118**, 12734–12748, doi:10.1002/2013JD020344.
- _____, and Coauthors, 2018: Joint Polar Satellite System (JPSS) Cross Track Infrared Sounder (CrIS) Sensor Data Records (SDR) Algorithm Theoretical Basis Document (ATBD) for

- normal spectral resolution. *National Oceanic and Atmospheric Administration Center for Satellite Applications and Research*, version 1.0.1, Available at: https://www.star.nesdis.noaa.gov/jpss/documents/ATBD/D0001-M01-S01-002_JPSS_ATBD_CRIS-SDR_nsr_20180614.pdf.
- Hewison, T. J., 2007: 1D-VAR retrieval of temperature and humidity profiles from a ground-based microwave radiometer. *IEEE Trans. Geosci. Remote Sens.*, **45**, 2163-2168, doi:10.1109/TGRS.2007.898091.
- Hillger, D., T. Kopp, T. Lee, D. Lindsey, C. Seaman, S. Miller, J. Solbrig, S. Kidder, S. Bachmeier, T. Jasmin, and T. Rink, 2013: First light imagery from Suomi NPP VIIRS. *Bull. Amer. Meteor. Soc.*, **94**, 1019-1029, doi: 10.1175/BAMS-D-12-00097.1.
- Hilton, F., and Coauthors, 2012: Hyperspectral earth observation from IASI: Five years of accomplishments. *Bull. Amer. Meteor. Soc.*, **93**, 347-370, doi:10.1175/BAMS-D-11-00027.1.
- Ho, S., W. L. Smith, H. Huang, 2002: Retrieval of atmospheric-temperature and water-vapor profiles by use of combined satellite and ground-based infrared spectral-radiance measurements. *J. Appl. Opt.*, **41**, 4057-4069, doi:10.1364/AO.41.004057.
- Hoff, R. M., and R. M. Hardesty, Eds., 2012: Thermodynamic Profiling Technologies Workshop Report to the National Science Foundation and the National Weather Service. NCAR Tech. Note. NCAR/TN-488+STR, 88 pp.
- Hu, J., N. Yussouf, D.D. Turner, T.A. Jones, and X. Wang, 2019: Impact of ground-based remote sensing boundary layer observation on short-term probabilistic forecasts of a tornadic supercell event. *Wea. Forecasting*, **34**, 1453-1476, doi:10.1175/WAF-D-18-0200.1
- Iturbide-Sanchez, F., S. R. Santos da Silva, Q. Liu, K. Pryor, M. E. Pettey, and N. R. Nalli, 2018: Toward the operational weather forecasting application of atmospheric stability products derived from NUCAPS CrIS/ATMS soundings. *IEEE Trans. Geosci. Remote Sens.*, **56**, 4522-4545, doi:10.1109/TGRS.2018.2824829.
- Kaplan, L. D., 1959: Inference of atmospheric structure from remote radiation measurements. *J. Opt. Soc. Am.*, **49**, 1004-1007, doi:10.1364/JOSA.49.001004.
- _____, M. T. Chahine, J. Sussking, and J. E. Searl, 1977: Spectral band passes for a high precision satellite sounder. *Appl. Optics*, **16**, 322-325, doi: 10.1364/AO.16.000322.
- Kelly, G. A. M., G. A. Mills, and W. L. Smith, 1978: Impact of Nimbus-6 temperature soundings on Australian region forecasts. *Bull. Amer. Meteor. Soc.*, **59**, 393-405, doi:10.1175/1520-0477-59.4.393.

- Knuteson, R. O., and Coauthors, 2004a: The Atmospheric Emitted Radiance Interferometer. Part I: Instrument design. *J. Atmos. Oceanic Technol.*, **21**, 1763-1776, doi:10.1175/JTECH-1662.1.
- _____ and Coauthors, 2004b: The Atmospheric Emitted Radiance Interferometer. Part II: Instrument performance. *J. Atmos. Oceanic Technol.*, **21**, 1777-1789, doi:10.1175/JTECH-1663.1.
- Klein, P., and Coauthors, 2015: LABEL: A multi-institutional, student-led, atmospheric boundary layer experiment. *Bull. Amer. Meteor. Soc.*, **96**, 1743-1764, doi:10.1175/BAMS-D-13-00267.1.
- Kuo, Y. H., T. K. Wee, S. Sokolovskiy, C. Rocken, W. Schreiner, D. Hunt, and R. A. Anthes, Inversion and error estimation of GPS radio occultation data. *J. Meteor. Soc. Japan*, **82**, 507-531, doi:10.2151/jmsj.2004.507.
- Kwon, E., B. J. Sohn, W. L. Smith, and J. Li, 2012: Validating IASI temperature and moisture sounding retrievals over East Asia using radiosonde observations. *J. Atmos. Oceanic Technol.*, **29**, 1250-1262, doi: 10.1175/JTECH-D-11-0078.1.
- Langland, R. H., and N. L. Baker, 2004: Estimation of observation impact using the NRL atmospheric variational data assimilation adjoint system. *Tellus*, **56**, 189-201, doi:10.3402/tellusa.v56i3.14413.
- LaRoche, S., and R. Sarrazin, 2010: Impact study with observations assimilated over North America and the North Pacific Ocean on the MSC global forecast system. Part I: Contribution of radiosonde, aircraft, and satellite data. *Atmos. Ocean*, **48**, 10-25, doi:10.3137/AO1006.2010.
- Lewis, W. E., T. J. Wagner, J. A. Otkin, and T. A. Jones, 2020: Impact of AERI temperature and moisture retrievals on the simulation of a Central Plains severe convective weather event. *Atmosphere*, **11**, 729, doi: 10.3390/atmos11070729.
- Le Marshall, and Coauthors, 2006: Advanced Infrared Sounder (AIRS) observations improve global analysis and forecast capability. *Bull. Amer. Meteor. Soc.*, **87**, 891-894, doi:10.1175/BAMS-87-7-891.
- Li, J., C. Y. Li, H. L. Huang, T. J. Schmidt, X. Wu, W. P. Menzel, and J. J. Gurka, 2005: Optimal cloud-clearing for AIRS radiances using MODIS. *IEEE T. Geosci. Remote*, **43**, 1266-1278, doi: 10.1109/TGRS/2005.847795.
- Li, Z., J. Li, P. Wang, A. Lim, J. Li, T. J. Schmit, R. Atlas, S. Boukabara, and R. N. Hoffman, 2018: Value-added impact of geostationary hyperspectral infrared sounders on local severe storm forecasts – via a quick regional OSSE. *Adv. Atmos. Sci.*, **35**, 1217-1230, doi:10.1007/s00376-018-8036-3.

- Löhnert, U., D. D. Turner, and S. Crewell, 2009: Ground-based temperature and humidity profiling using spectral infrared and microwave observations. Part I: Simulated retrieval performance in clear-sky conditions. *J. Appl. Meteor. Climatol.*, **48**, 1017-1032, doi:10.1175/2008JAMC2060.1.
- Loveless, D. M., T. J. Wagner, D. D. Turner, S. A. Ackerman, and W. F. Feltz, 2019: A composite perspective on bore passages during the PECAN campaign. *Mon. Wea. Rev.*, **147**, 1395-1413, doi:10.1175/MWR-D-18-0291.1.
- Loveless, M., E. E. Borbas, R. Knuteson, K. Cawse-Nicholson, G. Hulley, and S. Hook, 2021: Climatology of the Combined ASTER MODIS Emissivity over Land (CAMEL) version 2. *Remote Sens.*, **13**, 111, doi:10.3390/rs13010111.
- Martinazzo, M., D. Magurno, W. Cossich, C. Serio, G. Masiello, and T. Maestri, 2021: Assessment of the accuracy of scaling methods for radiance simulations at far and mid infrared wavelengths. *J. Quant. Spectrosc. Ra.*, **271**, 107739, doi: 10.1016/j.jqsrt.2021.107739.
- Masiello, G., C. Serio, and P. Antonelli, 2012: Inversion for atmospheric thermodynamical parameters of IASI data in the principal components space. *Quart. J. Roy. Meteor. Soc.*, **138**, 103–117, doi:10.1002/qj.909.
- McClatchey, R. A., 1972: *Optical Properties of the Atmosphere*. Air Force Cambridge Research Laboratories, 3rd Edition, Air Force Systems Command, United States Air Force, 108 pp.
- McNally, A. P., 2002: A note on the occurrence of cloud in meteorologically sensitive areas and the implications for advanced infrared sounders. *Quart. J. Roy. Meteor. Soc.*, **128**, 2551-2556, doi:10.1256/qj.01/206.
- _____, 2009: The direct assimilation of cloud-affected satellite infrared radiances in the ECMWF 4D-Var. *Quart. J. Royal Meteor. Soc.*, **135**, 1214-1229, doi:10.1002/qj.426.
- Menzel, W. P., T. J. Schmit, P. Zhang, and J. Li, 2018: Satellite-based atmospheric infrared sounder development and applications. *Bull. Amer. Meteor. Soc.*, **99**, 583-603, doi: 10.1175/BAMS-D-16-0293.1.
- Mlawer, E. J., and D. D. Turner, 2016: Spectral radiation measurements and analysis in the ARM program. *The Atmospheric Radiation Measurements Program: The First 20 Years, Meteor. Monogr.*, No. 57, Amer. Meteor. Soc., 14.1-14.17, doi:10.1175/AMSMONOGRAPHS-D-15-0027.1.
- Moncet, J., G. Uymin, A. E. Lipton, and H. E. Snell, 2008: Infrared radiance modeling by optimal spectral sampling. *J. Atmos. Sci.*, **65**, 3917-3934, doi:10.1175/2008JAS2711.1.

- _____, G. Uymin, P. Liang, and A. E. Lipton, 2015: Fast and accurate radiative transfer in the thermal regime by simultaneous optimal spectral sampling over all channels. *J. Atmos. Sci.*, **72**, 2622-2641, doi:10.1175/JAS-D-14-0190.1.
- Nalli, N. R., and Coauthors, 2018: Validation of atmospheric profile retrievals from the SNPP NOAA-unique combined atmospheric processing system. Part I: Temperature and moisture. *IEEE Trans. Geosci. and Remote Sens.*, **56**, 180-190, doi:10.1109/TGRS.2017.2744558.
- National Academies of Sciences, Engineering, and Medicine, 2018: *Thriving on Our Changing Planet: A Decadal Strategy for Earth Observation from Space*. National Academies Press, 716, pp. doi:0.17226/24938.
- National Research Council, 2009: *Committee on Developing Mesoscale Meteorological Observational Capabilities to Meet Multiple National Needs*. National Academies Press, 234 pp, ISBN:978-0-309-12986-2.
- Ohring, G., 1979: Impact of satellite temperature sounding data on weather forecasts. *Bull. Amer. Meteor. Soc.*, **60**, 1142-1147, doi:10.1175/1520-0477(1979)060<1142:IOSTDS>2.0.CO;2.
- Pagano, T. S., S. Broberg, H. H. Aumann, D. Elliott, E. Manning, and L. Strow, 2014: Performance status of the atmospheric infrared sounder ten years after launch. NASA-JPL, Pasadena, CA, p. 9, (available: https://trs.jpl.nasa.gov/bitstream/handle/2014/42928/12-5086_A1b.pdf).
- N. Phillips, L. McMillin, A Gruber, and D. Wark, 1979: An evaluation of early operational temperature soundings from TIROS-N. *Bull. Amer. Meteor. Soc.*, **60**, 1188-1197, doi: 10.1175/1520-0477-60.10.1177.
- Revercomb, H. E. and L. Strow, 2020: S-NPP CrIS IMG: Collocated VIIRS level 1 / cloud mask statistical summary V2, Greenbelt, MD, Goddard Earth Sciences Data and Information Services Center (GES DISC), doi: 10.5067/NC505NHFIHCY.
- Rodgers, C. D., 2000: *Inverse Methods for Atmospheric Sounding: Theory and Practice*. Series on Atmospheric, Oceanic, and Planetary Physics, Vol. 2, World Scientific, 238 pp.
- Rothman, L. S., and Coauthors, 2003: The HITRAN molecular spectroscopic database: Edition of 2000 including updates through 2001. *J. Quant. Spectrosc. Ra.*, **82**, 5-44, doi:10.1016/S0022-4073.
- Schmit, T. J., P. Griffith, M. M. Gunshor, J. M. Daniels, S. J. Goodman, and W. J. Lebair, 2017: A closer look at the ABI on the GOES-R series. *Bull. Amer. Meteor. Soc.*, **98**, 681-698, doi:10.1175/BAMS-D-15-00230.1.

- Shrestha, B., J. Brotzge, J. Wang, C. Thorncroft, N. Bain, and S. Perez, 2021: The New York state mesonet profiler network. *25th Conference on Integrated Observing and Assimilation Systems for the Atmosphere, Oceans, and Land Surface*, New Orleans, LA, Amer. Meteor. Soc., 13.2, <https://ams.confex.com/ams/101ANNUAL/meetingapp.cgi/Paper/382410>.
- Sisterton, D. L., R. A. Peppler, T. S. Cressm P. J. Lamb, and D. D. Turner, 2016: The ARM Southern Great Plains (SGP) site. *The First 20 Years, Meteor. Monogr.*, No. 57, Amer. Meteor. Soc., 6.1-6.14, doi:10.1175/AMSMONOGRAPHS-D-16-0004.1.
- Smith, N. and C. D. Barnet, 2020: CLIMCAPS observing capability for temperature, moisture and trace gases from AIRS/AMSU and CrIS/ATMS. *Atmos. Measur. Techn.*, **71**, 1-33, doi:10.5194/amt-2020-71.
- Smith, W. L., 1967: Profiles from satellite radiation measurements. *Mon. Wea. Rev.*, **95**, 363-369, doi:10.1175/1520-0493(1967)095<0363:AIMFDT>2.3.CO;2.
- _____, H. M. Woolf, C. M. Hayden, D. Q. Wark, and L. M. McMillin, 1979: The TIROS-N Operational Vertical Sounder, *Bull. Amer. Meteor. Soc.*, **60**, 1177-1187, doi: 10.1175/1520-0477-60.10.1177.
- _____, and Coauthors, 1981: First sounding results from VAS-D. *Bull. Amer. Meteor. Soc.*, **62**, 232-236, doi: 10.1175/1520-0477-62.2.232.
- _____, G. W. Wade, and H. M. Woolf, 1985: Combined atmospheric sounding/cloud imagery – A new forecasting tool. *Bull. Amer. Meteor. Soc.*, **66**, 138-141, doi: 10.1175/1520-0477(1985)066<0138:CASINF>2.0.CO;2.
- _____, 1991: Atmospheric soundings from satellites – false expectation or the key to improved weather prediction? *Quart. J. Roy. Meteor. Soc.*, **117**, 267-297, doi:10.1002/qj.49711749802.
- _____, Q. Zhang, M. Shao, and E. Weisz, 2020: Improved severe weather forecasts using LEO and GEO satellite soundings. *J. Atmos. Oceanic Technol.*, **37**, 1203-1218, doi:10.1175/JTECH-D-19-0158.1.
- _____, H. Revercomb, E. Weisz, D. Tobin, R. Knuteson, J. Taylor, and W. P. Menzel, 2021: Hyperspectral satellite radiance atmospheric profile information content and its dependence on spectrometer technology. *IEEE J. Sel. Top. Appl. Earth Observ.*, **14**, 4720-4736, doi:10.1109/JSTARS.2021.3073482.
- Stephens, G., and Coauthors, 2018: CloudSat and CALIPSO within the A-Train: Ten years of actively observing the Earth system. *Bull. Amer. Meteor. Soc.*, **99**, 569-581, doi:10.1175/BAMS-D-16-0324.1.

- Sun, B., A. Reale, F. H. Tilley, M. E. Pettey, N. R. Nalli, and C. D. Barnet, 2017: Assessment of NUCAPS S-NPP CrIS/ATMS sounding products using reference and conventional radiosonde observations. *IEEE J. Sel. Top. Appl. Earth Observ.*, **10**, 2499-2509, doi:10.1109/JSTARS.2017/2670504.
- Susskind, J., C. D. Barnet, and J. M. Blaisdell, 2003: Retrieval of atmospheric and surface parameters from AIRS/AMSU/HSB data in the presence of clouds. *IEEE T Geosci. Remote*, **41**, 390-409, doi: 10.1109/TGRS.2002.808236.
- Tanamachi, R. L., W. F. Feltz, and M. Xue, 2008: Observations and numerical simulation of upper boundary layer rapid drying and moistening events during the International H₂O Project (IHOP_2002). *Mon. Wea. Rev.*, **136**, 3106-3120, doi:10.1175/2008MWR2204.1.
- Toporov, M., and U. Löhnert, 2020: Synergy of satellite- and ground-based observations for continuous monitoring of atmospheric stability, liquid water path, and integrated water vapor: Theoretical evaluations using reanalysis and neural networks. *J. Appl. Meteor. and Climatol.*, **59**, 1153-1170, doi:10.1175/JAMC-D-19-0169.1.
- Turner, D. D., S. A. Ackerman, B. A. Baum, H. E. Revercomb, and P. Yang, 2003: Cloud phase determination using ground-based AERI observations at SHEBA. *J. Appl. Meteor.*, **42**, 701-715, doi:10.1175/1520-0450(2003)042<0701:CPDUGA>2.0.CO;2.
- _____, 2005: Arctic mixed-phase cloud properties from AERI-lidar observations: Algorithm and results from SHEBA. *J. Appl. Meteor.*, **44**, 427-444, doi:10.1175/JAM2208.1.
- _____, and U. Löhnert, 2014: Information content and uncertainties in thermodynamic profiles and liquid cloud properties retrieved from the ground-based Atmospheric Emitted Radiance Interferometer (AERI). *J. Appl Meteor. Climatol.*, **53**, 752-771, doi:10.1175/JAMC-D-13-0126.1.
- _____, J. Mlawer, and H. E. Revercomb, 2016: Water vapor observations in the ARM program. *The First 20 Years, Meteor. Monogr.*, No. 57, Amer. Meteor. Soc., 13.1-13.18, doi: 10.1175/AMSMONOGRAPHS-D-15-0025.1.
- _____, and W. G. Blumberg, 2019: Improvements to the AERIoe thermodynamic profile retrieval algorithm. *IEEE J. Sel. Top. Appl. Earth Observ.*, **12**, 1339-1354, doi:10.1109/JSTARS.2018.2874968.
- _____, and U. Löhnert, 2021: Ground-based temperature and humidity profiling: Combining active and passive remote sensors. *Atmos. Meas. Technol.*, **14**, 3033-3048, doi:10.5194/amt-14-3033-2021.
- Velden, C. S., W. L. Smith, and M. Mayfield, 1984: Applications of VAS and TOVS to tropical cyclones. *Bull. Amer. Meteor. Soc.*, **65**, 1059-1067, doi: 10.1175/1520-0477(1984)065<1059:AOVATT>2.0.CO;2.

- Verline, J., B. D. Zak, M. D. Shupe, M. D. Ivey, and K. Stamnes, 2016: The ARM North Slope of Alaska sites. *The First 20 Years, Meteor. Monogr.*, No. 57, Amer. Meteor. Soc., 8.1-6.13, doi:10.1175/AMSMONOGRAPHS-D-15-0023.1.
- Wagner, T. J., W. F. Feltz, and S. A. Ackerman, 2008: The temporal evolution of convective indices in storm-producing environments. *Wea. Forecasting*, **23**, 786-794, doi:10.1175/2008WAF2007046.1.
- Wark, D. Q., and Hilleary, D. T., 1969: Atmospheric temperature: A successful test of remote probing. *Science*, **165**, 1256-1258, doi:10.1126/science.165.3899.1256.
- Wulfmeyer, V., and Coauthors, 2018: A new research approach for observing and characterizing land-atmosphere feedback. *Bull. Amer. Meteor. Soc.*, **99**, 1639-1667, doi:10.1175/BAMS-D-17-0009.1.
- Wylie, D. P. and W. P. Menzel, 1999: Eight years of high cloud statistics using HIRS. *J. Climate*, **12**, 170-184, doi:10.1175/1520-0442(1999)012<0170:EYOHCS>2.0.CO;2.
- Yang, J., Z. Zhang, C. Wei, F. Lu, and Q. Guo, 2017: Introducing the new generation of Chinese geostationary weather satellites, Fengyun-4. *Bull. Amer. Meteor. Soc.*, **98**, 1637-1658, doi: 10.1175/BAMS-D-16-0065.1.
- Zavalyov, V., and Coauthors, 2013: Noise performance of the CrIS instrument. *J. Geophys. Res. Atmos.*, **118**, 13108-13120, doi:10.1002/2013JD020457.